Doctoral Thesis

Profiling of Antimicrobial Drugs Based on Yeast Single Cell Phenomics

（　酵母の単細胞フェノミクスに基づく抗菌薬のプロファイリング　）

アブラハム　アベラ　ゲブレ

Abraham Abera Gebre

The University of Tokyo

August 2016

Doctoral Thesis

Profiling of Antimicrobial Drugs Based on Yeast Single Cell Phenomics

酵母の単細胞フェノミクスに基づく抗菌薬のプロファイリング

Abraham Abera Gebre

Department of Integrated Biosciences

Graduate School of Frontier Sciences

The University of Tokyo

August 2016

Profiling of Antimicrobial Drugs Based on Yeast Single Cell Phenomics

Doctor of Philosophy (Ph.D.)

Abraham Abera Gebre

Department of Integrated Biosciences

The University of Tokyo

2016

In loving memory of my wife

Birtukan Endale Assefa

TABLE OF CONTENTS

TABLE OF CONTENTS ..... **I**

ACKNOWLEDGEMENTS ..... **III**

LIST OF FIGURES ..... **V**

LIST OF TABLES ..... **VI**

ABBREVIATIONS ..... **VIII**

SUMMARY **1**

GENERAL INTRODUCTION **3**

RESULTS AND DISCUSSION **11**

CHAPTER I: MORPHOLOGICAL PROFILING OF ANTIFUNGAL AGENTS **11**

1.1 INTRODUCTION 11

1.2 RESULTS 13

1.3 DISCUSSION 16

1.4 MATERIALS AND METHODS 17

1.5 FIGURES 20

1.6 TABLES 30

CHAPTER II: NEW PHENOTYPIC PROFILING METHOD FOR IDENTIFYING THE TARGETS OF BIOACTIVE COMPOUNDS **32**

2.1 INTRODUCTION 32

2.2 RESULTS 33

2.3 DISCUSSION 36

2.4 MATERIALS AND METHODS 40

2.5 FIGURES 43

2.6 TABLES 47

CHAPTER III: SENSITIVE AND HIGH-THROUGHPUT PROFILING OF THE RESPONSES OF ANTIMICROBIAL AGENTS FROM SINGLE CELLS **49**

3.1 INTRODUCTION 49

3.2 RESULTS 51

3.3 DISCUSSION 56
3.4 MATERIALS AND METHODS 57
3.5 FIGURES 60
3.6 TABLES 68

GENERAL DISCUSSION 75

PERSPECTIVES 79

APPENDICES 82
SUPPLEMENTAL RESULTS AND DISCUSSION 82
SUPPLEMENTAL EXPERIMENTAL PROCEDURE 82
SUPPLEMENTARY FIGURES 83
SUPPLEMENTARY TABLES 88

REFERENCES 143

ACKNOWLEDGEMENTS

First and foremost, I offer my sincerest gratitude to Prof. Yoshikazu Ohya for his relentless supervision throughout my doctoral study. Thank you for investing in me throughout the past three years - providing me with a challenging environment that has indisputably shaped me into a better scientist. Of note, your high caliber thinking and research excellence has truly inspired me.

My appreciation also goes to Dr. Suzuki Kuninori, an Asoc. Prof. of the laboratory of signal transduction for his encouragement and advises.

I thank my committee members Dr. Naoki Matsumoto, Dr. Shoji Oda, Dr. Shinji Nagata, and Dr. Hideki Yashiroda for their support of my project and their constructive comments.

I am indebted to the postdoctoral researchers at the laboratory of Prof. Ohya's - Dr. Shunsuki Ohnuki, Dr. Hiroki Okada, and Dr. Takahiro Negishi - for their insightful discussion, and encouragement during my stay at the University. I also thank Ms. Seiko Morinaga for her help in setting up high throughput image acquisition and subsequent follow-up experiments, and Mr. Suzuki Godai for his kind support when working with large-scale data in R.

Thanks go as well to Mr. Cholgwang Kim for his contribution in the early stages of this research project.

Many thanks to all the members of Prof. Ohya's laboratory for their encouragements, and creating friendly and stimulating working environment for learning and growing.

I acknowledge the Ministry of Education, Culture, Sports, Science and Technology in Japan (MEXT) for offering me a predoctoral (research student) scholarship, and a doctoral fellowship to successfully complete my PhD study at the University of Tokyo.

Lastly and perhaps most importantly, I would like to thank my family, parents, and brethren for their unwavering support. To my mom, dad, brothers and sisters – thanks for your constant encouragements during my study in Japan. To my beloved wife, Birtukan Endale Assefa – thanks for showing interested in my study and always understood me whenever I shall stay late at night in the laboratory to complete my experiments. I am lucky to have such a loving and supporting person in my life; to you I dedicate this work.

LIST OF FIGURES

Figure 0-1 Approaches in yeast chemical genomic studies..……..……..…….....9
Figure 0-2 Overall strategy in microscopy-based chemical genomics.…….……..10
Figure 1-1 Dose-dependency of morphologic changes induced by treatment with antifungal agents ……...…….……..……...20
Figure 1-2 Morphological changes induced by typical antifungal agents of various classes..…...…….…….…..……..…22
Figure 1-3 Morphological profiling of ergosterol, cell wall and nucleic acid biosynthesis inhibitors …….……..…….....24
Figure 1-4 Correlation among ergosterol, V-ATPase, and cell wall biosynthesis inhibitors ……..……...…25
Figure 1-5 Morphological analysis of ergosterol, and cell wall biosynthesis inhibitors for V-ATPase mutants profile …….……..…….…26
Figure 1-6 Treatment of budding yeast with ergosterol biosynthesis inhibitors disrupts V-ATPase function.…….……...……..28
Figure 1-7 Sensitivity of V-ATPase and cell wall drug-treated cells to Zymolyase…29
Figure 2-1 Schematic illustration of new phenotypic profiling method.....……43
Figure 2-2 Classification of antifungal drugs based on their morphological profile differences in 2D phenotypic space……..…….. 45
Figure 3-1 Morphological changes in *Δpdr1Δpdr3Δsnq2*…….……..60
Figure 3-2 Drug sensitivity of *Δpdr1Δpdr3Δsnq2*……...62
Figure 3-3 Schematic illustration of integrated method used in this study……..…...63
Figure 3-4 Prediction of 6 target-known compounds ……....…….65
Figure 3-5 Morphological similarity of yeast treated with standard compounds...….66
Figure 0-3 Conceptual frameworks for integrating antimicrobial drug development paradigms in this study……..……....…….…….....77
Figure S1. Growth inhibition and cellular effect of nystatin..…….…….83
Figure S2. Correlational network for ergosterol-, V-ATPase-, cell wall-acting agents. ……....……...……....…….…….....85
Figure S3. Commonly used antifungal drugs affecting ergosterol biosynthesis pathway of budding yeast, *Saccharomyces cerevisiae*…….…….....86

LIST OF TABLES

Table 1-1 Chemical compounds used in this study……..…30
Table 1-2 Enrichment of vacuolar acidification defects from WT cells treated with ergosterol and cell wall drugs……...…31
Table 2-1 Antimicrobial drugs used as test compounds in this study…….….47
Table 2-2 Comparison of the predictions of target-unknown drug classes by LDA analysis versus experimental research evidence…….….48
Table 3-1 Yeast mutants that shared significant similarity with benomyl treated hypersensitive host strain …….…….……..68
Table 3-2 Yeast mutants that shared significant similarity with tunicamycin treated hypersensitive host strain ……...…….69
Table 3-3 Yeast mutants that shared significant similarity with echinocandin B treated hypersensitive host strain…….…..……..70
Table 3-4 Yeast mutants that shared significant similarity with hydroxyurea treated hypersensitive host strain…….71
Table 3-5 Yeast mutants that shared significant similarity with methyl methanesulfonate treated hypersensitive host strain…..……...…….……..72
Table 3-6 Yeast mutants that shared significant similarity with bortezomib treated hypersensitive host strain …….…....…73
Table 3-7 Representative enriched GO processes associated with genes affected in sensitized yeast treated with antimicrobial compounds ……..……74
Table S1A List of parameters significantly affected by fluconazole ……..……88
Table S1B List of parameters significantly affected by terbinafine ……89
Table S1C List of parameters significantly affected by amorolfine ……...……91
Table S1D List of parameters significantly affected by flucytosine ……..…..…92
Table S1E List of parameters significantly affected by echinocandin B ……..…..94
Table S1F List of parameters significantly affected by micafungin ……..…106
Table S2A Parameters that describe major alteration induced by terbinafine treatment ……...……..…115
Table S2B Parameters that describe major alteration induced by flucytosine treatment …….……...…….……...…….…… 117
Table S2C Parameters that describe major alteration induced by micafungin treatment

…….……..…….……..……..… 119
Table S3 Vacuole morphology of antifungal agent-treated yeast cells **……..…122**
Table S4 List of parameters involved in three PCs that optimally classified antifungal drugs at FRD= 0.1**…….…..…...123**
Table S5 Results of GO term analysis showing the genes related to the effect of the antifungal agents **…….……..126**
Table S6 Independent morphological features describing triple mutants**……..…135**
Table S7 Description of *S. cerevisiae* hypersensitive deletion strains used in this study **……...….138**
Table S8 Representative gene set enrichments for the GO term related to the effect of the antimicrobial agents on hypersensitive strain..**……..…..…..……..139**

ABBREVIATIONS

AMF	amorolfine
α	alpha
β	beta
BMC	bleomycin
BML	benomyl
BTZ	bortezomib
C_n	carbon at n^{th} position
CAF	caffeine
CalMorph	calculated morphology
CMA	concanamycin A
ConA	concanavalin A
Δ	deletion (of a gene)
°C	degree Celsius
2D	two-dimensional
DAPI	4',6'-diamino-2-phenylindole
DC	decarboxylated
DIC	differential interference contrast
DMSO	dimethyl sulfoxide
DNA	deoxyribonucleic acid
DW	distilled water
ECB	echinocandin B
FACS	florescence activated cell sorting
FCS	flucytosine
FCZ	fluconazole
FDR	false discovery rate
FITC	fluorescein isothiocyanate
GLM	generalized linear model

GO	gene ontology
h	hour
HCS	high content screening
HIP	haploinsufficient profiling
HMG-CoA	3-hydroxy-3-methylglutaryl-coenzyme A
HOP	homozygous profiling
HTP	high throughput
HU (or HXU)	hydroxyurea
HYG	hygromycin B
kanMX	kanamycin resistant cassette
kb	kilobase pair(s)
LD	linear discriminant
LDA	linear discriminant analysis
LVS	Lovastatin
*MAT***a**	yeast mating type a
*MAT*α	yeast mating type alpha
MCF	micafungin
MCZ	miconazole
Min	minute(s)
μm	micromolar
μg/ml	microgram per milliliter
MMS	methyl methanesulfonate
MoA	mode of action
mRNA	messenger RNA
natMX	nourseothricin resistant cassette
nM	nanomolar
ng/ml	nano gram per milliliter
NMZ	nikkomycin Z
OD	optical density

ORF	open reading frame
p	probability value
PCA	principal component analysis
PC	principal component
PDR	pleiotropic drug response
PI	propidium iodide
%	percent
QMT	quadruple mutants
R	correlation coefficient
RNA	ribonucleic acid
S. cerevisiae	*Saccharomyces cerevisiae*
SCMD	*Saccharomyces cerevisiae* Genome Database
SGA	synthetic genetic array
SGD	saccharomyces genome database
SSU-rRNA	small subunit ribosomal RNA
TBF	terbinafine
TCM	tunicamycin
TM	triple mutant
V-ATPase	vacuolar proton-transporting V-type ATPase
WT	wild type
YPD	yeast extract peptone 2% glucose
YPGal	yeast extract peptone 2% galactose
Z-value	a test statistic for Z-tests

SUMMARY

Antimicrobial drug discovery is the most challenging field. For several decades, most of the drug discovery efforts have concentrated on target-based screens which generates protein disease model first and finds a candidate lead molecule. In contrast, less-biased phenotypic screening approaches have shown promises in potentially improving success rates of drug development. For comprehensive drug screening, various chemical genomic approaches have been developed to systematically search for targeted chemical libraries of compounds that potently and selectively modulate the functions of target proteins. Among others, single-cell phenomics technology, a microscopy-based chemical genomic method, has emerged as a critical set of tools for enhancing the power of analyses (Ohya *et al.*, 2015). It involves the acquisition of high-dimensional phenotypic profiles of a single cell in response to drug stimuli on a genome-wide scale from which the drug target is estimated by comparing morphological profiles of chemical perturbation with that of gene disruption. Using image-processing system CalMorph, Ohnuki *et al.* (2010) demonstrated that a drug target could be predicted from dose-dependent morphological changes induced by the drug. Later, the high-dimensional morphological data generated in a similar way has been exploited in identifying new targets of drugs as well as exploring their mode of action (Iwaki *et al.*, 2013; Okada *et al.*, 2014; Piotrowski *et al.*, 2015). Though it is considered that our current approach is powerful, much more simpler, efficient and complementary methods are required as significant tools for drug discovery and development. Therefore, I envisaged gaining further insights into the currently available antimicrobial drugs, and proposing new method(s) for discovering molecular targets and mode of action of novel drugs. In this study, I discussed the alternative methods for elucidating the potential mechanisms of action and identifying cellular targets of a candidate antifungal compound. In the first chapter, I focused on profiling currently available antifungal drugs using yeast morphology as a chemogenomic signature. Our similarity search system revealed not only the expected similarity but also unexpected functional connection among different cellular process. In the second chapter, as an alternative to current method, I proposed the development of new phenotypic profiling method, which sorts a newly discovered compound into a class with a similar mode of action without any mutant information. In the third chapter, aiming at reducing the amount of candidate compound required for

morphometric analysis using WT yeasts, I developed another method which combines drug-hypersensitive yeast collection and high-throughput microcopy. Herein, dose-dependent morphological phenotype of the drug-hypersensitive host strain was compared with the new panel of morphological data composed of ~2,000 representative quadruple mutant strains. The applicability of an integrated approach was demonstrated in profiling the targets of landmark anticancer and antifungal compounds. I hope that this strategy will facilitate the development of drugs for rare and/or neglected diseases as well as potentially useful novel compounds from scarce natural products to treat various diseases.

GENERAL INTRODUCTION

Overview of antimicrobial drug discovery and development

Infectious diseases account for a considerable amount of deaths worldwide. They generally result from the interaction between few pathogens among the many varieties of microorganisms, and the defense mechanisms of the hosts they infect (Engering *et al.*, 2013). A relatively few list of pathogenic bacteria contribute to globally important diseases in human including tuberculosis caused by *Mycobacterium*, pneumonia induced by *Streptococcus* and *Pseudomonas*, foodborne illnesses caused *Shigella*, *Campylobacter*, and *Salmonella,* and some others cause infections such as tetanus, typhoid fever, diphtheria, syphilis, and leprosy (Morens *et al.*, 2004). In addition, infections are being caused by few opportunistic fungi species, mainly *Candida spp.*, *Cryptococcus neoformans*, *Aspergillus spp.*, *Histoplasma capsulatum*, *Coccodiodides imitis* and *Fusarium species* (Ablordeppey *et al.*, 1999; O'Brien *et al.*, 2005). These opportunistic fungal infections are life-threatening diseases that cause increasing rates of mortality and morbidity, particularly in individuals' with impaired immune system.

For the last several years, antibiotics and similar drugs, hereafter called antimicrobial agents, have been used to treat individuals affected by infectious diseases (Spellberg *et al.*, 2004). Antimicrobial agent refers to natural, or synthetic substance that kills or inhibits the growth of microbes that cause little or no damage to the host. They are often grouped according to the microorganisms they act primarily against - antibiotics used for drugs against bacteria, and antifungals for those against fungi. Antimicrobial drug discovery is the most challenging field (Livermore, 2011; Silver, 2011). The discovery and development of antifungal agents was lagging far behind the antibiotics despite the knowledge of their existence well before that of bacteria. The main reason is that most agents toxic to fungi are also noxious to the human hosts as they are eukaryotic species, which are biochemically similar to the hosts as opposed to the prokaryotes. This difficulty ultimately complicates evaluation of properties of a potential antifungal agent *in vitro* or *in vivo*. To elude the damage to the human cells, the use of such antimycotic agents should exploit subtle differences between mammalian and fungal cells; *e.g.* sterol components - cholesterol and ergosterol.

Cholesterol is the major sterol in the plasma membranes of higher eukaryotes, while ergosterol is present in lower eukaryotes including yeast and other fungi (Bloch, 1983). The notable difference between the two sterols is in their chemical structures - ergosterol has two additional double bonds (at positions C_7 and C_{22}) and a methyl group at C_{24} of the side chain. In spite of limitations, advancements have been made in understanding the existing antifungal agents as well as developing even the new ones. Since the golden era of antibiotics (~1940-1970), different new antimycotics have been discovered and limited of them have reached the clinic (Butts & Krysan, 2012). The polyene antifungal agents, namely nystatin, amphotericin B, and pimaricin, were discovered in 1950's. In the early 1960's, Griseofulvin, the first orally effective antibiotic was used for dermatophytosis management. Later in 1969, the discovery of broad-spectrum agents such as azole antifungal agents that functioned by disrupting the fungal cell membrane was the success story. Imidazole, triazole and polyenes in current use had been introduced into the clinics by 1980. It took about 3 decades for the newest class of antifungal drugs, the echinocandins, to translate basic scientific findings into therapies (Mukherjee *et al.*, 2011). Despite these contemporary therapeutic interventions, preventing most invasive fungal infections are far from ideal (Roemer & Krysan, 2014).

To treat infectious diseases, natural products and their derivatives have been an ultimate source of new therapeutic agents (Newman *et al.*, 2003). Indeed, the vast majority of antifungals in current clinical use, including polyenes and echinocandins, are natural product derivatives. Researchers aim to find new antimicrobial agents either by discovering bioactive compounds from natural sources such as plants, microorganisms, or by systematic screening of compound libraries (Shen, 2015). As an approach to expediting drug development in general, the concept of drug repurposing has also emerged to treat new diseases. However, the campaigns continue to rediscover previously known molecules from new natural product collections remain a challenge facing natural product-based screening (Roemer *et al.*, 2011).

In the past few decades, most of the drug discovery efforts have concentrated on target-based screens, in which disease model and pathway analysis generate candidate proteins, followed by a biochemical studies to find candidate small molecules (Schenone *et al.*, 2013). Phenotypic drug discovery, a less-biased method however,

has enabled the cell to reveal a target required to achieve a desired phenotype (Eggert, 2013; Schenone *et al.*, 2013). Using drugs discovered between 1999 and 2008, Swinney & Anthony (2011) demonstrated that 28 (56%) of 50 first-in-class new molecular entities approved clinically were discovered by phenotype approach, while 17 (34%) were target-based. This striking analysis underlined the power of phenotype-based discoveries. The resurgence of phenotypic screening is partly due to the adaptation of high content imaging to drug discovery (Lang *et al.*, 2006) along with computer-driven detection and analysis with immunofluorescent techniques (Wagner & Schreiber, 2016).

Yeast chemical genomic approaches in drug discovery

Model organisms are the main workhorse of biological research, offering manipulable and cost-effective experimental systems that constantly yield fundamental insights into human biology and health. Amongst others, budding yeast *Saccharomyces cerevisiae* has been an excellent model to study various aspects of mammalian biology by acting as a living eukaryotic vehicle for carrying reporter constructs for screening (Ross-Macdonald, 2003) or as a representative of its pathogenic counterparts (Mccusker, 2006). This long utility certainly extends to pharmaceutical drug discovery process, including its use to isolate novel lead molecules, to reveal the mechanism of action of compounds, to discover and characterize components of signalling pathways and to dissect protein function. Moreover, Kachroo *et al.* (2015) demonstrated that almost half (47%) of yeast genes could systematically be functionally replaced with their human cousins, implying the relevance of addressing human life challenges through the study in yeast.

In order to comprehend how life works, genetics aims at understanding the relation between genotype and phenotype. Though, it is formidable to study their gene functions as complete deletion of most yeast genes (~80%) has no apparent phenotypic effect in rich medium (Hillenmeyer *et al.*, 2008). In light of this, small molecules are shown potent probes for dissecting cellular physiology at all levels of biological complexity (Schreiber, 2005). It is, thus, of paramount importance to study the biological systems using chemical perturbation, instead of genetic intervention alone. For studying chemical-biological interactions, diverse fields have emerged to

understand the relations between small molecules and genes on a systems level. The current strategies in drug discovery and development are chemical biology, chemical genetics, and chemical genomics. Chemical biology may be defined as the application of chemistry to the study of molecular events in biological systems. As such if a new phenotype is discovered by the action of a certain compound, the identification of the responsible target follows. Chemical genetics is the dedicated study of proteins and signal transduction pathways by the screening of chemical libraries of small molecules. Chemical genomic, or chemogenomic, study is an approach that combines the latest tools of genomics and chemistry, and applies them to target and drug discovery. It enables one to understand genomic responses to small molecule perturbants.

Numerous chemical genomic approaches have been developed to provide a platform that contends with the complexity inherent in the postgenomic view of cellular biology. Current yeast-based chemical genomic studies encompass high-throughput genomic approaches (Fig. 0-1) such as fitness profiling (Giaever *et al.*, 1999, 2002), and transcript profiling (Hughes *et al.*, 2000), as well as high content image profiling (Ohya *et al.*, 2005). In light of this, remarkable advances in *S. cerevisiae* chemical genomics have been achieved via a technological development that enabled invention of genome-wide clone sets. One of the most important technical feats was the systematic modulation of gene dosage on a genome scale (Rine *et al.*, 1983). The first demonstration in yeast was that drug targets could be identified by their ability to confer resistance when overexpressed. In addition, the advancements of chemical genomic assays on the yeast whole-genome heterozygous and homozygous deletion collections have enabled the quantification of the growth fitness of each deletion strain in the presence of chemical stress conditions, hence uncovering a phenotype of all genes (Giaever *et al.*, 2002; Hillenmeyer *et al.*, 2008). Additionally, microarray-based transcriptional profiling proved a valuable tool to thoroughly understand the cell's immediate and dynamic response to a perturbant on a genome-wide level (Bammert & Fostel, 2000; Hughes *et al.*, 2000; Agarwal *et al.*, 2008) and global biological networks (Creighton & Hanash, 2003). Moreover, cellular morphology is closely linked to cellular processes and functions in virtually all eukaryotic organisms. Fluorescence imaging proved a valuable tool for high-content assays that appraises *in vivo* effects of genetic or chemical perturbation using multiple cellular

response parameters (Ohya *et al.*, 2005; Vizeacoumar *et al.*, 2009). As such microscopy-based screens (Fig. 0-2) facilitate phenotype measurements in individual cells and heterogeneous response analyses, which provide deeper insights into biological processes and function (Ohya *et al.*, 2005, 2015; Liberali *et al.*, 2015). This approach was successfully applied to predict drug targets in a cell by matching the morphological profiles of a drug-treated cell with that of the mutant collection.

Application of yeast single cell phenomics in drug targets prediction

In high content image profiling, quantitative morphological analysis was performed using CalMorph, a program that outputs a large amount of data on cell cycle phase, cell forms, and other parameters (Ohtani *et al.*, 2004). High-dimensional morphological information obtained after treating of the cells with a drug of serial concentrations made it possible to search for a set of mutants with a similar morphology (Ohnuki *et al.*, 2010). A multidimensional quantitative data generated this way was used to predict drug target, functionally related genes as well as exploring mode of action (Iwaki *et al.*, 2013; Okada *et al.*, 2014; Piotrowski *et al.*, 2015). First, Iwaki and his colleagues showed that prediction of intracellular target of chemicals based on morphological profiling was effective for vanillin, an antimicrobial compound produced by degradation of lignocellulose (Iwaki *et al.*, 2013). Therein, comparison of the morphological profiles of vanillin-treated cells and non-essential gene deletion mutants revealed that components of large subunits of ribosome shown to be its target. In addition, Okada and his colleagues performed quantitative morphological analyses after treatment with drugs that inhibit different processes during cell wall synthesis, to uncover the distinct role of cell wall biogenesis (Okada *et al.*, 2014). The profiles of the tunicamycin treatment showed significantly similar morphology to those of strains defective in α-mannosylation, consistent with its mode of action which blocks *N*-glycosylation (Ballou, 1990; Jigami, 2008). Likewise, morphological profiling was conducted to define the mode of action of echinocandin B. They found that echinocandin B induced morphological effects similar to those observed in some *fks1* mutants, with reduced glucan synthesis activity, suggesting that the agent affects 1,3-β-glucan synthesis, and additional functional domain. More recently, similar technique was applied for identification of the intracellular target of poacic acid, newly extracted compound from plant lignocellulose (Piotrowski *et al.*, 2015). Analysis of morphological profiles of

compound-treated cells established that poacic acid caused similar phenotype to many cell-wall defective mutants. They further verified that poacic acid had antifungal activity on many phytopathogenic fungi by binding to 1,3-β-glucan thereby inhibiting glucan synthase activity of fungal cells.

In this dissertation, I summarized the findings of my diverse research themes into three principal chapters. The first chapter deals with morphological profiling of antifungal agents with current morphological profiling approach while the second chapter introduces the proposal of a new phenotypic profiling method for identifying the targets of bioactive compounds as an alternative to our current approach. The last chapter describes the development of sensitive and high-throughput profiling method for studying the responses of antimicrobial agents from single cells, and demonstrates its applicability using diverse landmark compounds.

FIGURES

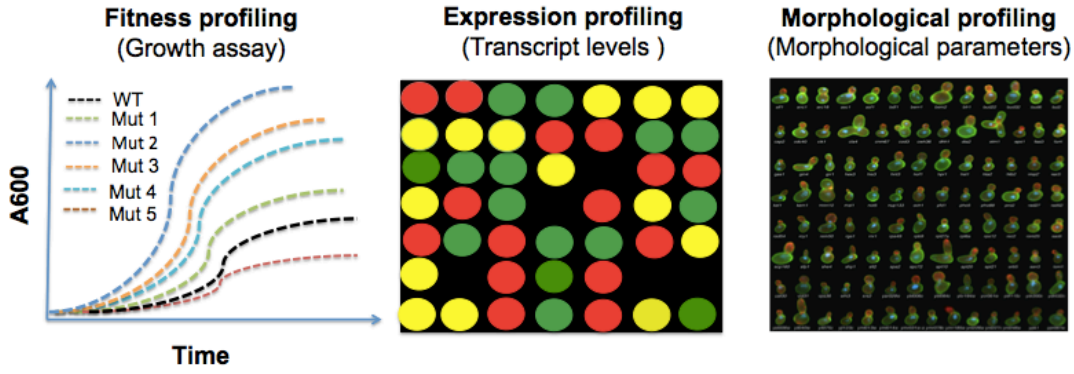

Figure 0-1. Approaches in yeast chemical genomic studies.

(A) Fitness profiling. Profiling of an organism's growth could be used to identify the genes involved in some of adaptive responses, *e.g.* all genes required for a role in response to challenge with the antimicrobial compound (Giaever *et al.*, 1999). (B) Expression profiling. Because the relative abundance of transcripts is tailored to specific cellular needs, expression profiling studies were used to monitor the genes that respond to conditions or treatments of interest using DNA microarray hybridization assay (Hughes *et al.*, 2000). (C) Morphological profiling. Analysis of fluorescent microscopic images of triple-stained cells makes it possible to treat morphological variations (parameters) as quantitative traits to study attributing functions to genes (Ohya *et al.*, 2005).

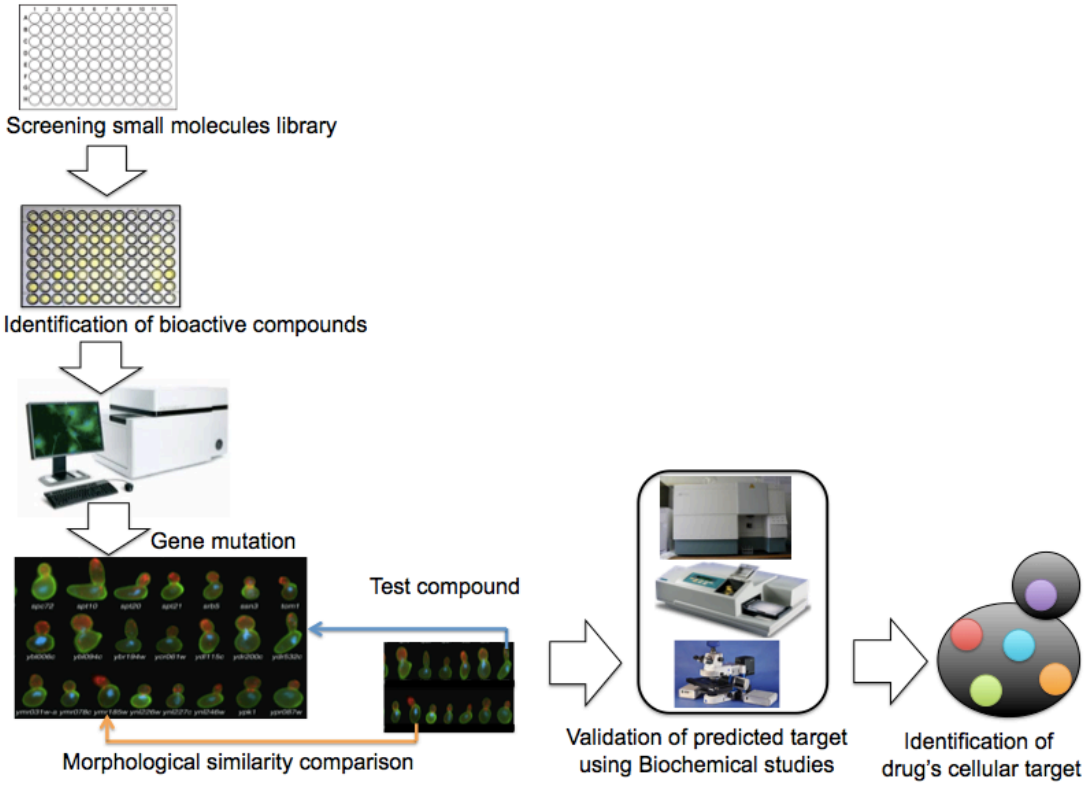

Figure 0-2. Overall strategy in microscopy-based chemical genomics.

Generally, chemogenomics-based drug discovery involves screening of large collections of chemical products for the parallel identification of biological targets and biologically active compounds. In image-based approach, this followed by analysis of the phenotypic profiles after high-content, high-dimensional morphological data acquisition. The underlying principle of target prediction laid on the assumption that a compound, which induces a specific phenotypic change, should share similar perturbation profiles with that of gene mutation or authentic drug. Therefore, comparison of similarity of morphology induced by a compound of interest induced with that of gene deletions (reference set) should provide its likely intracellular targets and pathways involved in. Ultimately, the molecular targets predicted by the morphological profiling of yeast treated with biologically active compounds are then validated for appropriateness using different techniques including biochemical studies.

RESULTS AND DISCUSSION

Chapter I: Morphological Profiling of Antifungal Agents

1.1 INTRODUCTION

Identification of the molecular targets is indispensable during the development of new antifungal drugs (Hughes *et al.*, 2000; Carrillo-Muñoz *et al.*, 2006; Agarwal *et al.*, 2008). Antifungal drugs with known clear targets can be easily applied for antifungal therapies. Antifungal drugs with distinct molecular targets are attractive because of the effectiveness of their combinatorial usage.

Several potential criteria must be fulfilled by targets of antifungal drugs (Agarwal *et al.*, 2008). A potential target must be essential for fungal cell survival either in the process of static growth, homeostatic stability or infection of the host. It is also important for the target to be a fungal-specific protein; otherwise, even if it is conserved, the affinity of the counterpart to the drugs must be low. Fungal-specific metabolic pathways are attractive targets because each metabolic component is a potential target. Finally, because the plasma membrane can act as a barrier to chemicals, cell surface proteins are preferable as targets.

Due to these restrictions, the intracellular targets of currently available antifungal drugs are limited to the processes related to the cell wall, the cell membrane and ribonucleotide metabolism. Echinocandins such as echinocandin B, caspofungin and micafungin target the biosynthesis of 1,3-β-glucan, a key fungal cell wall component (Perlin, 2007). A recent study of drug-resistant mutant echinocandins suggested that the drugs impact a putative catalytic subunit of 1,3-β-glucan synthase, Fks1p (Johnson *et al.*, 2011; Johnson & Edlind, 2012). Azole compounds (Bodey, 1992) such as fluconazole and miconazole, allylamine compounds (Petranyi *et al.*, 1984) such as terbinafine and naftifine, and morpholine compounds (Polak-Wyss *et al.*, 1985) such as fenpropimorph and amorolfine impact ergosterol biosynthesis. Azoles, allylamines and morpholines inhibit lanosterol 14 α-demethylase, squalene epoxidase and Δ^{14} reductase/Δ^{7}-Δ^{8} isomerase, respectively (Carrillo-Muñoz *et al.*, 2006).

Ergosterol, a component of the fungal membrane itself, binds to polyene antifungals such as nystatin and amphotericin B (Zygmunt & Tavormina, 1966). Finally, flucytosine, or 5-fluorocytosine, a fluorinated pyrimidine analog, is a synthetic antifungal drug that inhibits ribonucleotide metabolism (Finland & Schönebeck, 1972). Although antifungal drugs with the same structural backbone have similar modes of action (MoA), the reverse is not always the case. New drugs with novel structures could be established without relying on structure-based screening.

Phenotype-based screening has been also recognized as a reliable approach to identifying new antifungal drugs. Such techniques have recently become more powerful after the development of modified phenotypic screens, such as high-throughput, high-content and omics-based screens (Feng *et al.*, 2009; Houle *et al.*, 2010; Roti & Stegmaier, 2012; Futamura *et al.*, 2013a). Various genomic and genetic tools for the advancement of genome-wide studies in *Saccharomyces cerevisiae* have been developed (Luesch *et al.*, 2005; Bharucha & Kumar, 2007), and a large-scale data set has been deposited in public databases, greatly facilitating the comparison and interpretation of results. Expression profiling and fitness profiling have been widely used for these purposes. It was reported that the pattern of changes in global gene expression can be used as a fingerprint to identify specific pathways perturbed by the chemical compounds (Hughes *et al.*, 2000). Fitness profiling with a decreased or increased gene dosage was shown to facilitate classification of chemical compounds with similar MoAs (Hillenmeyer *et al.*, 2010; Lee *et al.*, 2013).

Another phenotype-based approach that involves the assessment of a high-dimensional cellular response caused by the drugs is image-based profiling (Perlman *et al.*, 2004). Ohnuki and his colleagues developed the image-based method to infer drug targets based on the yeast morphological changes after treatment (Ohnuki *et al.*, 2010). The morphological profiles induced by the drugs were statistically compared with those induced by deletion of each of 4,718 non-essential genes. Based on the ranking of similarity in each mutant, this method was capable of inferring intracellular targets among the 4,718 non-essential genes (Ohnuki *et al.*, 2010; Iwaki *et al.*, 2013; Piotrowski *et al.*, 2015). However, no systematic analysis and comparison of antifungal drugs based on morphological profiling has been performed to date.

To gain further insights into antifungal drug profiles, I profiled currently available antifungal drugs using yeast morphology as chemogenomic signature. I analyzed echinocandins (echinocandin B and micafungin), an azole (fluconazole), an allylamine (terbinafine), a morpholine (amorolfine) and a fluorinated pyrimidine analog (5-fluorocytosine). Comparison with deletion mutants of each of 4,718 non-essential genes confirmed the MoA of the drugs and revealed unexpected connections among the various cellular processes. This suggested the comparison between chemical-induced phenotypes and genetic perturbation is a powerful method to understand the MoA of antifungal agents.

1.2 RESULTS

Morphological changes induced by antifungal agents

I examined the morphological changes after treating haploid yeast cells with antifungal agents that disrupt three well-known targets—the ergosterol, nucleic acid and cell wall biosynthesis pathways (Table 1-1). To minimize high-dose side effects, I used the concentration of each drug that delayed the wild-type cell growth by 10% for morphological analysis (see Materials and methods). I found that cells treated with FCZ, TBF, AMF, FCS, ECB, and MCF displayed aberrant morphological phenotypes (Fig. 1-1A). To explore the dose-dependency of these effects, I quantified 501 morphometric parameters using CalMorph (Ohtani *et al.*, 2004) after treatment with various concentrations of the drugs (Table 1-1) and analyzed them using the Jonkheere-Terpstra test, a test for an ordered alternative hypothesis within the data sets (Jonckheere, 1954). Of the 501 morphological parameters examined, I successfully identified 17, 52, 9, 49, 343, and 251 dose-dependent parameters of FCZ, TBF, AMF, FCS, ECB and MCF, respectively (Table S1, A-F). I did not use nystatin, an agent binding to ergosterol, because its pharmacological effect did not allow us to observe the morphological changes (Fig. S1; see Supplemental procedure, and results & discussion).

I next analyzed these dose-dependent parameters as described previously (Ohnuki *et al.*, 2012). Figure 1-1B shows that the PC1 scores increased in a dose-dependent manner for each of the antifungal agents, suggesting that similar morphological changes became progressively more apparent in the data sets. Next, I performed PCA to identify independent features in the dose-dependent parameters (see Materials and

methods; Table S2, A-C). Accordingly, I illustrated phenotypic responses to the representative agents and summarized the morphological changes of yeast cells at the indicated cell cycle stages using representative features (Fig. 1-2A). As shown in Figure 1-2B, a moderate relationship was observed between MCF and TBF, but a weak or negligible relationship was recorded between FCS and the other two agents (TBF & MCF). Consistent with their difference in MoA, the agents of the three classes induced distinct alterations in cellular, actin, and nuclear morphology.

Morphological profiling of the antifungal agents—expected similarities

To unravel the MoA of the antifungal agents in more detail, a comparison of the morphological profiles of the cells treated with the agents and those of non-essential deletion mutants with defects in their MoA-related genes was conducted (Ohnuki *et al.*, 2010). Among the 4,718 haploid non-essential gene deletion mutants, I identified morphologically similar gene deletion mutants ($p < 0.05$, after Bonferroni correction) after treatment with each drug (Fig. 1-3).

I then analyzed the genes enriched in the mutants similar to those in cells treated with FCS, a nucleic acid biosynthesis inhibitor, using the GO term finder (Boyle *et al.*, 2004). I found that the genes related to maturation of small subunit ribosomal RNA (SSU-rRNA; GO ID: 0000462) were significantly enriched (Fig. 1-3; Table S5). FCS is known to be bioconverted into cytostatic fluorouracil, which, in turn, is further converted to metabolites that inhibit fungal RNA and DNA synthesis (Waldorf & Polak, 1983; Parker & Cheng, 1990; Vermes, 2000; Fang *et al.*, 2004). Therefore, FCS was likely incorporated into newly synthesized RNA and potently blocked rRNA processing; thus, FCS-treated cells were similar to SSU-rRNA mutants. Treatment with two ergosterol biosynthesis inhibitors (FCZ and TBF) resulted in significant morphological similarities with an *erg28* mutant (Fig. 1-3; Fig. 1-4; Table S5), a mutant endoplasmic reticulum membrane protein, required for ergosterol biosynthesis (Mo *et al.*, 2004). The correlation coefficients for *erg28* were 0.57 and 0.70 for FCZ and TBF, respectively. This finding is consistent with Hughes *et al.* (2000), who demonstrated by microarray analyses that the *ERG28* transcript is induced in *erg11*, *erg2*, *erg3* and wild-type cells treated with azole drugs. AMF-treated cells were significantly associated with an *erg2* mutant (Fig. S3), a mutant of C-8 sterol isomerase (Rahier *et al.*, 2008). This result is in line with the findings of Jia *et al.*,

(2002) who reported that, like other morpholines, AMF targets primarily Erg2, although it has been shown to also inhibit Erg24 at higher concentrations. The morphology of cells treated with two cell wall biosynthesis inhibitors (ECB and MCF) shared significant similarity with that of two mutants (*hoc1* and *mnn10*), which have defects in "cell wall biogenesis" (Fig. 1-3, Fig. 1-4). Analysis of ECB-MCF correlation revealed strong similarity between cell wall drugs (Fig. S2). This is reasonable because even if the two compounds are distinct but of the same target. This indicates the validity of morphometric approach in finding likely targets of the drugs including previously unreported ones.

Morphological profiling of the antifungal agents—unexpected similarities

Strikingly, I found some unexpected morphological similarities between the cells treated with ergosterol affecting agents and V-ATPase-affecting agent, CMA (Fig. 1-4, Fig. S2). The GO term analysis of mutants similar to cells treated with FCZ, TBF and AMF showed no enrichment in the genes responsible for the ergosterol pathway, but the genes responsible for V-ATPases (Table S5). I also observed high morphological similarity between the yeast cells treated with ergosterol-affecting and V-ATPase-inhibiting agents (Fig. 1-5). The similarity between the cells treated with ergosterol-affecting agents and vacuolar ATPase-deficient cells suggested a role of ergosterol in V-ATPase function, although there is little direct evidence (Zhang *et al.*, 2010). I then assessed the effect of ergosterol inhibitors on the vacuole. Cells treated with ergosterol inhibitors showed a decrease in the ergosterol content in wild-type cells (Kelly *et al.*, 1995). In addition, I observed the reduction of vacuolar quinacrine fluorescence in wild-type yeast cells (Fig. 1-6, Table S3), implying that the antifungal drugs had impaired vacuolar acidification. Taken together, these data suggest that ergosterol depletion is a likely mechanism of antifungal activity for disrupting V-ATPase function.

Likewise, GO term analysis using mutants that were similar to ECB- and MCF-treated cells showed enrichment in several genes related to vacuolar function (Fig. 1-5; Table 1-2; Table S5). This unexpected similarity might be because of the cell wall perturbation induced by defective vacuoles. To this end, robust morphological similarity found between inhibitors of cell wall synthesis (ECB, and MCF) and the V-ATPase inhibitor (CMA) may support this idea (Fig. 1-4; Fig. S2). I next tested

whether this association could be explained by cell wall defects across those antifungal drugs of different classes (ECB, MCF and CMA). To assess the impact of drug treatments on the cell wall structure, I measured the susceptibility of yeast cells to zymolyase, an enzyme that effectively lyse cell wall of viable yeast cells (Lussier *et al.*, 1997; Ovalle *et al.*, 1998). I found that preincubation of yeast cells with CMA and cell wall-affecting drugs similarly resulted in an increased sensitivity to zymolyase compared with the mock-treated cells (Fig. 1-7). Therefore, I concluded that unexpected similar phenotypes between CMA-treated and ECB- or MCF-treated cells are due to the functional connection between these two cellular processes.

1.3 DISCUSSION

A wealth of biologically meaningful information can better be obtained from a well-designed research in conjunction with suitable statistical analysis. To mine genetically and biologically important information, application of morphometric analysis high-dimensional yeast morphological data was shown a powerful approach. This is fundamentally because a single experiment usually provides a high-dimensional morphological data set in which each cellular image contains various morphological features. To this end, quantification of cell shape, actin, nuclear DNA, and microtubular morphology was finalized for a collection of nonessential deletion mutants (Ohya *et al.*, 2005; Vizeacoumar *et al.*, 2009). Such morphological data has enabled us to search for a set of mutants that share significant similarity with morphology of cells treated with chemical compound (Ohya *et al.*, 2005). Notably, this method was shown to be a powerful tool to identify the target and describe the mode of action of a candidate compound (Ohnuki *et al.*, 2010, 2015).

Morphological similarities among the antifungal agent-treated cells

Our quantitative morphological analyses showed distinct but somewhat similar morphological phenotypes among the cells treated with ergosterol-, vacuole-, and cell wall-acting agents. It is important to know the mechanism of their similarity because it is directly related to the understanding of the fungal physiological system. Experimental evidence, in fact, has supported their functional relationships; ergosterol-deficient cells showed no acidification of vacuoles, and vacuolar-deficient cells showed cell wall defects. These findings are also particularly of interest from

therapeutic aspects because of the frequent combinational use of antifungal drugs in therapy. It is known that a synergetic antifungal effect of 11% was recorded for the antifungal combination of MCF with FCZ against clinical isolates *Candida spp.* without any antagonistic influence (Nishi *et al.*, 2009). AMF also showed a synergetic combination with terbinafine and azole drugs (Polak-Wyss, 1995). These facts suggest that the high-content profiling of antifungal drugs is useful for the understanding of yeast cell biology and pharmacology of antifungal agents.

1.4 MATERIALS AND METHODS

Antifungal agents

The compounds, their acronyms and suppliers are as follows: fluconazole (FCZ; Tokyo Chemical Industry, Tokyo, Japan), terbinafine (TBF; Tokyo Chemical Industry), amorolfine (AMF; Tokyo Chemical Industry), flucytosine (FCS; Sigma-Aldrich, St Louis, MO, USA), echinocandin B (ECB; a kind gift from O. Kondo, Chugai Pharmaceutical, Tokyo Japan), micafungin (MCF; Astellas Pharma, Tokyo, Japan), lovastatin (LVS; Wako Pure Chemical Industries, Osaka, Japan), concanamycin A (CMA; Sigma-Aldrich), Stock concentrations and solution preparation methods are summarized in Table 1-1.

Culture conditions for morphological analysis

Yeast culture for morphological analysis was performed as described previously (Ohnuki *et al.*, 2010). The *S. cerevisiae* haploid strain BY4741 (*MAT*a; *his3*Δ1 *leu2*Δ0 *met15*Δ0 *ura3*Δ0) was used as the wild-type (WT) strain. Cells were grown at 25 °C in yeast rich medium (YPD) containing 1% Bacto yeast extract (BD Biosciences, San Diego, CA, USA), 2% Bactopeptone (BD Biosciences) and 2% glucose (Wako Pure Chemical Industries). Growth inhibitory tests were performed, with or without a compound, at least twice using the biophotorecorder TVS062CA (Advantec, Tokyo, Japan). The doubling time was calculated to determine the inhibitory concentration that delayed the growth by approximately 10% of that of the control. Cell samples were grown (n = 5) in the presence of various concentrations of the study drugs, up to the 10% inhibitory concentration (Table 1-1).

Image acquisition and processing

Morphological data were acquired as described previously (Ohya *et al.*, 2005). I quantified the morphological attributes in budding yeast to obtain 501 parameter values from at least 200 individual cells in each experiment using the automated image-processing software CalMorph (*ver.* 1.2) for haploid cells. The CalMorph software can be downloaded from SCMD: *S. cerevisiae* Genome Database (Saito *et al.*, 2004). For illustrative purposes, images were processed using Adobe Photoshop CS2 (Adobe Systems, San Jose, CA).

Statistical Analysis

Most of the statistical analyses were performed using R *ver.* 3.0.0 (http://www.r-project.org/). A custom-made Java-based program was used to assess the morphological similarity between the cells treated with each agent and 4,718 non-essential gene deletion mutants, as reported previously (Ohnuki *et al.*, 2010, 2015).

Extraction of morphological features

To elucidate complex phenotypic changes in the cell, principal component analysis (PCA) was performed using the prcomp() function in R as described previously (Ohnuki *et al.*, 2012; Iwaki *et al.*, 2013; Okada *et al.*, 2014; Piotrowski *et al.*, 2015). The dose-dependent parameters were detected by the Jonckheere-Terpstra test. Significant parameters, obtained from five replicated experiments of each drug data set (FDR = 0.05, t-test; Table S1), were transformed into rank-sum values to standardize the distribution. To identify morphological features, I executed a PCA on selected parameters using 122 replicated WT morphological data as a null distribution. Among several independent PCs extracted, at least one parameter in each PC was selected as a representative parameter (highlighted in yellow, Table S2) by considering significant absolute loading values (> 0.5). Based on the representative parameters, drug-induced morphological changes are depicted.

Gene ontology (GO) terms analysis

Information on GO annotations was gathered using the "GO Term Finder," ver. 0.83 (http://www.yeastgenome.org/cgi-bin/GO/goTermFinder.pl) in the *Saccharomyces* Genome Database (Boyle *et al.*, 2004). Genes of morphologically similar mutants were used as query genes, and 4,708 of 4,718 non-essential genes associated with at least one GO term were considered as the background gene set.

Quinacrine staining

Quinacrine staining was used to assess the effects of antifungal agents on vacuole acidification *in vivo*. Yeast cells from an overnight culture were inoculated into 5 ml of fresh YPD with FCZ (7 μg mL^{-1}), TBF (4 μg mL^{-1}) or control (1% DMSO). The cells with or without drugs were cultured for 5 h at 25 °C. After harvesting, the cells were suspended in 50 mM potassium phosphate buffer (pH 7.6) plus 2% glucose containing 500 μM quinacrine solution and incubated for 10 min. The cells were then washed three times with YPD and immediately observed under a fluorescence microscope using an aniline blue filter.

Zymolyase sensitivity test

To check the cell wall integrity, the zymolyase sensitivity test was performed as described previously (Vink *et al.*, 2002) with slight modifications. Briefly, the yeast strain (y13206: *pdr1*Δ*pdr3*Δ*snq2*Δ) was precultured in YPGal (the same composition as YPD, but with 2% galactose instead of 2% glucose) until log phase, and then resuspended in fresh YPGal at 1.5×10^7 cells mL^{-1}. Cells were incubated in fresh YPGal medium containing the test compounds in 96-well microtiter plates (CoStar®; Corning Incorporated, Corning, NY, USA) and incubated at 25 °C for 4 h with shaking. The compounds used were 4 μg mL^{-1} echinocandin B, 30 ng mL^{-1} micafungin, 100 mM concanamycin A, and 1% DMSO as the control. The cell pellets were washed twice with 10 mM Tris-HCl (pH 7.5) and resuspended in the same buffer containing Zymolyase 100T (Seikagaku, Japan) at 20 μg mL^{-1}. After an initial $OD_{600\ nm}$ measurement, samples were incubated at 30 °C, and the first $OD_{600\ nm}$ reading was taken after 30 min. Subsequent OD readings were recorded every 15 min for ~2 h using a plate reader (SPECTRAmax plus384; Molecular Devices, Sunnyvale,

CA, USA). In each sample, $OD_{600\ nm}$ values were standardized at time 0=1 (or 100%).

1.5 FIGURES

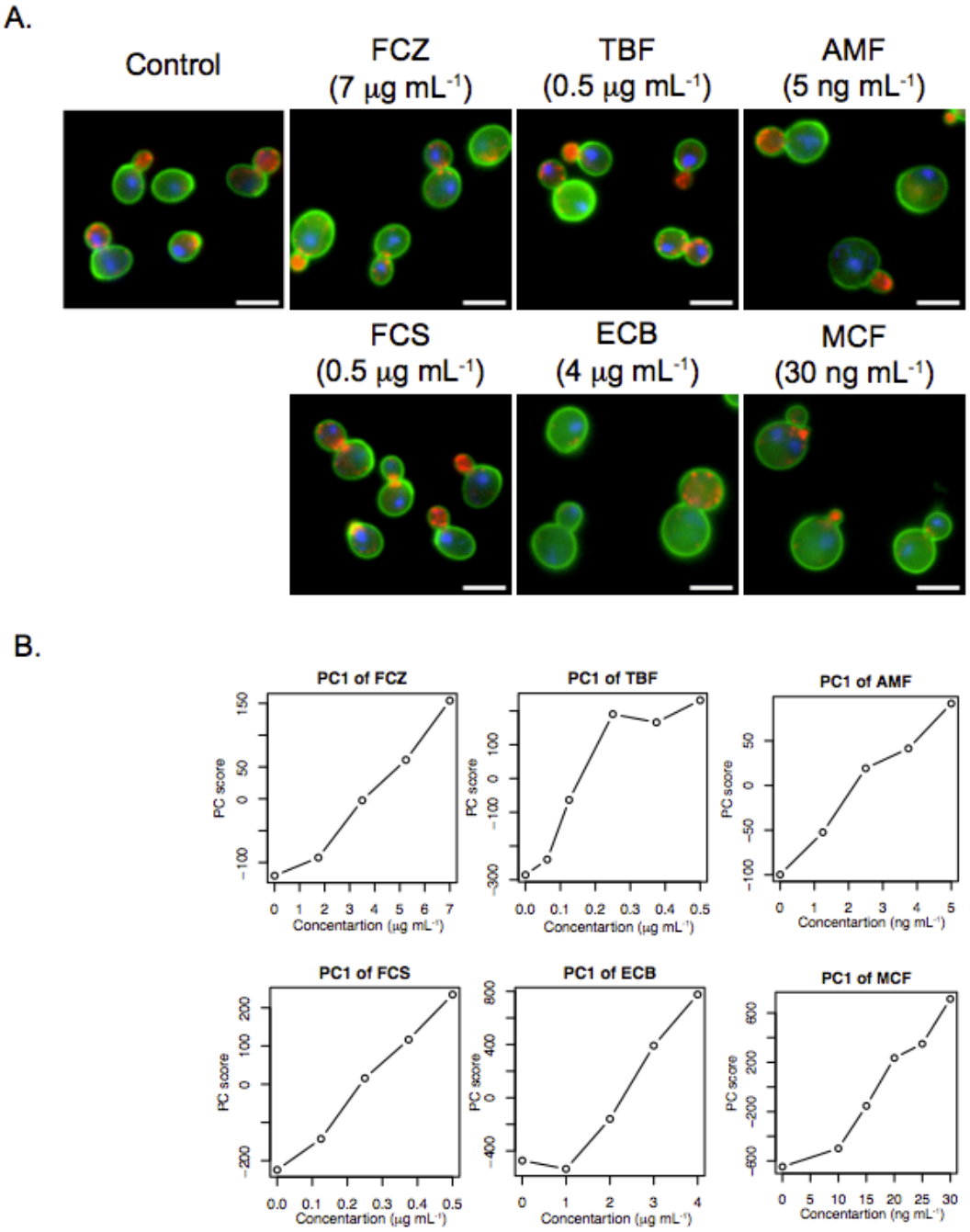

Figure 1-1. Dose-dependency of morphologic changes induced by treatment with antifungal agents.

Wild-type cells (BY4741) were cultured until the early log-phase at 25 °C in YPD medium with or without the indicated concentrations of antifungal drugs. Cells were triply stained with FITC-Con A, Rhodamine phalloidin, and DAPI to detect the cell wall, actin and nucleus, respectively. (A) Representative images at the indicated cell cycle stages from five independent experiments are shown. Scale bar, 5 μm. (B) Distribution of PC1 scores. Initially, some dose-dependent parameters of each drug were selected using the Jonkheere-Terpstra test (FDR = 0.05; Table S1). Morphological data from five replicates were standardized by the rank-sum method, and PC scores that made the greatest contribution to morphological features (PC1s) were plotted versus drug concentrations.

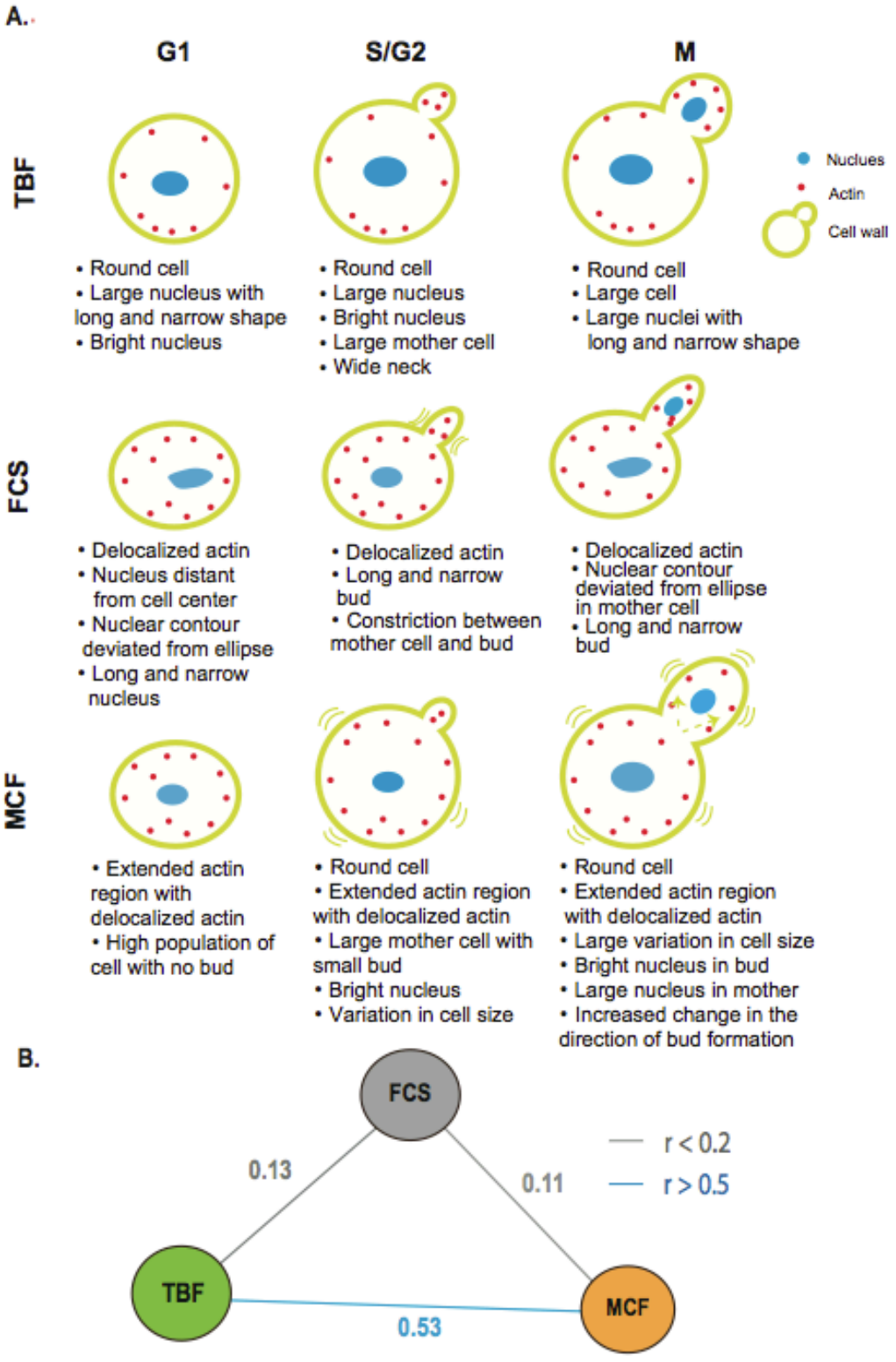

Figure 1-2. Morphological changes induced by typical antifungal agents of various classes.

(A) TBF, FCS and MCF were selected and exemplified as typical agents of each class. Morphological changes induced by the agents were extracted by PCA to identify representative parameters for each agent. Representative parameters used for illustration are summarized in Table S2. (B) To investigate the relationships among the representative antifungal agents TBF, FCS, and MCF, a correlational network map was constructed. The correl() function in Excel was used to calculate the coefficient of correlation among the morphological variables (PC scores) of the two drugs. The 102 PC scores of each agent were estimated by the algorithm used for morphological profiling. Light blue and gray lines, and scores near an individual line denote the degree of association: moderate ($R > 0.5$), weak ($R < 0.5$) or negligible ($R < 0.2$) relationship.

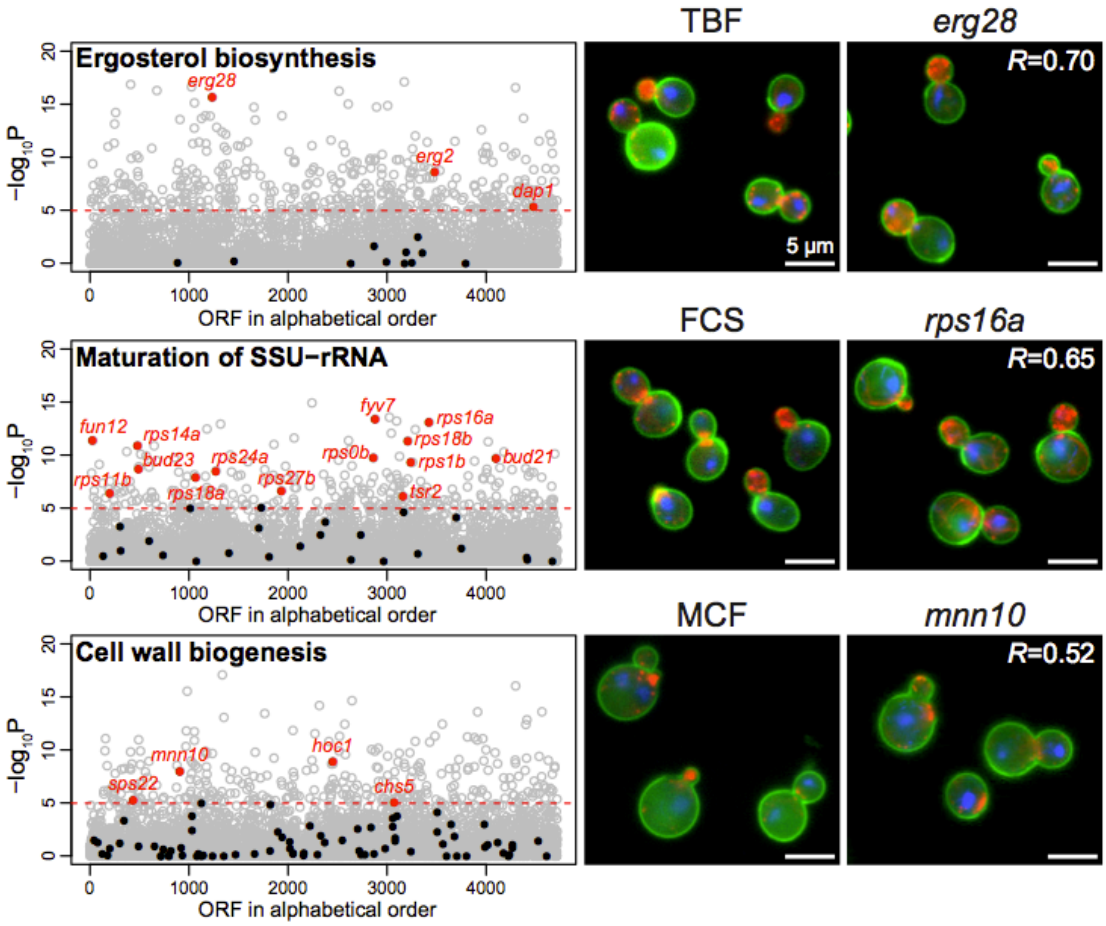

Figure 1-3. **Morphological profiling of ergosterol, cell wall and nucleic acid biosynthesis inhibitors**.

WT cells treated with different concentrations of each drug and the morphological profiles were compared with those of 4,718 non-essential gene deletion mutants, as described previously (Ohnuki *et al.*, 2010). The horizontal axis indicates each ORF in alphabetical order of the systemic name. The vertical axis represents –log10P (1-sided *P* value) of the similarity of the profiles between the drug treatment and each gene deletion. Red filled circles are genes that share significant similarity with those related to the GO terms "ergosterol biosynthesis," or "Vacuolar proton transporting V-type ATPase," or "maturation of SSU-rRNA," or "cell wall biogenesis." Black filled circles show genes that show insignificant similarity with drug treated cells.

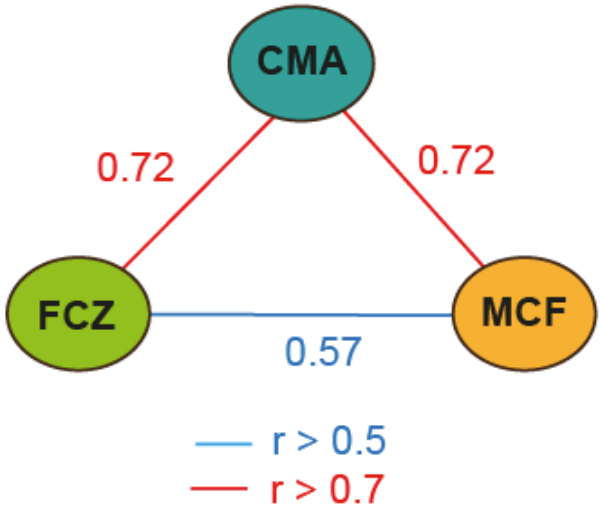

Figure 1-4 Correlation among ergosterol, V-ATPase, and cell wall biosynthesis inhibitors.

To build the network model, the correlation coefficient of the morphological profile between each pair of antimicrobial drugs was determined from 102 PC scores of a pair of agent considered as estimated by the morphological profiling approach. Red and light blue lines, and scores near an individual line denote the degree of association: strong (R > 0.70), or moderate (R > 0.50) correlation.

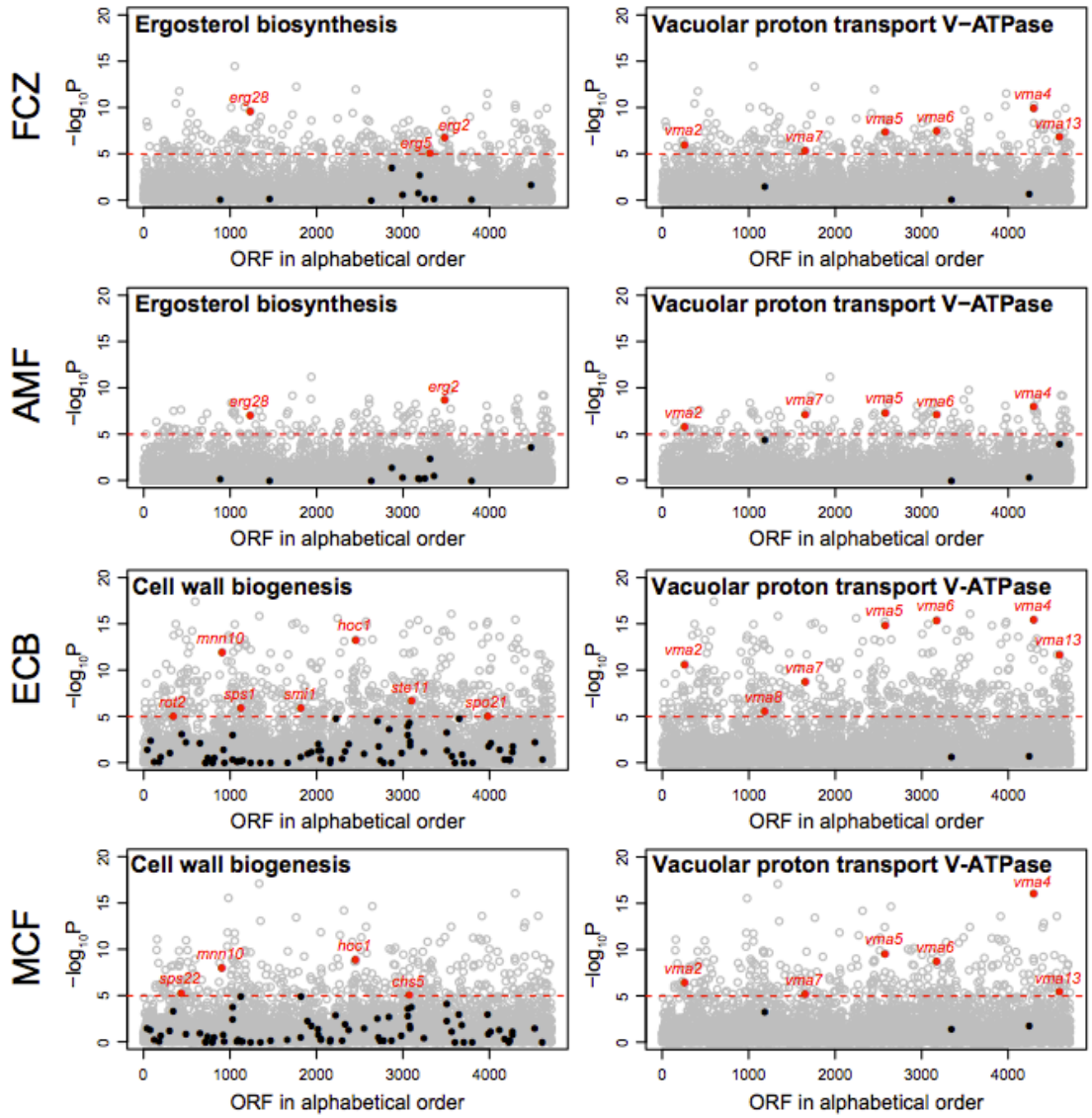

Figure 1-5. Morphological analysis of ergosterol, and cell wall biosynthesis inhibitors for V-ATPase mutants profile.

WT cells treated with several concentrations of each drug and the morphological profiles were compared with that of 4,718 non-essential gene deletion mutants, as described previously (Ohnuki *et al.*, 2010). The horizontal axis indicates each ORF in alphabetical order of the systemic name. The vertical axis represents –log10P (two-sided P value) of the similarity of the profiles between drug treatment and each gene deletion. Red circles are genes that share significant similarity to those related to the GO terms “ergosterol biosynthesis” (FCZ and AMF), or “cell wall biogenesis” (ECB), or “Vacuolar proton-transporting V-type ATPase” (FCZ, AMF, and ECB). Black filled circles show genes that show insignificant similarity with drug treated cells.

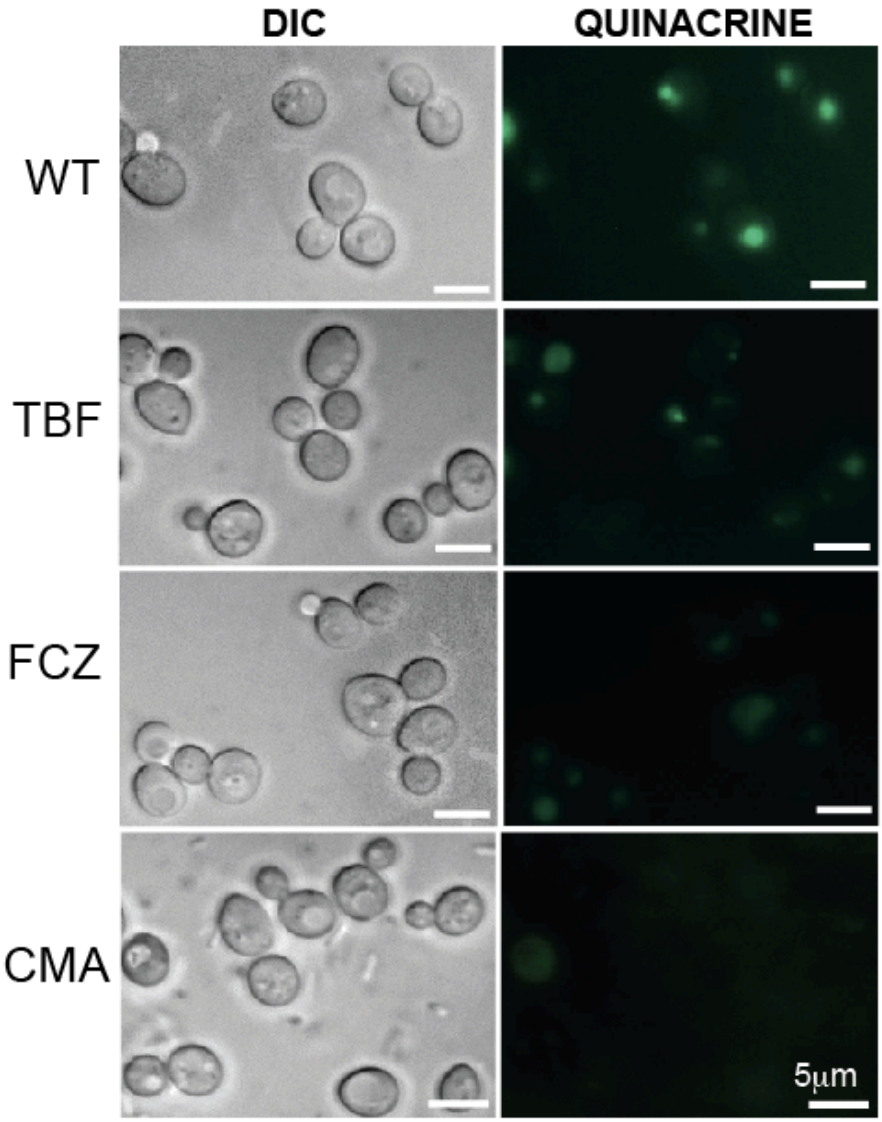

Figure 1-6. Treatment of budding yeast with ergosterol biosynthesis inhibitors disrupts V-ATPase function.

WT cells were grown in YPD for 16 h, and a small volume of the culture was inoculated into YPD without or with TBF or FCZ for 5 h followed by the addition of quinacrine (500 μM) for 15 min at 25 °C. Cells were then washed with YPD (pH 7.6). Fluorescence images of cells were obtained immediately after washings. The figure shows representative images of quinacrine-stained cells using the aniline blue filter (right panel) and Normarski photomicrographs of corresponding fields (left panel) of TBF-treated cells as representative images. As a control, the phenotype of mock- and CMA- treated WT cells is also shown. Bar: 5 μm.

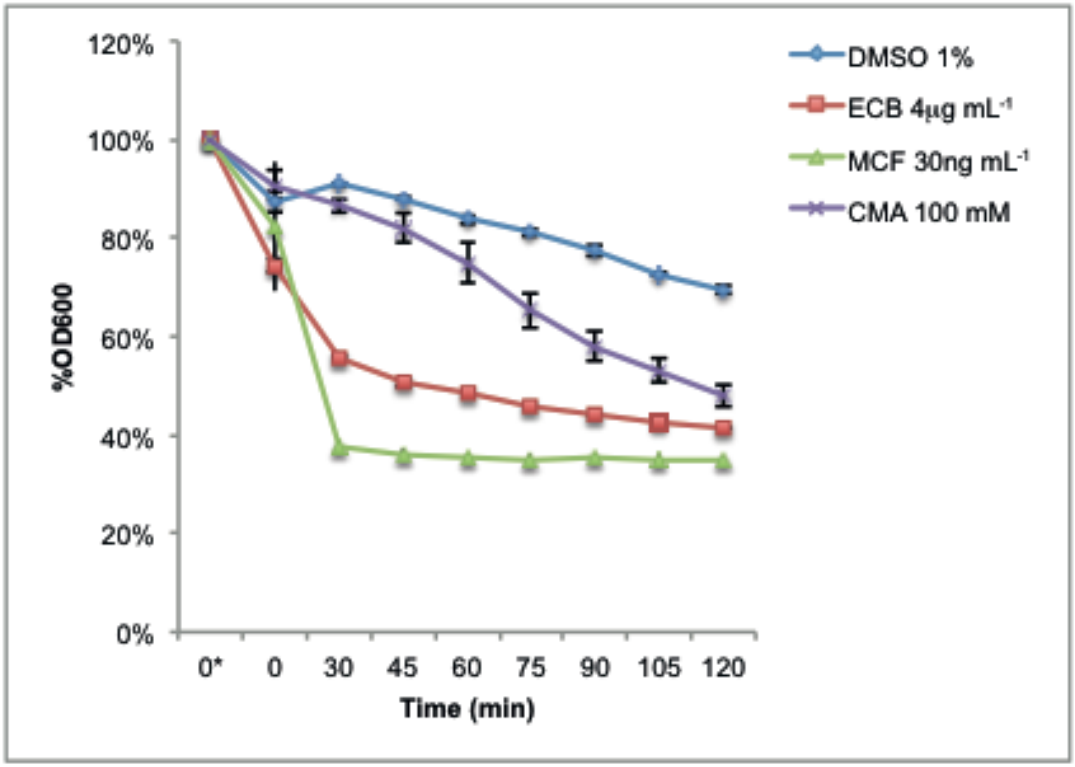

Figure 1-7. Sensitivity of V-ATPase and cell wall drug-treated cells to Zymolyase.

Yeast cells of the triple mutant strain (y13206) were treated for 4 h with concanamycin A (CMA, 100 nM), echinocandin B (ECB, 4 mg mL^{-1}) and micafungin (MCF, 30 ng mL^{-1}), prior to zymolyase assay. The $OD_{600\ nm}$ was determined before the addition of zymolyase (0* min) and was considered as an initial OD value. Thereafter, measurements were taken at addition (0 min), after 30 min of zymolyase addition and every 15 min thereafter for ~2 h. Cell lysis is expressed as the decrease in OD at 600 nm (as a percentage of the initial value (0*). Data are expressed as mean values of three independent experiments. Error bar: standard error of the mean.

1.6 TABLES

Table 1-1. Chemical compounds used in this study

Compound	Abbreviation	Stock solution	Treatment concentrations	Target cellular process
Fluconazole	FCZ	10 mg mL^{-1} methanol	0, 1.75, 3.5, 5.25, 7 μg mL^{-1}	Ergosterol biosynthesis
Terbinafine	TBF	10 mg mL^{-1} methanol	0, 0.0625, 0.125, 0.25, 0.375, 0.5 μg mL^{-1}	Ergosterol biosynthesis
Amorolfine	AMF	1 mg mL^{-1} methanol	0, 1.25, 2.5, 3.75, 5 ng mL^{-1}	Ergosterol biosynthesis
Flucytosine	FCS	2 mg mL^{-1} in DW	0, 0.125, 0.25, 0.375, 0.5 μg mL^{-1}	Nucleic acid biosynthesis
Micafungin	MCF	10 mg mL^{-1} in DW	0, 10, 15, 20, 25, 30 ng mL^{-1}	Cell wall biogenesis
Echinocandin B	ECB	2 mg mL^{-1} DMSO	0, 1, 2, 3, 4 μg mL^{-1}	Cell wall biogenesis

Table 1-2. Enrichment of vacuolar acidification defects from WT cells treated with ergosterol and cell wall drugs

Agent	GO category	GO term	P-value	Annotated Genes
FCZ	Process	Vacuolar acidification	1.31E-07	*VMA1, VMA3, VMA16, VMA5, VPH2, VMA6, VMA4, VMA11*
TBF	Process	Vacuolar acidification	3.12E-07	*VMA2, VMA1, VPS3, VMA3, VMA7, VMA16, VMA5, VPH2, VMA6, VMA4, VMA11*
AMF	Process	Vacuolar acidification	8.41E-08	*VMA2, VMA1, RRG1, RAV2, VMA3, VMA8, VMA7, VMA5, VPH2, MEH1, VMA6, VMA4, VMA11*
ECB	Process	Vacuolar acidification	6.10E-06	*VMA2, VMA3, VMA7, VMA16, RAV1, VMA5, VPH2, VMA6, VMA4, VMA11, VMA13*
MCF	Function	H^+-transmembrane transporter activity	0.00264	*VMA3, VMA5, VMA6, ATP18, VMA4, ATP4, VMA11, ATP15*

Chapter II: New Phenotypic Profiling Method for Identifying the Targets of Bioactive Compounds

2.1 INTRODUCTION

Antimicrobial drugs are indispensable for the prevention and treatment of disease. The history of drug development began in 1920's, when Fleming serendipitously discovered penicillin and a number of subsequent antimicrobial discoveries quickly followed, which ushered the golden era of antibiotics (Davies, 2006). The discovery of newer antifungal compounds continued but the progress has been relatively slow. This is partly because of increasing antifungal resistance, and to some extent also fungi are eukaryotes like mammalian cells. Consequently, rational drug designs directed at producing drugs have focused on identifying molecular targets, which are different or have no mammalian analog. For several decades, most of the drug discovery efforts have concentrated on target-based screens. However, less-biased phenotypic screening approaches shown promises in potentially improving success rates of drug development (Eggert, 2013; Schenone *et al.*, 2013).

Bioactive compounds interfere with fungal cellular activity by a number of different mechanisms; some of the compounds inhibit the growth of fungi (fungistatic activity) while some others kill the fungal cell (fungicidal effect). Based on their mode of action, there are a number of potential targets for antifungal treatment (Andriole, 1999). These include the compounds that interfere with cell wall synthesis, membrane sterol biosynthesis, metabolites, and nucleic acid synthesis. Despite this, more efficacious bioactive compounds, with novel biological activity and novel structures, are yet indispensable to combat various fungal infectious and tumor disease.

Identification of cellular target is the most important step in biological research and drug development as understanding the molecular targets of a compound can help elucidate its biological functions and potential pharmaceutical applications. Following the completion of the human genome sequencing, target-based screenings was considered to be the most rational and powerful approach for demonstration of dramatic clinical efficacy for emerging molecular-target drugs. However, the reintroduction of phenotypic approach as a complementary strategy for drug

discovery has sparkled renewed interest as it shown advantage especially in the exploration of first-in-class therapeutics (Swinney & Anthony, 2011). With the advancement of omics-based approaches, modified phenotypic screens such as the high-content imaging-driven methods emerged as vital tools in earlier steps of the small molecule discovery (Feng *et al.*, 2009; Houle *et al.*, 2010; Roti & Stegmaier, 2012). Our ability to analyze information on the possible molecular targets related to phenotypes determines the competency of identifying a compound with a specific mechanism of action and its efficacy. It is thus expected that a multidimensional phenotypic profiling approach supported either by genetics or the application of well-validated drugs can offer a promising strategy for discovering new drugs and defining their mechanisms of action. For example, the comparison between chemical-induced phenotypes and genetic perturbation proved a powerful tool to understand the MoA of antifungal agents (Ohnuki *et al.*, 2010). In spite of this, our current approach requires mutant information in advance. Therefore, it would be sagacious to consider complementary chemical genetic method that could overcome this setback.

In this study, I envisaged the development of a new method that classifies bioactive antimicrobial agents based on their difference in the phenotypic responses. This is made possible because of the fact that the morphological changes observed in cells treated with different classes of antifungal drugs are distinct from one another. I successfully established a systematic classifier that sorts antifungal agents into the three major classes: cell wall synthesis inhibitors, sterol biosynthesis inhibitors, and a nucleic acid synthesis inhibitor.

2.2 RESULTS

Classification of antifungal drugs by mode of action

I considered that the comparison between chemical-induced phenotypes and genetic perturbation is a powerful tool to understand the MoA of antifungal agents. However, for this purpose, I needed to obtain mutant information in advance. I report here a new method to classify antifungal agents without any mutant information by performing LDA on quantified morphological data. To that purpose, I summarized our image-profiling strategy into six analytical steps as shown in Figure 2-1 (see Materials and methods for the detailed algorithm). CalMorph analysis was executed on fluorescence microscopic images to obtain quantified morphological data for each drug considered

(Step 1). Before applying LDA, I analyzed the multidimensional drug data with GLM (Step 2A), and the resulting figures were designated as specific phenotypic descriptors. The machine supervised with response descriptors of six drug data sets yielded a learned machine that could discriminate drugs according to their MoA (Step 3). Next, GLM was performed on random samples derived from each drug data set (Step 2B). This test data set was used to validate the efficiency of the learning machine (Step 4). Selection of the best classifier was accomplished using the overall cyclic processes of optimization (Step 5). Eventually, the morphological profiling results from the projection of test compounds onto the best classifiers (Step 6) were visualized in 2D-phenotypic space.

The training algorithm was applied to the high content data of FCZ, TBF, AMF, FCS, ECB, and MCF (Table 1-1), and the resulting LD scores of the phenotypic responses were depicted on 2D space to visually classify the features of each agent (Fig. 2-2A). I can see that the first linear discriminant (LD1) separated the classes quite well, but the second linear discriminant (LD2) added less valuable information. In this space, the color-filled circles represent the distribution of the six drugs from the three classes; solid arrows represent the direction of training data separation by the LDA. Therein, drugs that have similar activities formed a cluster at a specific distance from the center. Cross validation of the test set showed clustering of nearly all of the test data points around the six points of the training data set (Fig. 2-2A). In this figure, the diamond symbols denote median points of the test data, and the dashed arrows show the directions of the test data set separation. Even if the distance of the median points of the training and test sets from the center are different, the direction is similar. In this space, specific phenotypic responses were shown as a distinct cluster distribution. The results suggested that the classification of antifungal agents based on the morphological profiles of the three classes reflects their intracellular MoA.

Classification of other antifungal agents

In our machine learning approach, I anticipate that when the test agents form a group with a particular training set compound, they are likely to have similar cellular targets. To evaluate our proposed method, I selected a well-characterized drug set containing 10 antifungal agents as “target unknown” drugs data (Table 2-1). The profiles of

phenotypic multiparameters of these test compounds were visualized in 2D scatter plot. The possible target drug class to which a given compound of interest may belong was determined based on their posterior probability scores. Intriguingly, an optimized classifier assigned nearly all of the agents into the three categories with the highest posterior probability > 0.90 (Fig. 2-2; Table 2-1), indicating that well-characterized drugs were classified by MoA.

Classification of other antifungal agents: cell wall-affecting drugs

Of the bioactive test compounds, our image-profiling method suggested that caffeine (CAF) and nikkomycin Z (NMZ) were significantly associated with a cluster of distinguished cell wall-disrupting drugs, echinocandin B and micafungin (Fig. 2-2B). Essentially, both CAF and NMZ are known to affect the yeast cell wall. CAF is an analog of purine bases that induces alteration in the yeast cell wall architecture (Levin, 2005; Kuranda *et al.*, 2006). NMZ is a competitive inhibitor of chitin synthases in fungi (Gaughran *et al.*, 1994). Thus, our machine learning method was successful in profiling cell wall-affecting drugs based on their specific phenotypic response.

Classification of other antifungal agents: nucleic acid-acting drugs

Some of the nucleic acid synthesis-interfering compounds—such as hydroxyurea (HXU), bleomycin (BMC), tunicamycin (TCM), and hygromycin B (HYG)—were classified along with FCS, an inhibitor of fungal DNA and RNA synthesis and protein translation (Waldorf & Polak, 1983) (Fig. 2-2B). HXU is an antitumor agent with antileukemic activity, causing the inhibition of ribonucleotide reductase activity and consequent suppression of DNA synthesis (Chang & Cheng, 1978). BMC binds to DNA and causes single- and double-strand breaks catalytically, resulting in inhibition of DNA biosynthesis (Chen & Stubbe, 2005). TCM is known to affect N-glycosylation, but it also causes G1 arrest of *S. cerevisiae* cells in the unbudded phase and prevents initiation of DNA synthesis (Vai *et al.*, 1987). HYG is an aminoglycosidic agent that inhibits protein synthesis by disrupting translocation and

promoting mistranslation at the 80S ribosome(Ahmad *et al.*, 1980). This similarity in their MoAs might have induced similar morphological profiles.

Classification of other antifungal agents: ergosterol-affecting drugs

Miconazole (MCZ) and amorolfine (AMF), which interfere with the fungal sterol synthetic pathway (Shah Alam Bhuiyan *et al.*, 2007; Isham & Ghannoum, 2010), were classified into the cluster of ergosterol synthesis inhibitors (Fig. 2-2B; Fig. S3). MCZ inhibits ergosterol biosynthesis at the step of sterol 14α-demethylase in the ergosterol biosynthetic pathway (Ghannoum & Rice, 1999). However, AMF blocks the same pathway at the step of Δ^{14} reductase and Δ^{7}-Δ^{8} isomerase (Shah Alam Bhuiyan *et al.*, 2007). Therefore, it is conceivable that the data of these agents were plotted at or nearby the cluster organized by the ergosterol biosynthesis inhibitors (Fig. 2-2B). Lovastatin (LVS) is another drug that inhibits ergosterol biosynthesis (Fig. S3). Independent of its hydroxymethyl glutaryl-CoA reductase inhibition (Alberts *et al.*, 1980), LVS reduces proteasome activity, leading to G1 phase arrest (Rao *et al.*, 1999). The newly established method plotted LVS in the space between the clusters of ergosterol- and nucleic acid- synthesis interfering agents (Fig. 2-2B), indicating that the high-content system was successful in profiling phenotypes by drug function.

2.3 DISCUSSION

I analyzed the image-based morphological profiling of the currently available antifungal agents and developed a new profiling method that facilitates the prediction of drug targets. The system uses quantified multiparametric data based on morphological alterations induced by a candidate drug. Most of the drugs were classified into the three training set groups, indicating the system can successfully recognize the morphological changes of a drug and group them into drugs with similar MoAs. The designed method identifies the biological targets of a compound of interest without relying on any mutant information in advance. In the current situation in which I only have a reference dataset for non-essential mutants, this approach can also be used for the prediction of essential gene targets of a certain compound. A similar approach can be applicable to higher eukaryotes once the system is established in the budding yeast, a proven model organism for studying related human diseases.

Thus, my results suggest the potential use of this new profiling method as an interesting powerful tool to predict the target of a small molecule of interest.

Comparison with the fitness profiling approach

The multimorphic method employed 501 morphologic parameters to predict drug targets. A comparable method, such as fitness profiling, which employs growth as a primary phenotypic descriptor, has been developed in yeast chemical genomic studies. The fitness approach identifies the likely target of a given compound in two discrete assays—haploinsufficient profiling (HIP) and homozygous profiling (HOP). In the HIP assay, essential gene targets of a certain compound of interest could be identified from the fitness data of the heterozygote strain deleted for the drug target (Giaever *et al.*, 1999; Lum *et al.*, 2004; Lee *et al.*, 2005). In HOP, growth data from a complete loss-of-function deletion in a diploid strain allow identification of non-essential gene targets of a compound (Parsons *et al.*, 2004, 2006; Dudley *et al.*, 2005; Fry *et al.*, 2005). Unlike fitness profiling, our profiling system facilitates genome-wide target assessment from multidimensional cellular responses caused by the drugs in a systematic manner once the training database is sufficiently diverse. Therefore, morphological profiling and fitness profiling are complementary, and serve as new drug-prediction tools.

Comparison with other image-profiling approaches

Our chemical genomics research wing focuses on developing various methods for drug target prediction based either on the assumption that chemicals should phenocopy the mutation or screening drugs that share similar perturbation profiles. In Chapter one, I reported a method of exploring the cellular functions affected by candidate compounds by comparing with the phenotypes of yeast non-essential gene-deletion mutants (Ohnuki *et al.*, 2010). Therein, several functionally related genes, and potentially affected cellular pathways, were identified in addition to previously known target genes of studied compounds. This approach was limited in its ability to cross-examine all relevant gene targets because it interrogates only nonessential gene targets; no information related to essential genes could consequently be inferred. The new method developed in this study was a complementary approach, enabling us to extrapolate a drug target and other pertinent information without any reliance on a

mutant database. The machine learning technique sorts a new compound into a class of drug with a similar MoA, defining the MoA of the compound from different viewpoints. Remarkably, the combinatory usage of these two image-profiling methods has allowed us to leverage the scale of our study by not only identifying candidates of drug targets but also mapping detailed phenotypic information on the cellular response to any conditions that may induce morphologic changes.

Application of linear classification models for drug discovery

In this study, I developed the method that learns phenotypic profiles induced by the drugs of training set and classifies bioactive substances. Our profiling system involves a simple procedure involving triple staining of the cells (the cell wall, DNA and actin), extracting high-dimensional phenotypic data using CalMorph, and sorting compounds into a class with a similar MoA. Another chemical-genetic phenotype profiling approach, morphobase (Futamura *et al.*, 2012), was developed using the images of mammalian cells. Morphobase strategy engages PCA and similarity search software to detect targets of a candidate small molecule. Our expedient image-profiling tool employs LDA, which performs dimensionality reduction while preserving as much of the class discriminatory information as possible, attempting to explicitly model the differences among the classes of data (Swets, 1996; Martinez & Kak, 2001; James, 2012). LDA best discriminates up to three classes, yet can achieve average classification accuracies of above 80% for a number of classes until four (Castro, 2012). To create a quantitative structure–activity relationship model and identify new compounds from molecular topology databases, other studies used LDA and multiple linear regression (Gozalbes *et al.*, 2000; Mahmoudi *et al.*, 2006, 2008). Their model could discriminate between inactive and active compounds by learning the drug's structural patterns. This approach and our method are both powerful in target prediction and deduced biological information despite the difference in screening criteria (*e.g.*, structure *vs.* phenotype) used and number of features involved (Gozalbes *et al.*, 2000; Ohya *et al.*, 2005).

New insights into mode of action of some bioactive compounds

Intriguingly, the systematic classifier drew new insights into antifungal agents. For example, miconazole was assigned to ergosterol biosynthesis inhibitors, but plotted near DNA affecting agents' class. Recent mechanistic studies (Najm *et al.*, 2015) showed that miconazole affects pathways regulating DNA synthesis via interfering the role of mitogen-activated protein (MAPK)/extracellular signal-regulated kinase (ERK) signaling in estrogen receptor positive MCF-7 breast carcinoma cells. This suggests the power of the method in efficiently indicating drugs MoA from their morphologic signatures. Moreover, since LVS is another drug that acts in a mevalonate synthesis pathway, I expected it to be sorted into the ergosterol biosynthesis inhibitors. Although lovastatin is plotted in the clusters of ergosterol affecting agents, functionally classified as nucleic acid biosynthesis inhibitors (Fig. 2-2). As such, I presumed that LVS might be a drug that exerts dual effect on yeast cellular processes. Research evidences showed that independent of its hydroxymethyl glutaryl-CoA reductase inhibition (Alberts *et al.*, 1980), LVS reduces proteasome activity thereby leading to G1 phase arrest (Rao *et al.*, 1999). Furthermore, considering its MoA, I expected CMA, potent V-ATPase inhibitor (Dröse *et al.*, 1993), to be classified into either ergosterol or cell wall synthesis inhibitors. However, it was notably ascribed to a different drug group - nucleic acid inhibitors (Fig. 2.2). Consequently, I thought it was unfortunately misclassified at that time. To my surprise, a very recent research evidences demonstrated an unexpected finding that the yeast vacuole plays a positive essential role in initiation of the cell-cycle and its functional loss results in a specific arrest of cells in G1 phase (Jin & Weisman, 2015). Taken together, these data indicate that high-content system was successful in profiling phenotype by drug function.

In general, though the target prediction process went well with the training compounds considered, the cluster representing ergosterol and nucleic acid seems to get closer to each other. This might reflect the limitation of such linear methods as LDA. To increase its discrimination power, nonlinear multiclass models such as neural networks can be used as a supervised classification technique (Terfloth & Gasteiger, 2001; Concu *et al.*, 2010). Moreover, our profiling technique is a quantitative morphology-based system that attempts for the first time to use LDA for drug target prediction starting with a small training data set. Expanding the compound

database of diverse therapeutic categories could enhance the effectiveness of this image-profiling technology.

2.4 MATERIALS AND METHODS

Antimicrobial agents

The following is the list of compounds analyzed, their acronyms and suppliers: Lovastatin (LVS; Wako Pure Chemical Industries, Osaka, Japan), concanamycin A (CMA; Sigma-Aldrich), tunicamycin (TCM; Sigma-Aldrich), bleomycin (BMC; Sigma-Aldrich), hydroxyurea (HXU; Sigma-Aldrich), miconazole (MCZ; Sigma-Aldrich), hygromycin B (HYG; Wako), caffeine (CAF; Nacalai tesque, Kyoto, Japan) and nikkomycin Z (NMZ; Sigma-Aldrich). Stock concentrations and solution preparation methods are summarized in Table 1-1 and Table 2-1 for training and test compounds sets, respectively.

Culture conditions and data acquisition for morphological analysis

As in first chapter, drug treatment experiments was conducted using haploid wild-type (WT) yeast strain; BY4741 (*MAT*a; *his3*Δ1 *leu2*Δ0 *met15*Δ0 *ura3*Δ0). Yeast culture condition, and morphological data acquisition was performed as described in first chapter of this dissertation.

Linear discriminant analysis

Linear discriminant analysis (LDA) is a machine learning method that generates a classifier based on the combination of variables that best predicts the group to which a given compound belongs. LDA best separates two or more classes (Friedman, 1989). To classify and show the difference of the three classes of antifungal agents, I performed LDA as indicated in the following six principal steps.

Step 1. CalMorph analysis. Yeast cells were treated with serial concentrations of antifungal agents and triply stained with fluoroscienisothiocyanate labeled concanavalin A (FITC-ConA), Rhodamine-phalloidin, and 4',6-diamidino-2-phenylindole (DAPI) to obtain fluorescent images of the cell wall, actin cytoskeleton, and nuclear DNA, respectively. To describe the cellular responses using quantitative values, fluorescent images were analyzed using CalMorph, which generated

quantified 501 morphological parameters for each drug set. The mean values in each parameter were calculated from at least 200 individual cells treated with six different antifungal agents as specific phenotypic descriptors.

Step 2. Performing the Generalized Linear Model (GLM). I applied the GLM, a flexible generalization of ordinary linear regression (Nelder & Wedderburn, 1972), to estimate the dose-dependency of the data. The probability distribution functions and the link functions to estimate the effects of a drug on cell morphology in each parameter was used as described in Yang *et al.* (2014). I subjected the training and test data sets to GLM as follows.

Step 2A. GLM on the training data. For the training data set, effects of six well-known drugs from the three classes were used as a supervisor for the machine learning. The Z value of the Wald test for dose-dependency (a fixed effect of a drug treatment) in each parameter was calculated by simple linear regression with GLM between five or six concentrations of the drug treatment and parameter values (five replications in each concentration). The number of Z values was six for each parameter: three for ergosterol (FCZ, AFM &TBF), 1 for DNA (FCS), and two for cell wall (MCF & ECB) drugs.

Step 2B. GLM on the test data. Regarding the test data set for cross validation, Z values of the Wald test for the dose-dependency in each parameter were estimated by simple linear regression with GLM between the drug concentrations and parameter values of three replicates randomly selected from the five replicates of each concentration. The number of Z values calculated in the test data was 1,500 for each class (4,500 in total) in each parameter: FCZ, AMF & TBF: 500; FCS: 1,500; MCF & ECB: 750. Before implementing LDA, Z values of both training and test data set were superimposed onto 122 PCA-rotated replicated WT morphological data sets.

Step 3. Machine learning

At first, one pair of PCs among all pairs of 122 PCs (7,381 combinations) was selected for the classifier that can discriminate among drugs with different mechanisms of action. Next, to enhance the efficiency of sorting, a third possible partnering PC was similarly selected from the remaining 120 PCs. Using

combinations of the three PCs, the classifier was calculated by supervising the machine with a training data set (n = 6).

Step 4: Cross-validation

Validation of the classifier was accomplished by the accuracy estimated from a 3 × 3 contingency table among three categories of the six drugs and predicted categories by the classifier with the test data set (n = 4500). Projection of test data set resulted in a cross-validated learning machine.

Step 5. Optimization

Repeated processes of selecting PC combination, calculation of a classifier by instructing the machine with the training data set using selected PCs, and validation of the classifier with the test data set consequently generates the optimum classifier. The morphological parameters attributed to the three best PCs that produced optimum drug classifier (PC63, PC77 & PC54) were determined by estimating the association between PC and Z values of the training data set using cor.test() function. The parameters were detected at false discovery rate (FDR) of 0.1 estimated by qvalue() function in R package (Storey, 2002). The list of contributing parameters is shown in table S4.

Step 6. Superimposing the test compounds

The Z values of test compounds were computed using GLM, the values were projected to 122 PCA-rotated WT data, and the resulting PCs were superimposed onto the best classifier. The generated linear discriminant (LD) scores were displayed in two-dimensional (2D) phenotypic space. Posterior probability scores defined the target prediction of a test compound.

2.5 FIGURES

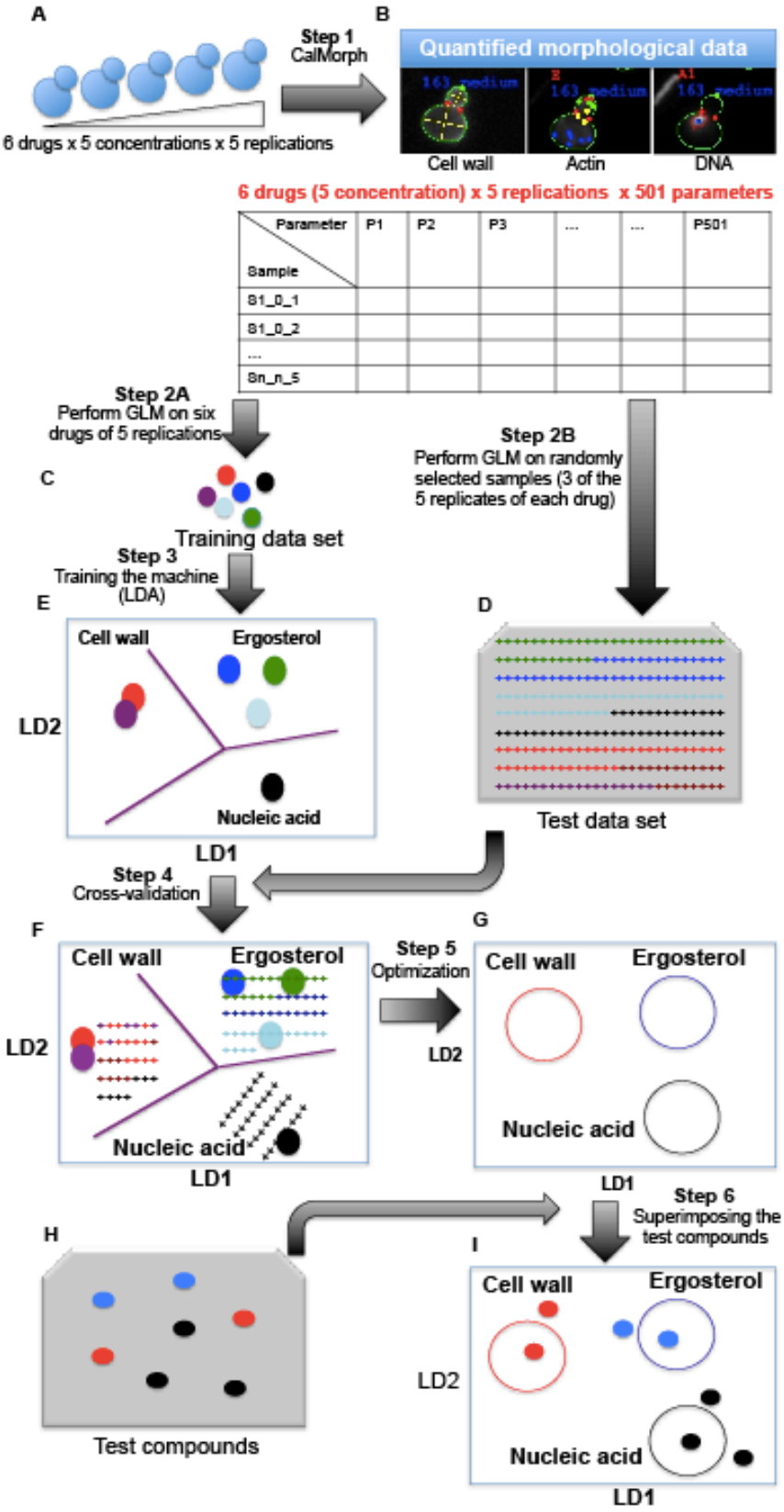

Figure 2-1. Schematic illustration of new phenotypic profiling method.

The image-based antifungal drug profiling technique involves six principal steps, as described in the Results and Materials and Methods. Images from A-I denote the following: (A) Dose-dependent antifungal agent treatment of yeast cells; (B) CalMorph-processed morphological data of triply stained cells; (C) Training data set represented in six different colors; (D) Test data set generated from random samples; (E) Output of machine learning; (F) Result of cross-validation; (G) Optimum systematic classifier; (H) Test compound to be profiled by the best classifier; (I) the results of target prediction.

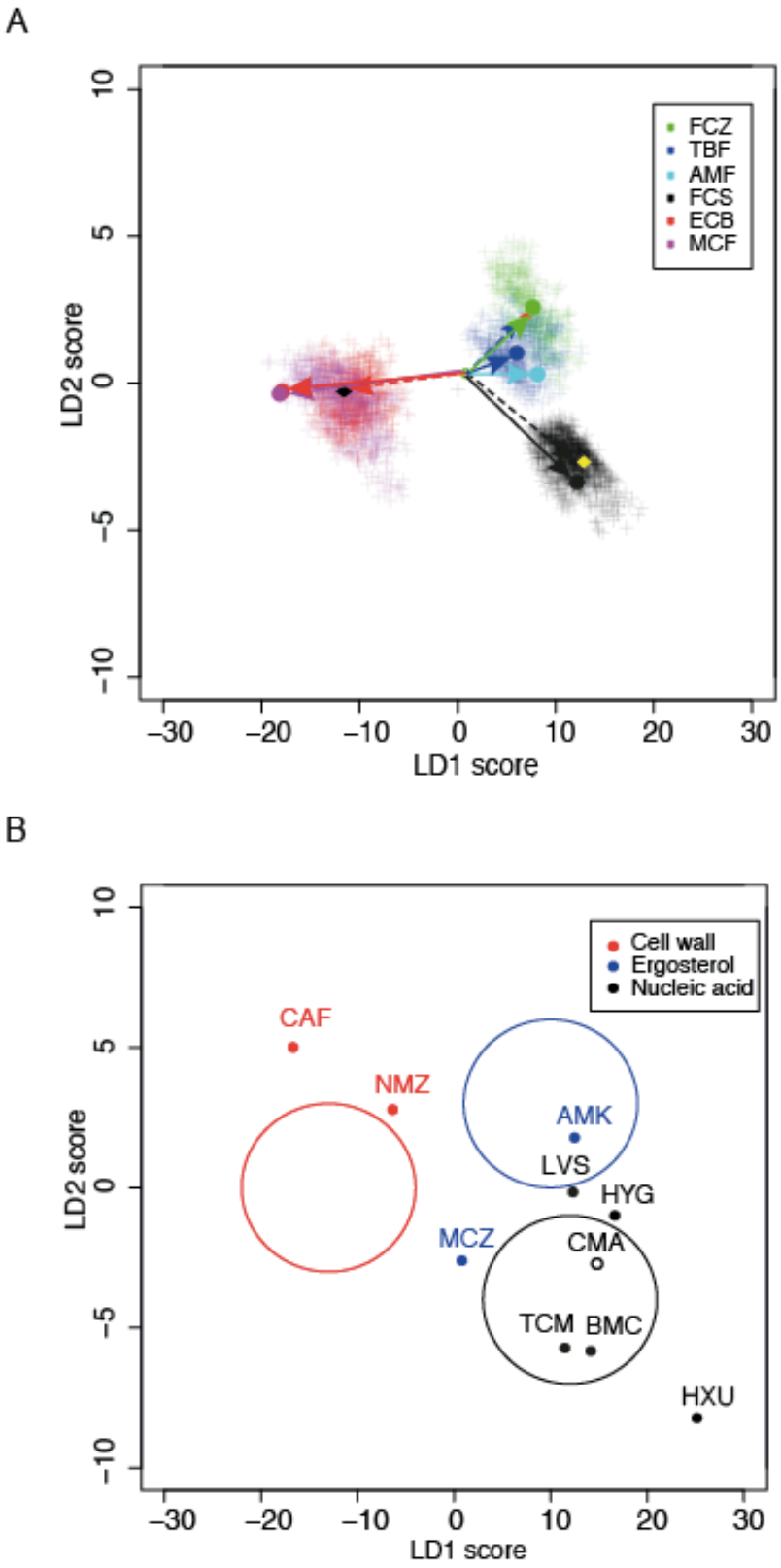

Figure 2-2. Classification of antifungal drugs based on their morphological profile differences in 2D-phenotypic space.

(A) The clustering pattern of the test data set around six data points of the training set from antifungal agents of three distinct classes. Clusters represent the test data distribution of the cell wall (red, left side), ergosterol (green, middle), and nucleic acid (black, right side) acting drugs respectively. Training data (filled circles); test data median points for each drug class (diamond symbol). The positions of the median points for the test data (dashed arrow), and training data (solid arrow) from the center (green open circle; average of posterior probability scores) are indicated. (B) Target profiling of test antifungal compounds. A biplot shows classification of the test compounds into different classes with similar mechanisms of action by the optimum classifier. LD1 & LD2: linear discriminant functions 1 & 2; larger circle (test data distribution), small circles (exact position of each test compound), small filled circle (correctly classified), and small open circle (incorrectly classified).

2.6 TABLES

Table 2-1 Antimicrobial drugs used as test compounds in this study

Compound	Abbreviation	Stock solution	Treatment concentrations	Target cellular process
Caffeine	CAF	10 mg/ml in DW	0, 197.5, 296.3, 444, 666, 1000 μg/ml	Cell wall biogenesis
Nikkomycin Z	NMZ	10 mM in DW	0, 80, 160, 240, 320, 400 μM	Cell wall biogenesis
Miconazole	MCZ	10 μM in DMSO	0, 2, 4, 6, 8 nM	Ergosterol biosynthesis
Concanamycin A	CMA	100 μM in DMSO	0, 2, 3.9, 7.8, 15 μM	V-ATPase
Lovastatin	LVS	20 mg/ml in ethanolic NaOH*	0, 6.25, 12.5, 25, 50 μg/ml	Mevalonate synthesis
Tunicamycin	TCM	10 mg/ml DMSO	0, 20, 40, 60, 80, 100 ng/ml	Glycoprotein synthesis
Hygromycin B	HYG	5 mg/ml DW	0, 0.78, 1.56, 3.13, 6.25, 12.5 μg/ml	Macromolecular biosynthesis
Hydroxyurea	HXU	2M in DW	0, 10, 15, 20, 25, 30 nM	Macromolecular synthesis
Bleomycin	BMC	1 mg/ml DW	0, 31.3, 62.5, 125, 250, 500 ng/ml	Nucleic acid biosynthesis

*Contains 15% (v/v) Ethanol and 0.25% NaOH

Table 2-2 Comparison of the predictions of target-unknown drug classes by LDA analysis versus experimental research evidence

Drug	**Abbreviation**	**Predicted drug class**	**Target, mechanism of action and/or function**	**References**
Caffeine	CAF	Cell wall	Blocks cell wall biosynthesis	Levin (2005); Kuranda *et al.* (2006)
Nikkomycin Z	NMZ	Cell wall	Inhibits chitin synthase of *Saccharomyces cerevisiae*	Gaughran *et al.* (1994)
Miconazole	MCZ	Ergosterol	Blocks the biosynthesis of ergosterol, inhibits sterol 14α-demethylase	Ghannoum & Rice (1999)
Amorolfine	AMK*	Ergosterol	Inhibits Δ14 reductase and Δ7-Δ8 isomerase	Shah Alam Bhuiyan *et al.* (2007)
Lovastatin	LVS	Ergosterol/ Nucleic acid	HMG-CoA synthase inhibitor; disrupts the cholesterol synthesis pathway; Mediates G1 arrest via inhibition of proteasome	Alberts *et al.* 1980; Rao *et al.* (1999)
Tunicamycin	TCM	Nucleic acid	Affects bud emergence and initiation of DNA synthesis; Inhibitor of yeast glycoprotein synthesis	Kuo & Lampen (1974); Vai *et al.* (1987)
Hygromycin B	HYG	Nucleic acid	Inhibiting protein synthesis; Stabilizes the tRNA-ribosomal acceptor site, thereby inhibiting translocation	Borovinskaya *et al.* (2008); Shoji *et al.* (2009)
Hydroxyurea	HXU	Nucleic acid	Inhibits DNA synthesis; Reduces mRNA levels of small subunit of ribonucleotide reductase (RNR2)	Timson, (1975); Moore & Hurlbert (1985)
Bleomycin	BMC	Nucleic acid	DNA fragmenting agent	Chen & Stubbe (2005)
Concanamycin A	CMA	Nucleic acid	Inhibits vacuolar-type H^+-ATPases	Dröse *et al.* (1993)

*AMK – Amorolfine data acquired in different experiment

CHAPTER III: Sensitive and High-throughput Profiling of the Responses of Antimicrobial Agents from Single Cells

3.1 INTRODUCTION

Antimicrobial drug development is a time-consuming and costly process. The most challenging but crucial aspect of antimicrobial drug research is elucidating the mode of action and cellular targets of new compounds (Livermore, 2011; Futamura *et al.*, 2013b). Much of the difficulty in identifying the mode of action of putative bioactive compounds emerges from the complexity and interrelationship of the cellular system (Toledo-Arana & Solano, 2010), the existence of multiple targets (Rix & Superti-Furga, 2009; Silver, 2011), and the pleiotropic effects of target genes (Kohanski *et al.*, 2010; Toledo‐Arana & Solano, 2010). Profiling multimetric phenotypic signatures of small molecules proved useful in offering substantial insights into their mechanisms of action, a systems level understanding of biological pathways (targets) and their responses to drug treatments including uncharacterized ones. It thus deserves due emphasis in the drug discovery process especially at an early step.

Cell-based screens are increasingly being used in drug discovery pipeline to assess drug responses of signalling pathways because they properly reflect the complexity of the cell than target-based approaches (Fishman & Porter, 2005). Among others, high-throughput image analysis is becoming a powerful tool for drug target identification, and compound lead selection (Perlman *et al.*, 2004; Lang *et al*., 2006). First, the availability of yeast *S. cerevisiae* as a eukaryotic cell model of choice for high-throughput phenotyping has facilitated phenotypic drug discovery process. This is mainly due to its ease of manipulation and genetic tractability, inexpensiveness to maintain and grow, many of its core cellular process conserved in humans (Botstein *et al.*, 1997; Botstein & Fink, 2011). To this end, researchers have unparalleled breadth of reagents to interrogate the yeast genome as its strains are ideal to model disease state in human cells and for studying conserved targets and mechanisms of basic biological processes (St Onge *et al.*, 2012). Second, increased availability of automated fluorescence microscopy, supercomputing facilities, and advances in molecular labeling has enabled the advancement of high-throughput image-based

assays (Price *et al.*, 2002; Zhou & Wong, 2006). Such assays have impressively empowered large-scale phenotyping of single cells including cellular morphology. Finding of new therapeutics from vast natural products using high-throughput screening shall, however, meet various challenges. For example, the development of natural products is hampered by a lack of a mechanistic understanding of their molecular action and identifying the potential targets associated with a bioactive small molecule, among others.

Diverse genomic and genetic tools of for the advancement of genome-wide studies in *S. cerevisiae* have so far been developed (Luesch *et al.*, 2005; Bharucha & Kumar, 2007). As part and parcel of the scientific development, our chemical genomics research has predominantly focused on developing tools for drug target prediction, which is based either on the assumption that chemicals should phenocopy the mutation, or screening drugs that share similar perturbation profiles. Ohnuki *et al*. (2010) reported a method of exploring the cellular functions affected by candidate compounds by comparing with the phenotypes of yeast non-essential gene-deletion mutants. Later, as an alternative to the current system, I developed a high-content method that profiles genetic targets of an antifungal compound without relying on any mutant information in advance (Gebre *et al.*, 2015). Despite these developments, relatively high concentration of drugs is needed because wild-type yeast cells are treated with drugs. As a result, quite a number of abundance -limited natural products have largely been prone to exclusion from characterization via high-throughput profiling strategies. To enhance the value of the high-throughput screening paradigm for the discovery of new therapeutics, new efficient systems are highly demanded. The use of alternative resources that may increase compound efficiency and further diminishes is hence of paramount importance in this regards.

Nowadays, resistance to multiple drugs becomes one of the major concerns in the areas of antibiotics and antifungal drug development. The major mechanism responsible for increased resistance to drug (*e.g.* azole) in clinical *Candida* isolates is drug efflux mediated by plasma membrane transporters (Rogers & Barker, 2003; Holmes *et al.*, 2008). Consequently, it is supposed that knocking out these transporters in model systems background could facilitate the drug discovery at

reduced amount of a given compound. In this study, I envisaged developing a new, efficient image-profiling tool for high-throughput drug discovery. To that purpose, an integrated profiling method was proposed to combine hypersensitive strains and high-throughput microscopy through high statistical power as a great tool for connecting low-abundance natural compounds to their biological targets and pathways. The introduction of new yeast deletion mutant dataset that compromised the cell's ability to efflux toxic compounds allows the use of small amount of compound compared to wild type. Besides, a high-content microscopy is used as one of the faucets of integrated approach to enable large-scale screening of chemical library. Furthermore, high power statistical approach that accommodates the non-normally distributed data, a generalized linear model (GLM), was utilized for the analysis of dose response morphological data. As a proof-of-concept study, I employed six standard compounds to demonstrate its applicability for the discovery of new drug. My profiling system successfully identified the targets of those compounds and potentially affected cellular pathways, demonstrating the validity of this approach.

3.2 RESULTS

The sensitivity of morphological dataset

In this study, I considered using a collection of *S. cerevisiae* with drug-hypersensitive background to establish new morphological dataset. Thus, first I examined the morphological changes in a triple mutant (*pdr1Δpdr3Δsnq2Δ*, hereafter designated as "TM") background strain compared to its isogenic wild type (Fig. 3-1). Visual inspection revealed the triple mutant yeast is different in the morphological traits compared to the WT (Fig. 3-1A). Quantitative phenotypic description showed TM distinct from its WT in more than 170 morphological parameters (Fig 3-1B, Table S6). To study the contribution of each gene deletion to the TM morphology, I examined the phenotypic effects of potential drug-hypersensitive background strains (Table S7). The study revealed that snq2 gene deletion in single, double and triple mutants background showed comparable number altered morphological profile (Fig. 3-1C), supporting the finding that deletion of SNQ2 in the pdr1Δpdr3Δ mutant background yielded a highly drug sensitive strain (Andrusiak, 2012). To find out which gene(s) is/are the principal contributor(s) to the TM background, I subjected the morphological data to PCA, a multivariate statistical approach. I found that taking all the dimensions into account, snq2 and pdr1 genes are the most dominant genes

(Fig. 3-1D), and Snq2 gene is the main contributor to the TM morphology based on the 2D phenotypic profile (Fig. 3-1E).

Because phenotypic characteristics such as defective growth could be scored to determine the sensitivity of cells to chemical compounds, at first, I pondered assessing drug sensitivity of hypersensitive yeast and WT cells after exposing both strains to a similar range of concentrations of standard compounds. Therein, a relative sensitivity was defined by taking the ratio of data determined from growth-inhibition test of triple mutants to that of its isogenic WT (Fig. 3-2A, see Material & methods for the details). Depending on the bioactive compounds, I found that TM yeast showed 2-15 fold higher sensitivity compared to the equivalent wild-type *S. cerevisiae* background strain used in previous image-based chemical genomics experiments in yeast. In addition, further comparison of morphological sensitivity after treating the cells with same concentration of TCM, ECB and HU revealed significant number of parameters altered in TM than WT (Fig. 3-2B). Altogether, the comparison provided evidence that yeast host is a sensitive and practical model system for our chemical phenomics studies.

Development of sensitive high-throughput phenotyping method

Previous works in our laboratory demonstrated that phenotypic similarity could be used for the prediction of drug targets (Ohnuki *et al.*, 2010; Okada *et al.*, 2014; Jin & Weisman, 2015), identification of target of a new antifungal drug (Iwaki *et al.*, 2013; Piotrowski *et al.*, 2015). However, for the comprehensive analyses of cellular responses even from reduced amount compound, I developed a more integrated profiling method that offers high-throughput sensitive screening capability (Fig. 3-3). In this approach, the genetic target(s) of a drug is explored by associating morphologic changes induced by chemical with that of the genetic perturbations. Target prediction pipeline from HTP-image acquired and processed data, could be accomplished the following three steps: Firstly, the distributions of each parameter value from about 2000 mutants were normalized using 726 replicates of WT sample distribution by generalized linear model (GLM) to evaluate the 501 parameters in each mutant, followed by characterization using principal component analysis (PCA). Secondly, morphological data from chemical compound treated set were similarly characterized by GLM and PCA. Finally, morphologic similarities were defined using

the Pearson product-moment correlation coefficient (R value). Using *p* values from the correlation coefficient test (at one-sided *p* value after the Bonferroni correction), mutants with significantly high positive R-values were defined as potential targets.

Phenotypic profiling of antimicrobial response signatures

As proof of mechanism, using well-characterized standard compounds, I needed to demonstrate the validity of an approach that allows the identification of those gene products that functionally interact with small molecules and result in the inhibition of cellular proliferation. For that purpose, I used six different standard compounds, which include both anticancer, and antifungals – hydroxyurea (HU), bortezomib (BTZ), benomyl (BML), methyl methanesulfonate (MMS), tunicamycin (TCM) and echinocandin B (ECB). The results from screening are described below.

Antifungal compounds. Since the quest for new effective antifungal agents is struggling to keep up with emerging drug resistance, using standard drugs, it is worth verifying the vitality of the new method in facilitating chemoprospecting of untapped natural compounds repository. I used three antifungal agents: ECB and TCM as representative of agents that damage the cell wall while BML as the antimitotic antifungal compound that inhibits microtubule polymerization and dynamics.

Benomyl

BML is an antifungal agent with fungicidal acidity that is selectively toxic to both microorganisms and invertebrates. The antimitotic antifungal compound inhibits microtubule polymerization and dynamics, thereby interfering with cell functions and intracellular transportation. A microtubule-depolymerizing agent was also shown to inhibit cancer cell proliferation at mitosis, by binding to a novel site in tubulin (Gupta *et al.*, 2004). Microtubules are comprised of α- and β-tubulin subunits encoded by *TUB1/TUB3* and *TUB2,* respectively. The essential *TUB1* and *TUB2* gene was not evaluated in this study because the both mutant was not included among the tested 1984 mutants. TUB2, the core of *S. cerevisiae* β-tubulin, was indicated to be a potential binding site for benomyl (Richards *et al.*, 2000). Morphological profiling revealed CIN4, a GTP-binding protein involved in beta-tubulin (Tub2p) folding, shared significant similarity with benomyl-treated cells (Fig. 3-4 & Fig. 3-5, Table 3-1). The GO term analyses with 20 most similar mutants showed 5 genes were

associated with GO process "tubulin assembly complex" (Table S8; GOID: 7021). This is consistent with a genetic screen which demonstrated CIN4 mutants display super-sensitivity to BML (Stearns *et al*., 1990).

Tunicamycin

TCM, a nucleoside antibiotic, is a specific inhibitor of *N*-linked glycosylation that blocks the first step of glycoprotein synthesis thereby inducing protein unfolding. The known target of tunicamycin is an essential gene *ALG7,* which encodes for UDP-*N*-acetyl-glucosamine-1-P transferase. The morphological profiles induced by the TCM treatment showed significant resemblance (165 out of 1984: 8.32%) to those induced by individual deletions of genes that encode mannosyltransferase (*HOC1, MNN10*, *OCH1*, *MNN2*, *etc.*) (Fig. 3-4 & Fig. 3-5, Table S8; $p < 0.0001$ after Bonferroni correction). The correlation coefficient for *hoc1*, and *mnn10* was 0.69 and 0.59, respectively. The Gene Ontology enrichment analysis with the significantly similar 165 gene deletion mutants ($p < 0.01$) showed 10 genes annotated to GO term "glycoprotein biosynthetic process," in a GO database (Table S8, GOID: 9101). These results are consistent with the mode of action of TCM, which blocks *N*-glycosylation (Ballou, 1990; Jigami, 2008).

Echinocandin B

ECB, a lipopeptide, is the first of the echinocandin class of antifungals which was known to inhibit Fks1p activity, the synthesis of 1,3-β-D-glucan, a major component of the yeast cell wall (Sawistowska-Schriider *et al.*, 1984). In my profiling; however, ECB-treated cells had no or little similarity to the FKS mutants (Fks2 and fks3). Instead, ECB-treated cells had somewhat similar profiles with TCM-treated cells *i.e.* mutants related to α-1,6-mannosyltransferase were enriched ($p < 0.00001$ after Bonferroni correction; Fig. 3-4 & Fig. 3-5, Table S8). This is consistent with previous observations and is probably due to functional redundancy between *Fks1* and *Fks2* and/or the multifunctional properties of *Fks1* (Ohnuki *et al.*, 2010; Okada *et al.*, 2010).

Anticancer compounds. Because of the extensive homology between yeast and human biochemical pathways and, in particular, that of the cell cycle, I tested the hypothesis that our chemical-genetic technique could reveal the mechanism of action

of anticancer compounds. Presented below is the profiles of some of such compounds in this study: HU, MMS, and BTZ.

Hydroxyurea

HU is an antineoplastic drug used in myeloproliferative disorders. The agent inhibits ribonucleotide reductase activity and consequent suppression of DNA synthesis (Chang & Cheng, 1978). In the yeast *S. cerevisiae*, HU targets RNR1 and RNR3, encode α-subunits (Elledge & Davis, 1990) though RNR2 (Elledge & Davis, 1987) and RNR4 (Wang *et al.*, 1997) encode β-subunit. To identify mutant cells with similar morphologic profiles, I applied the high-content image profiling on the phenotypic information of the mutants (Fig. 3-4 & Fig. 3-5). Of 1984 mutants, 770 (38.81%) morphologic profiles were significantly similar with that of the hydroxyurea-treated cells by the high-content image profiling at one-sided p <0.00001 with the Bonferroni correction. Among these mutants, 104 of them were annotated to a GO process term "DNA metabolism" in the GO database (Fig. 3-4 & Fig. 3-5; Table S8, GOID: 6259, $p < 0.01$). Although the *rnr4* mutant was not detected as a candidate as it wasn't included in our dataset, probably due weak phenotype, the mutant of the HU target *rnr3* was identified (R=0.30). Thus, this proves that the method proficiently identified genes from pathways related to the function of the agent.

Bortezomib

BTZ is an antitumor drug approved for the treatment of multiple myeloma, which acts either by inhibiting the activity of the 26S proteasome or through the inhibition of transcription factor nuclear factor-kappa beta (Richardson & Anderson, 2003). Our image profiling detected 466 (23.48%) of the 1984 genes including RPN10, non-ATPase base subunit of the 19S RP of the 26S proteasome (R=0.74), as potential bortezomib targets at one-sided $p < 0.00001$ with the Bonferroni correction. Besides, mutants such as RTT109, a gene required for H3K56 acetylation which plays a critical role in conferring resistance to replication stress, and *rpn4*, the transcription factor that stimulates expression of proteasome genes (R=0.68) were associated with "cellular response to DNA damage stimulus" (Table S8, GOID: 6974), a GO term that was significantly enriched (Fig. 3-4 & Fig. 3-5). Consistent with my finding research evidences indicated that proteasome inhibitors activate the DNA damage response or

perturb its pathway (Jacquemont & Taniguchi, 2007), which often equates to the enhanced chemosensitivity of cells to DNA damaging agents (Takeshita *et al.*, 2009). In a nutshell, this proves the power of our phenomic profiling in properly identifying genes in pathways related to the DNA damage signalling as targets for BTZ.

Methyl methanesulfonate (MMS)

MMS, an anticancer agent, which acts on DNA by methylating predominantly on N7-deoxyguanosine and N3-deoxyadenosine (Pegg, 1984). Brown and co-workers found a set of genes whose expression increased following methyl-methanesulfonate (MMS), which includes *RAD51*, *RAD54*, *RNR2*, *RNR4* or more (Gasch *et al.*, 2001; Chang *et al.*, 2002). Our image profiling system revealed that among the 1984 mutants, 563 (28.38%) were notably comparable to MMS-treated cells at one-sided $p<0.00001$ after Bonferroni correction (Fig. 3-4 & Fig. 3-5). Amongst the most likely candidates, 63 mutants including *Rad55 and MMS22* were associated with "cellular response to DNA damage stimulus" (Figure S8, GOID: 6974), which represented a significant GO enrichment ($p < 0.01$). This clearly indicates my method competently identified the genes encoding proteins in pathways related to DNA damage response.

3.3 DISCUSSION

To advance our understanding of disease biology, the characterization of the molecular target for clinically proven or new drugs is very important. In this study, I developed a novel image-based sensitive and high-throughput method to systematically identify genes encoding drug targets in yeast *S. cerevisiae.* The multimorphic profiling method uses quantitative morphologic response of antimicrobial compound from yeast cells and a dataset of ~2000 nonessential deletion mutants in drug-hypersensitive background. I used six well-characterized standard compounds that affect several cellular functions as a representative of antitumor and antifungal drugs. I attested that the proposed method could detect targets and uncover their potential mechanisms of action of drug candidate independent of prior information.

The technique is high-throughput would mean that large-scale screening of the chemical compound library can be done at a time. This will enable us to successfully recover targets for a large number of known compounds as well as make predictions

for several uncharacterized compounds. I also considered that our new yeast morphological database might serve as a powerful tool for linking novel low-abundance bioactive compounds to their biological targets and pathways. In a new yeast deletion, each strain was created in triple mutant background (*Δpdr1Δpdr3Δsnq2*) that compromises the cell's ability to pump out toxic compounds. Thus, a host strain carrying these mutations render cells more sensitive to bioactive compounds. As such it is expected to facilitate target identification through phenotypic response of any candidate compound at reduced amount. Moreover, the high-throughput profiling system will not only enable characterizing drug activity in yeast, but these analyses could also be extended in more relevant context in extensive chemical-biology program centered around mammalian cells. I propose that my new method could serve as a useful tool for high-throughput drug discovery.

Chemical genomic studies in yeast face dual challenges of determining compounds that induces complex phenotypes and inferring compounds' targets. My high-throughput phenomic profiling is a microscope-based chemical genomic study tool, which uses image-processing program CalMorph that outputs 501 cell morphology parameters (Ohtani *et al.*, 2004). Using this CalMorph system, our laboratory successfully identified genetic targets of both characterized bioactive compound from their morphologic signatures (Ohnuki *et al.*, 2010; Iwaki *et al.*, 2013; Gebre *et al.*, 2015). Chemical-genomic profiling, a similar approach to mine, also involves high-throughput screening a compound against a collection of mutant strains with defined genetic perturbations. Therein, the profiles of mutants that are differentially sensitive and show different morphology from this collection acts as a "fingerprint" for a compound's mode of action (Parsons *et al.*, 2004). Combining genetic interactions-based chemical genomics profiling and CalMorph-based phenomic profiling will facilitate the development of new paradigms for high-throughput drug discovery.

3.4 MATERIALS AND METHODS

Yeast Strains

To establish new morphological dataset for morphological profiling, I employed new yeast deletion mutant collection, where each strain carries three additional mutations (*pdr1Δ pdr3Δ snq2Δ*), covering over 5000 ORFs. These huge resources were obtained from the laboratory of Dr. Charles Boone at the University of Toronto. To

systematically identify yeast mutants and appropriate their growth under similar conditions, I took into consideration the research evidences noted previously (Warringer *et al.*, 2003; Ohya *et al.*, 2005). Since Ohya *et al.* (2005) demonstrated that individual deletion of nearly half of the nonessential genes in the genome (2,378 out of 4,718) affects cellular morphology; a list of 2,300 was extracted from a set of nearly 5000 quadruple mutants. By cluster analysis, groups of yeast mutants that have similar growth characters were identified using reference strains, mutant having relevant growth behavior available at PROPHECY database (Warringer *et al.*, 2003; http://prophecy.lundberg.gu.se).

Drug sensitivity of triple mutant host strain

Growth sensitivity. The evaluation of chemical sensitivity of TM host strain was identified from the dose-response analysis. Both yeast strains (WT and TM) were grown in YPD medium containing serially diluted antimicrobial agent in a 96-well microplate for about 42 h at 25 °C. Growth inhibition was determined from the doubling time of cells treated with each doses over mock-treated cells. After taking the ratio of relative growth delay in TM to its isogenic WT at each concentration of the standard compounds, the dose that has higher hit rate define the sensitivity of a given strain compared to the equivalent WT.

Morphological sensitivity. To assess the effects (*e.g.* the changes in the morphological parameters) brought about by the drug in hypersensitive yeast, both WT and sensitized yeast strains were treated with the same concentration of each standard drug. The number of altered parameters induced by the compounds in the WT and TM describes if the strain is sensitive than its WT cousin or not.

High-throughput image acquisition and analysis

Acquisition and analysis of image from high throughput samples was performed using an automated microscope In CELL analyzer as described previously (Okada *et al.*, 2015) with little modifications. Briefly, Wild-type yeast strains were cultured at 25 °C in YPD until the early log phase overnight on microtiter plate shaker. The cells were fixed with 3.7% formaldehyde (Wako Pure Chemical Industries) and 0.1 M potassium phosphate buffer (pH 6.5), agitated for 30 min at 25 °C in a water bath. Yeast cells were triply stained, image were acquired and subjected to CalMorph (ver.

1.2) analysis. To study the effect of gene deletion on the yeast morphology, image acquisition and analysis of single, double, triple mutant yeasts as well as their wild-type strain were carried out. Conditions of cell culture and image acquisition using AxioImager M1 microscope were described previously (Ohya *et al.*, 2005).

Phenotypic analysis of drug-hypersensitive strains

To find out what makes triple mutant strain different from its WT, the Manny-Whitney-Wilcoxon test was performed on PCA subjected quantitated morphological data using *wilcox.test()* function. Significantly changed morphological parameters were detected at the threshold *p* value of 0.01 or 0.05 after Boniferonni correction. Ultimately, morphological changes induced by the deletion of three pleotropic drug resistance genes in the hypersensitive background was summarized in the relevant cell cycle stages and depicted schematically.

To describe phenotypes of hypersensitive mutants taking all the dimensions into account, I applied PCA on the Z values of wild type 50 data. Next, I calculated the Z values of 7 yeast deletion mutants' and their parental wild-type morphological data (Table S2). To remove spurious correlation among morphological parameters, the Z values of mutants were projected onto the PCA-rotated 50 WT phenotypic data. After calculating the difference of all mutant data from mean value of wild type as a center, the association between two strains was estimated from correlation coefficient between the net values of resulting PC scores. For 2D phenotypic depiction, quantified raw morphological data was subjected to PCA without scaling and the first two PCs (PC1 and PC2) were plotted in 2D-phenotypic space.

Gene Ontology (GO) analysis

Information on GO annotations was gathered using the 'GO Term Finder', ver. 0.83 (http://www.yeastgenome.org/cgi-bin/GO/goTermFinder.pl) in the *Saccharomyces* Genome Database (Boyle *et al.* 2004). Genes of morphologically similar mutants were used as query genes, and 1980 of 1984 quadruple mutant associated with at least one GO term were considered as the background gene set.

3.5 FIGURES

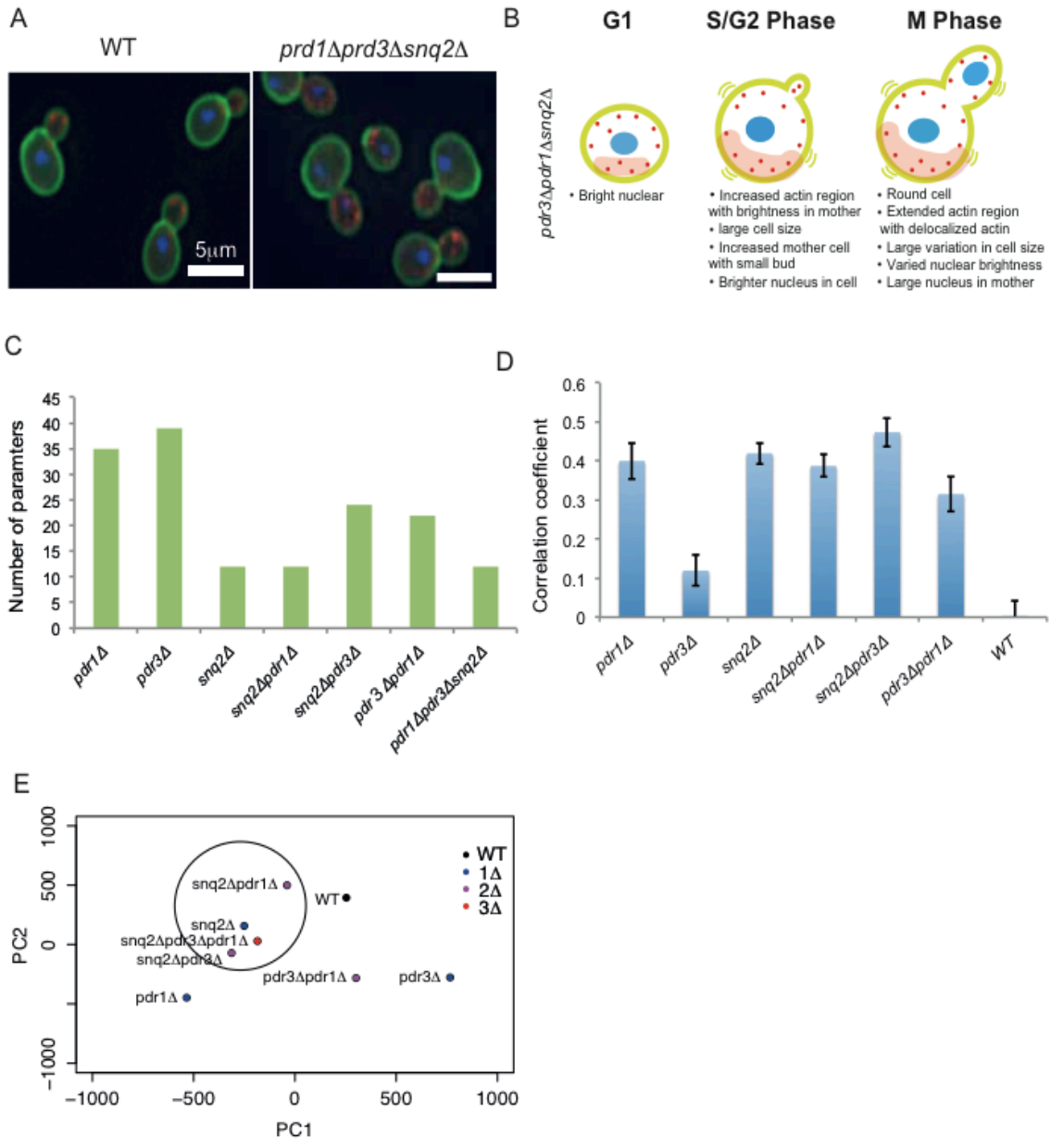

Figure 3-1. Morphological changes in *Δpdr1Δpdr3Δsnq2*.

(A) Microscopic observation of TM and WT cells. (B) Summary of morphological changes induced by three gene deletions. (C) Number of morphological parameters altered by deletion effect. (D) Then phenotypic characteristics of each mutant with respect to the triple mutant host strain was determined by a correlational analysis estimated after the data distribution is centered at the WT mean value. The result was depicted in column histogram expressed in terms of standard deviation. (E) The morphological data of the eight hypersensitive strains subjected to PCA and displayed in a 2D-phenotypic space.

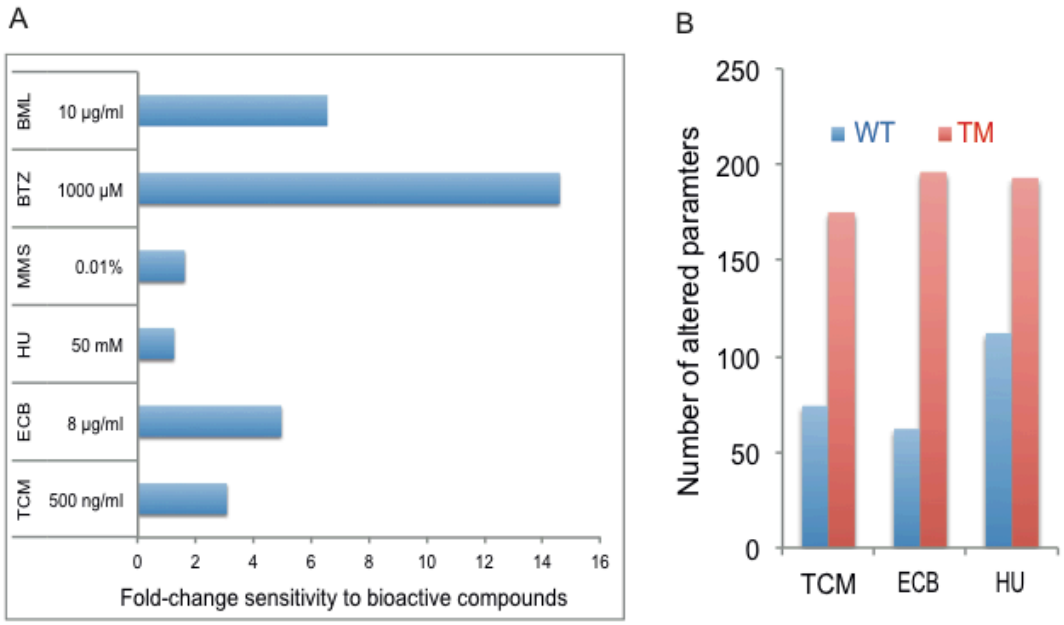

Figure 3-2. Drug sensitivity of *Δpdr1Δpdr3Δsnq2*.

Using the same concentration data for both WT and TM and growth sensitivity of triple mutants to 6 standard compounds (A) and the number of altered parameters by the compounds 100 ng/ml TCM, 2 µg/ml ECB, and 20 mM HU (B), respectively were determined by the Manny-Whitney-Wilcox test.

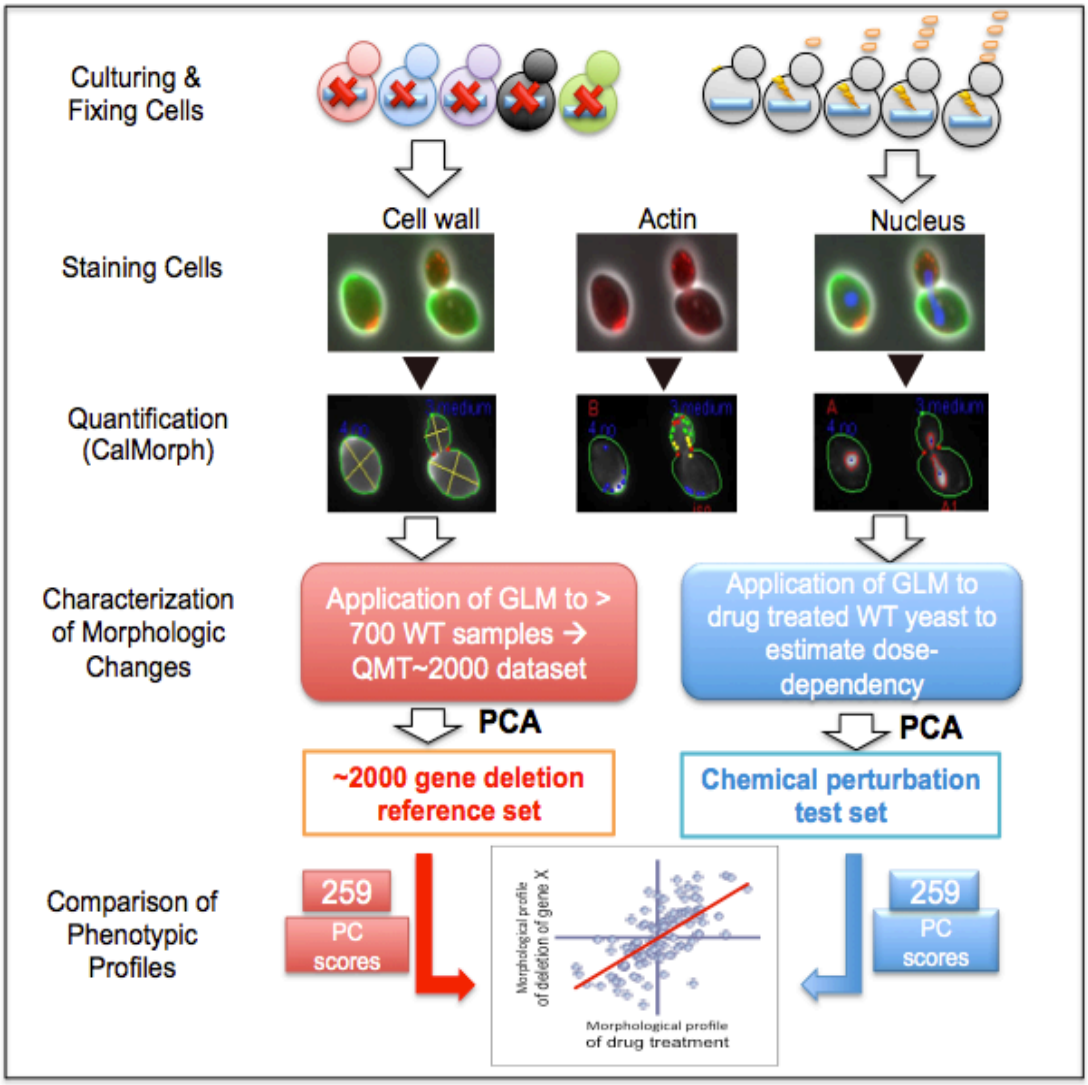

Figure 3-3. Schematic illustration of the integrated method used in this study.

Yeast cells (both mutants and drug-treated) were cultured, fixed with 37% formaldehyde, and stained triply with FITC (cell wall), Rhodamine-Ph (actin cytoskeleton), and DAPI (nuclear DNA), respectively. From the fluorescent microscopic images of triple-stained yeast cells, CalMorph analyzes and quantitates 501 cell morphology parameters. To characterize the mutants, first the distributions of 726 TM host strain, considered as a "wild-type (WT)", values for each parameter were transformed. Using more than 700 WT samples, the distributions of parameter values for the 2000 quadruple mutants (QMT) were normalized and subjected to PCA. This serves as gene perturbation reference set. Next, the distributions of the parameter values from drug-treated wild-type yeast were characterized and then defined by the PCA of wild-type data transformed for 259 parameters. The output will be used as chemical perturbation test data set. Finally, the Pearson product-moment correlation coefficient (R) defined the morphologic similarities between the dose-dependent changes induced drug treatment and those induced by the deletion mutations.

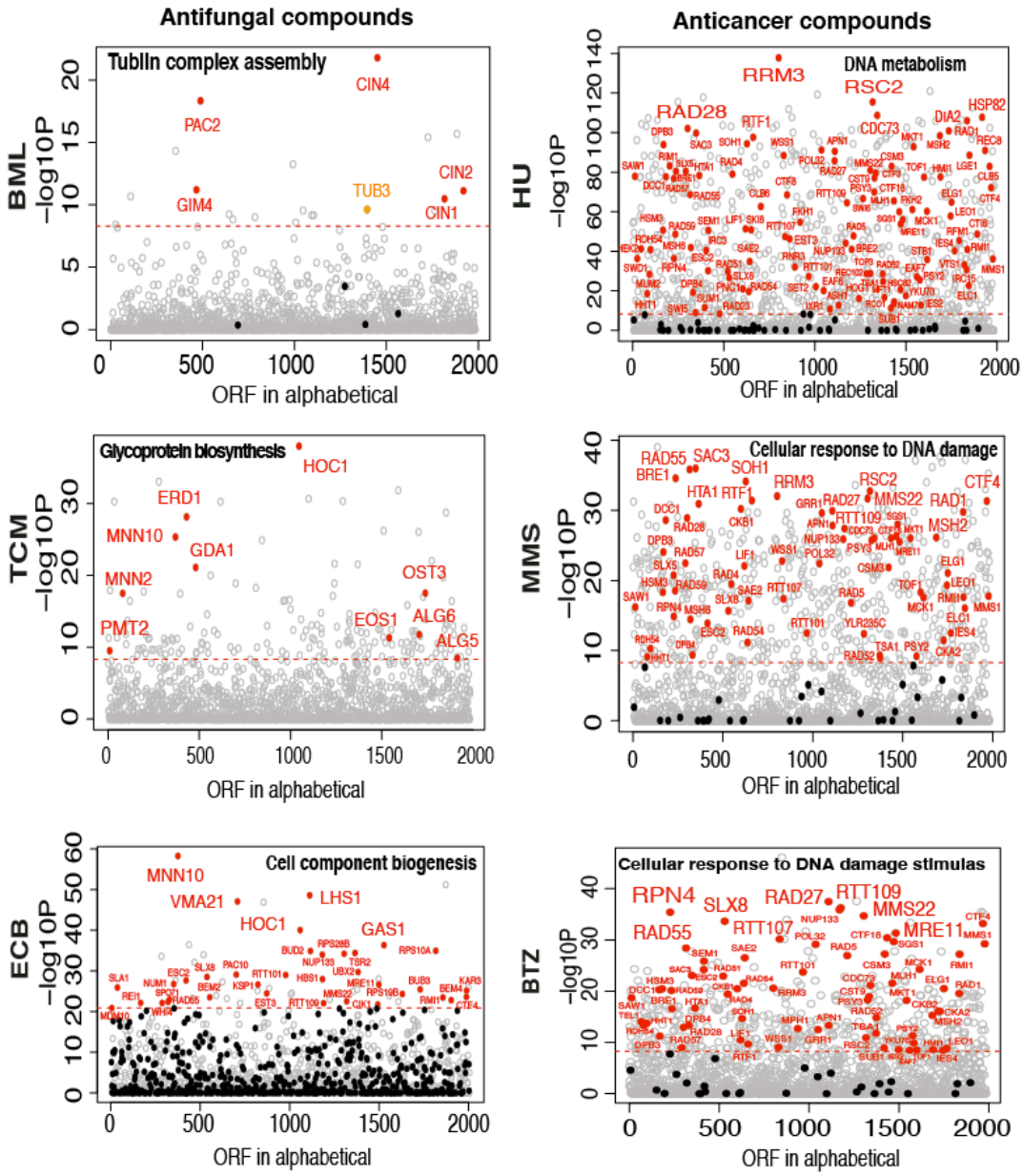

Figure 3-4. Prediction of 6 target-known compounds.

Morphological profiling was performed using integrated method for sensitized yeast cells treated with BML, TCM, ECB, HU, MMS, and BTZ. Comparison of profiles of drug-treated cell morphology with non-essential genes deletion in the hypersensive background revealed cellar target of each drug and genes involved in functionally related pathways. Red filled circles are genes that share significant similarity with those related to the GO terms “tubulin complex assembly,” or “glycoprotein synthesis,” or “cell component biogenesis,” or “DNA metabolism,” or “cellular response to DNA damage,” or “cellular response to DNA damage stimulus.” Black filled circles show genes that show insignificant similarity with each drug treated cells.

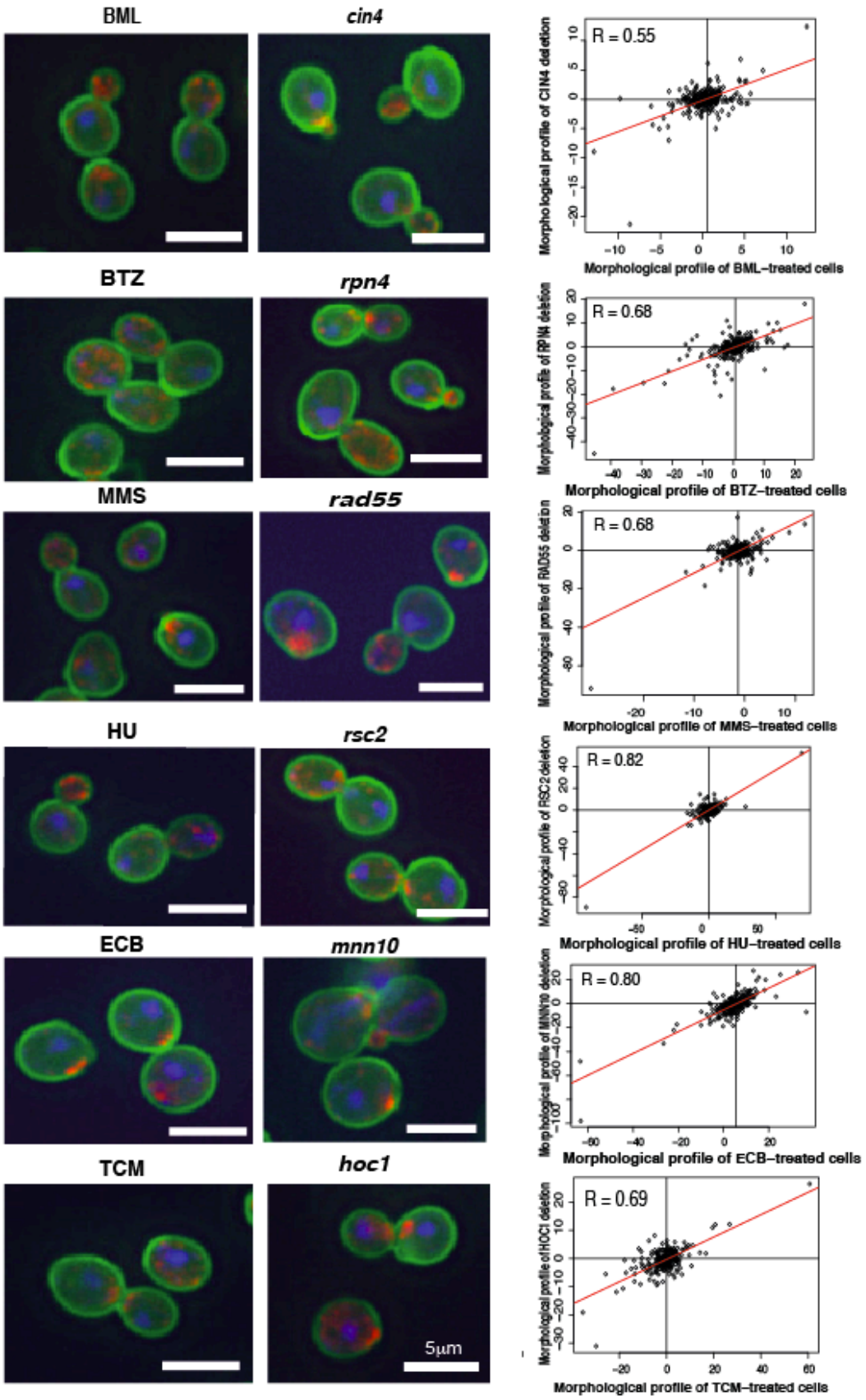

Figure 3-5. Morphological similarity of yeast treated with standard compounds.

Morphology of cells treated with the six standard compounds was compared to mutant that shared significantly similarity. The degree of morphological resemblance was expressed as a Pearson product moment correlation coefficient, R values for each drug, which is indicated on the right side of respective images.

3.6 TABLES

Table 3-1 Yeast mutants that shared significant similarity with benomyl treated hypersensitive host strain

Drug	ORF	GENE	DESCRIPTION	R	p
BML	YMR138W	CIN4	GTP-binding protein involved in beta-tubulin (Tub2p) folding; isolated as mutant with increased chromosome loss and sensitivity to benomyl	0.55	1.66E-22
	YER007W	PAC2	Microtubule effector required for tubulin heterodimer formation; binds alpha-tubulin, required for normal microtubule function, null mutant exhibits sensitivity to benomyl	0.51	4.69E-19
	YPL165C	SET6	SET domain protein of unknown function; deletion heterozygote is sensitive to compounds that target ergosterol biosynthesis, may be involved in compound availability	0.47	2.08E-16
	YOR058C	ASE1	Mitotic spindle midzone-localized microtubule bundling protein; undergoes cell cycle-regulated degradation by anaphase promoting complex; potential Cdc28p substrate	0.47	3.93E-16
	YDR183W	PLP1	Protein that interacts with CCT (chaperonin containing TCP-1) complex; has a role in actin and tubulin folding; has weak similarity to phosducins, which are G-protein regulators	0.45	4.82E-15
	YJL145W	SFH5	Non-classical phosphatidylinositol transfer protein (PITP); localizes to the peripheral endoplasmic reticulum, cytosol and microsomes; similar to Sec14p; partially relocalizes to the plasma membrane upon DNA replication stress	0.44	5.72E-14
	YEL003W	GIM4	Subunit of the heterohexameric cochaperone prefoldin complex; complex binds specifically to cytosolic chaperonin and transfers target proteins to it	0.40	6.33E-12
	YPL241C	CIN2	GTPase-activating protein (GAP) for Cin4p; tubulin folding factor C involved in beta-tubulin (Tub2p) folding; mutants display increased chromosome loss and benomyl sensitivity	0.40	7.57E-12
	YBR101C	FES1	Hsp70 (Ssa1p) nucleotide exchange factor; required for the release of misfolded proteins from the Hsp70 system to the Ub-proteasome machinery for destruction; cytosolic homolog of Sil1p	0.39	2.12E-11
	YOR349W	CIN1	Tubulin folding factor D involved in beta-tubulin (Tub2p) folding; isolated as mutant with increased chromosome loss and sensitivity to benomyl	0.39	3.33E-11
	YML124C	TUB3	Alpha-tubulin; associates with beta-tubulin (Tub2p) to form tubulin dimer, which polymerizes to form microtubules; expressed at lower level than Tub1p; TUB3 has a paralog, TUB1	0.37	2.38E-10

Table 3-2. Yeast mutants that shared significant similarity with tunicamycin treated hypersensitive host strain

Drug	ORF	GENE	DESCRIPTION	R	p
TCM	YJR075W	HOC1	Alpha-1,6-mannosyltransferase; involved in cell wall mannan biosynthesis; subunit of a Golgi-localized complex that also contains Anp1p, Mnn9p, Mnn11p, and Mnn10p	0.69	1.06E-38
	YDL192W	ARF1	ADP-ribosylation factor; GTPase of the Ras superfamily involved in regulation of coated vesicle formation in intracellular trafficking within the Golgi	0.65	9.37E-34
	YNL238W	KEX2	Kexin, a subtilisin-like protease (proprotein convertase); a calcium-dependent serine protease involved in the activation of proproteins of the secretory pathway	0.64	1.53E-32
	YKL073W	LHS1	Molecular chaperone of the endoplasmic reticulum lumen; involved in polypeptide translocation and folding; regulated by the unfolded protein response pathway	0.64	2.29E-31
	YLR242C	ARV1	May function in transport of glycosylphosphatidylinositol intermediates into ER lumen; required for normal intracellular sterol distribution; human ARV1 is required for normal cholesterol and bile acid homeostasis, can complement yeast arv1 null mutant	0.64	4.92E-31
	YBL007C	SLA1	Cytoskeletal protein binding protein; required for assembly of the cortical actin cytoskeleton; interacts with proteins regulating actin dynamics and proteins required for endocytosis; found in the nucleus and cell cortex; has 3 SH3 domains	0.64	5.66E-31
	YGL084C	GUP1	Plasma membrane protein involved in remodeling GPI anchors; role in misfolded protein quality control; proposed to be involved in glycerol transport	0.64	5.79E-31
	YPL069C	BTS1	Geranylgeranyl diphosphate synthase (GGPS); increases the intracellular pool of geranylgeranyl diphosphate	0.62	1.86E-29
	YDR414C	ERD1	Predicted membrane protein required for lumenal ER protein retention; mutants secrete the endogenous ER protein, BiP (Kar2p)	0.61	7.38E-29
	YMR307W	GAS1	Beta-1,3-glucanosyltransferase; required for cell wall assembly localizes to cell surface via a GPI anchor	0.59	6.35E-27

Table 3-3. Yeast mutants that shared significant similarity with echinocandin B treated hypersensitive host strain

Drug	ORF	GENE	DESCRIPTION	R	p
ECB	YDR245W	MNN10	Subunit of a Golgi mannosyltransferase complex; complex mediates elongation of the polysaccharide mannan backbone; membrane protein of the mannosyltransferase family	0.79	5.26E-59
	YPL069C	BTS1	Geranylgeranyl diphosphate synthase (GGPS); increases the intracellular pool of geranylgeranyl diphosphate	0.76	5.85E-52
	YKL073W	LHS1	Molecular chaperone of the endoplasmic reticulum lumen; involved in polypeptide translocation and folding; nucleotide exchange factor for the ER lumenal Hsp70 chaperone Kar2p; regulated by the unfolded protein response pathway	0.75	2.49E-49
	YGR105W	VMA21	Integral membrane protein required for V-ATPase function; localized to the yeast endoplasmic reticulum (ER)	0.74	8.03E-48
	YHR178W	STB5	Transcription factor; involved in regulating multidrug resistance and oxidative stress response; forms a heterodimer with Pdr1p; contains a Zn(II)2Cys6 zinc finger domain that interacts with a pleiotropic drug resistance element in vitro	0.74	1.25E-47
	YJR075W	HOC1	Alpha-1,6-mannosyltransferase; involved in cell wall mannan biosynthesis	0.70	9.31E-41
	YDR414C	ERD1	Predicted membrane protein required for lumenal ER protein retention; mutants secrete the endogenous ER protein, BiP (Kar2p)	0.68	3.65E-37
	YMR307W	GAS1	Beta-1,3-glucanosyltransferase; required for cell wall assembly and also has a role in transcriptional silencing	0.68	4.47E-37
	YOR293W	RPS10A	Protein component of the small (40S) ribosomal subunit; homologous to mammalian ribosomal protein S10	0.67	1.09E-35
	YKL092C	BUD2	GTPase activating factor for Rsr1p/Bud1p; mutants exhibit random budding in all cell types	0.67	1.28E-35

Table 3-4. Yeast mutants that shared significant similarity with hydroxyurea treated hypersensitive host strain

Drug	ORF	GENE	DESCRIPTION	R	p
HU	YHR031C	RRM3	DNA helicase involved in rDNA replication and Ty1 transposition; binds to and suppresses DNA damage at G4 motifs in vivo; relieves replication fork pauses at telomeric regions	0.86	1.59E-138
	YNR010W	CSE2	Subunit of the RNA polymerase II mediator complex; associates with core polymerase subunits to form the RNA polymerase II holoenzyme	0.83	9.92E-122
	YJL188C	BUD19	Dubious open reading frame; unlikely to encode a functional protein	0.83	5.82E-120
	YDR287W	INM2	Inositol monophosphatase; involved in biosynthesis of inositol; enzymatic activity requires magnesium ions and is inhibited by lithium and sodium ions; inm1 inm2 double mutant lacks inositol auxotrophy	0.83	1.74E-118
	YDL113C	ATG20	Required for the cytoplasm-to-vacuole targeting (Cvt) pathway and for endosomal sorting; has a Phox homology domain that binds phosphatidylinositol-3-phosphate; interacts with Snx4p	0.82	2.64E-116
	YLR357W	RSC2	Component of the RSC chromatin remodeling complex; required for expression of mid-late sporulation-specific genes; involved in telomere maintenance	0.82	3.28E-116
	YPL090C	RPS6A	Protein component of the small (40S) ribosomal subunit; homologous to mammalian ribosomal protein S6	0.82	2.8E-113
	YHR210C	YHR210C	Putative aldose 1-epimerase superfamily protein; non-essential gene	0.82	1.47E-112
	YLR418C	CDC73	Component of the Paf1p complex; binds to and modulates the activity of RNA polymerases I and II; required for expression of certain genes, modification of some histones, and telomere maintenance	0.81	1.9E-109
	YPL240C	HSP82	Hsp90 chaperone; redundant in function with Hsc82p; required for pheromone signaling, negative regulation of Hsf1p; promotes telomerase DNA binding, nucleotide addition; protein abundance increases in response to DNA replication stress	0.81	1.76E-108

Table 3-5. Yeast mutants that shared significant similarity with methyl methanesulfonate treated hypersensitive host strain

Drug	ORF	GENE	DESCRIPTION	R	p
MMS	YOR080W	DIA2	Required for deactivation of Rad53 checkpoint kinase, completion of DNA replication during recovery from DNA damage, assembly of RSC complex, RSC-mediated transcription regulation, and nucleosome positioning	0.70	8.79E-40
	YBR194W	AIM4	Protein proposed to be associated with the nuclear pore complex; null mutant is viable, displays elevated frequency of mitochondrial genome loss	0.70	9.78E-40
	YOR014W	RTS1	B-type regulatory subunit of protein phosphatase 2A (PP2A); required for maintenance of septin ring organization during cytokinesis, for ring disassembly in G1 and for dephosphorylation of septin, Shs1p	0.69	2.36E-38
	YPL055C	LGE1	Protein of unknown function; null mutant forms abnormally large cells, and homozygous diploid null mutant displays delayed premeiotic DNA synthesis and reduced efficiency of meiotic nuclear division	0.69	5.91E-38
	YOR038C	HIR2	Subunit of HIR nucleosome assembly complex; involved in regulation of histone gene transcription; recruits Swi-Snf complexes to histone gene promoters; promotes heterochromatic gene silencing with Asf1p	0.69	1.33E-37
	YOL012C	HTZ1	Histone variant H2AZ; exchanged for histone H2A in nucleosomes by the SWR1 complex; involved in transcriptional regulation through prevention of the spread of silent heterochromatin	0.68	6.66E-37
	YDR159W	SAC3	mRNA export factor; required for biogenesis of the small ribosomal subunit; component of TREX-2 complex (Sac3p-Thp1p-Sus1p-Cdc31p) involved in transcription elongation and mRNA export from the nucleus	0.68	1.01E-36
	YDR076W	RAD55	Protein that stimulates strand exchange; stimulates strand exchange by stabilizing the binding of Rad51p to single-stranded DNA; involved in the recombinational repair of double-strand breaks in DNA during vegetative growth and meiosis	0.68	1.46E-36
	YPR160W	GPH1	Glycogen phosphorylase required for the mobilization of glycogen; non-essential; regulated by cyclic AMP-mediated phosphorylation; expression is regulated by stress-response elements and by the HOG MAP kinase pathway	0.67	6.16E-36

Table 3-6. Yeast mutants that shared significant similarity with botezomib treated hypersensitive host strain

Drug	ORF	GENE	DESCRIPTION	R	p
BTZ	YHR200W	RPN10	Non-ATPase base subunit of the 19S RP of the 26S proteasome; N-terminus plays a role in maintaining the structural integrity of the regulatory particle (RP); binds selectively to polyubiquitin chains; homolog of the mammalian S5a protein	0.74	7.74E-47
	YLR182W	SWI6	Transcription cofactor; forms complexes with Swi4p and Mbp1p to regulate transcription at the G1//S transition; involved in meiotic gene expression	0.69	2.69E-38
	YKL113C	RAD27	5' to 3' exonuclease; required for Okazaki fragment processing and maturation, for long-patch base-excision repair & large loop repair, ribonucleotide excision repair	0.69	3.3E-38
	YLL002W	RTT109	Histone acetyltransferase; critical for cell survival in presence of DNA damage during S phase; acetylates H3K56, H3K9; buffering of mRNA synthesis rate against changes in gene dosage during S phase	0.68	5.54E-37
	YKR082W	NUP133	Subunit of Nup84p subcomplex of nuclear pore complex (NPC); contributes to nucleocytoplasmic transport, NPC biogenesis; is involved in establishment of a normal nucleocytoplasmic concentration gradient of GTPase Gsp1p	0.68	1.33E-36
	YPR120C	CLB5	B-type cyclin involved in DNA replication during S phase; activates Cdc28p to promote initiation of DNA synthesis; most abundant during late G1 phase	0.67	3.61E-36
	YDL020C	RPN4	Transcription factor that stimulates expression of proteasome genes; Rpn4p levels are in turn regulated by the 26S proteasome in a negative feedback control mechanism; RPN4 is transcriptionally regulated by various stress responses; relative distribution to the nucleus increases upon DNA replication stress	0.67	3.83E-36
	YPR141C	KAR3	Functions in mitosis and meiosis, localizes to the spindle pole body depend on functional Cik1p, required for nuclear fusion during mating; potential Cdc28p substrate	0.67	7.09E-36
	YLR320W	MMS22	Subunit of E3 ubiquitin ligase complex involved in replication repair; stabilizes protein components of the replication fork, and promoting efficient recovery during replication stress	0.67	1.98E-35
	YIL040W	APQ12	Nuclear envelope/ER integral membrane protein; interacts and functions with Brr6p and Brl1p in lipid homeostasis	0.66	1.18E-34

Table 3-7. Representative enriched GO processes associated with genes affected in sensitized yeast treated with antimicrobial compounds

Drug	GOID	GO term	P-value	Genes annotated to the term
BML	7021	Tubulin complex assembly	1.22E-06	GIM4, PAC2, CIN4, CIN1, CIN2
TCM	9101	Glycoprotein biosynthetic process	0.00635	PMT2, MNN2, MNN10, ERD1, GDA1, HOC1, EOS1, ALG6, OST3, ALG5, MDM10, SLA1
ECB	71840	Cellular component organization or biogenesis	0.00287	REI1, WHI4, RAD55, SPO71, NUM1, MNN10, ESC2, SLX8, BEM2, XRN1, PAC10, VMA21 KSP1, EST3, APQ12, RTT101, HOC1, LHS1, BUD2, NUP133, HBS1, RTT109, RPS28B, KAR3 MMS22, TSR2, UBX2, CIK1, MRE11, GAS1, RPS19B, BUB3, RPS10A, RMI1, BEM4, CTF4,
HU	6259	DNA metabolic process	2.85E-09	SAW1, SWD1, HEK2, HHT1, MUM2, RDH54, HSM3, DPB3, DCC1, RIM1, SLX5, RPN4, RAD59, BRE1, RAD57, RAD28, RAD55, MSH6, DPB4, SWI5, SAC3, HTA1, SUM1, IRC3, ESC2, SEM1, RAD51, SLX8, RAD4, PNC1, LIF1, SOH1, RAD54, SAE2, SKI8, RTF1, CLB6, RRM3, WSS1, RTT107, CTF8, EST3, FKH1, RTT101, SET2, POL32, EAF6, IXR1, RAD27, APN1, ASH1, NUP133, RTT109, BRE2, RAD5, HOG1, SWI6, TOP3, MMS22, REC102, RSC2, PSY3, CTF3, CST9, CDC73, TSA1, RAD52, MFT1, SUB1, CSM3, RCO1, CTF18, NAM7, MLH1, HSC82, SGS1, MRE11, YKU70, FKH2, EAF7, PSY2, TOF1, MCK1, STB1, MSH2, HMI1, DIA2, LEO1, ELG1, IES4, RFM1, VTS1, IRC15, RAD1, RMI1, ELC1, LGE1, CTI6, HSP82, REC8, CLB5, CTF4, MMS1
MMS	6974	Cellular response to DNA damage stimulus	8.78E-10	SAW1, HHT1, RDH54, HSM3, DPB3, DCC1, SLX5, RPN4, RAD59, BRE1, RAD57, RAD28, RAD55, MSH6, DPB4, SAC3, HTA1, ESC2, SLX8, RAD4, CKB1, LIF1, SOH1, RAD54, SAE2, RTF1, RRM3, WSS1, RTT107, RTT101, POL32, GRR1, RAD27, APN1, NUP133, RTT109, RAD5, YLR235C, MMS22, RSC2, PSY3, CDC73, TSA1, RAD52, CSM3, CTF18, MLH1, SGS1, MRE11, MKT1, PSY2, TOF1, MCK1, MSH2, CKA2, LEO1, ELG1, IES4, RAD1, RMI1, ELC1, CTF4, MMS1
BTZ	6974	Cellular response to DNA damage stimulus	1.28E-16	SAW1, TEL1, HHT1, RDH54, HSM3, DPB3, DCC1, RPN4, RAD59, BRE1, RAD57, RAD28, RAD55, DPB4, SAC3, HTA1, ESC2, SLX8, RAD4, CKB1, LIF1, SOH1, RAD54, SAE2, RTF1, RRM3, WSS1, RTT107, MPH1, RTT101, POL32, GRR1, RAD27, APN1, NUP133, RTT109, RAD5, YLR235C, MMS22, RSC2, PSY3, CDC73, TSA1, RAD52, SUB1, CSM3, CTF18, MLH1, SGS1, MRE11, YKU70, MKT1, EAF7, PSY2, TOF1, MCK1, MSH2, CKB2, CKA2, LEO1, ELG1, IES4, RAD1, RMI1, CTF4, MMS1

GENERAL DISCUSSION

The overview of the development of antimicrobial therapeutic agents reflects increased interest in this particular area of infectious diseases. It is therefore necessity to put concerted efforts in developing more promising and effective antimicrobials for use in the clinical arena. Although still in the investigational stages, recent advances in the development of new antifungals and/or antibiotics offer some new hope of improving the future of antimicrobial therapy. While hitting the target is the basic challenge in phenotype-driven drug discovery, advances in computational and biochemical approaches are providing a powerful toolbox with complementary technologies for target identification.

In this study, I developed two quantitative morphology-based methods to predict cellular targets of an antifungal agent using phenotypes of yeast cells responding to extracellular chemical stimuli. At first, I profiled currently available antifungal drugs using yeast morphology to gain further insights into antifungal drug profiles, and propose new methods of predicting drug targets without any mutant information. I analyzed echinocandins, an azole, an allylamine, a morpholine, and a fluorinated pyrimidine analog. Comparison with deletion mutants of each of 4,718 non-essential genes confirmed the MoA of the drugs and revealed unexpected connections among the various cellular processes. I then proposed that development of supervised classifier based on the morphological profiles of the drugs could facilitate elucidating the mode of action of a newly discovered compound as it sorts into drugs with similar MoA. Intriguingly, all the (target-known) compounds in test set were exclusively classified into expected antifungal class according to their MoA. To this end, I suggest that morphological profiling can be used to develop novel antifungal drugs.

In addition to this, the systematic classifier also drew new insights into antifungal agents. For example, miconazole was assigned to ergosterol biosynthesis inhibitors, but plotted near DNA affecting agents' class. Recent mechanistic studies (Najm *et al.*, 2015) showed that miconazole affects pathways regulating DNA synthesis via interfering the role of mitogen-activated protein kinase/extracellular signal-regulated

kinase signaling in estrogen receptor positive MCF-7 breast carcinoma cells. This suggests the power of the method in efficiently indicating drugs MoA from their morphologic signatures. Though I expected CMA to be classified into cell wall synthesis inhibitors, considering its MoA, it was notably ascribed to a different drug group - nucleic acid inhibitors. To my surprise, a very recent research evidences demonstrated an unexpected finding that the yeast vacuole plays a positive essential role in initiation of the cell cycle and its functional loss results in a specific arrest of cells in G1 phase (Jin & Weisman, 2015). Taken together, these data indicate that high-content system was successful in profiling phenotype by drug function.

Aiming at enhancing the contribution of natural products (NPs) and rare compound to the modern drug development, I sought to address the drawbacks of the existing analytical method that utilizes relatively high amount drugs. To establish yeast morphology-based chemical genomics as a powerful approach for characterizing low-abundance NPs, this thesis introduced two major faucets. First, I sought to modify the current morphological profiling strategy so as to reduce the quantity of each compound required for analysis. To that purpose our laboratory introduced new yeast gene deletion collections that were generated in the hypersensitive background; strains compromised for their ability to efflux chemical compounds. Second, I endeavored to combine those compound-efficient new yeast deletion collections with high-content high-speed automated microscopy to maximize the efficiency of high throughput screening. Therein, dose-dependent morphological phenotypes of the drug-hypersensitive strain were compared with the new panel of morphological data composed of ~2,000 representative mutant strains. Finally, I needed to demonstrate the applicability of the new integrated approach by profile six previously characterized compounds, for which it successfully established the targets and functionally related genes. In my opinion, it would be great if the use of these different phenotypic drug discovery approaches could be combined so as to leverage the scale of our study (Fig. 0-3).

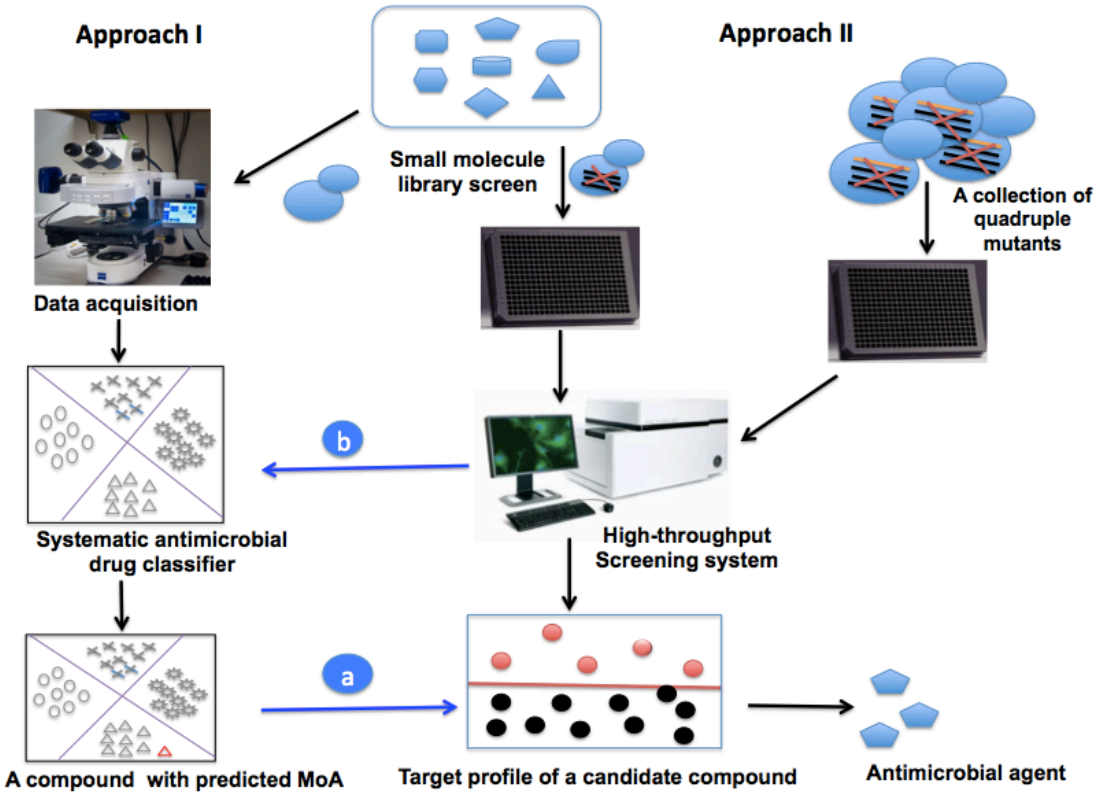

Figure 0-3. Conceptual framework for integrating antimicrobial drug development paradigms in this study.

The proposed model platform envisages integration of the two independently developed methods in this study in order to leverage the morphology-based chemical phenomics. First, compound library will be screened to find out reagents with bioactivity in yeast cells, followed by acquisition and processing of morphological data and subsequent phenotypic analysis of selected compounds using LDA approach indicates the mode of action of each compound. Next, specific target gene for those bioactive compounds for which mode of action is identified could be predicted using new integrated method (refer to blue line designated with symbol "b"). Similarly, quantitative morphological data obtained from small amount of bioactive compounds treated hypersensitive strains will then be compared with the HTP morphological information of quadruple mutants so as to predict their cellular targets. Alternatively, the mode of action of the drugs might be described using a machine learning approach established previously (see the blue line represented with symbol "a"). After appropriate validation of the predicted targets with relevant genetic, biochemical or molecular methods, promising candidate is ready for required next stage study. Red marked "Δ" symbol in LDA space is predicted MoA of a drug while red filled circles in profiling plot indicates targets of a compound from my morphological similarity search system.

PERSPECTIVES

In seek of new directions in antimicrobial drug research and development, researchers across many scientific domains have responded to the increasing lack of effective drugs by inventing new effective and safe antimicrobial agents. Correspondingly, investigators responded to the challenges from the threats posed by increasing drug-resistant pathogenic strains by studying the feasibility of combinatorial therapy as combination drugs are less prone to drug resistance. Therein, it was demonstrated that reinforcing the computational prediction science in the discovery of synergistic drug combinations based upon known combinations and advancements of fungal chemical genomics prospects a new direction in antimicrobial drug discovery and therapy (Chen *et al.*, 2007; Jansen *et al.*, 2009). Alternatively, to overcome the phenomenon of multidrug resistance, researchers engage themselves in finding new clinically useful potential compound from various sources. Integration of computational approaches into a drug development process was indicated helpful in providing a powerful toolbox for target identification, discovery and optimization of drug candidate molecules (Katsila *et al.*, 2016). As part and parcel of this concerted effort, the findings of my study shall be considered for their prospective application to substantiate the antimicrobial drug discovery pipeline.

The application of the chemical genomic approaches offers capacity for describing the global cellular response to a certain compound, for predicting the target of a compound, and for inferring the function of genes. One of chemogenomic approach comparable to our morphological profiling system is homozygous profiling or haploid deletion chemical-genetic profiling (Parsons *et al.*, 2004, 2006; Lee *et al.*, 2005; Hillenmeyer *et al.*, 2008). HOP, an assay in which relative growth rate *e.g.* in the presence of drug, is measured by microarray signal intensity in the strains that are completely deleted for non-essential genes in either haploid or diploid strains. By screening a collection of compounds across non-essential genes in this assay, each compound produces a unique chemogenomic signature. When these genome-wide profiles are compared to those obtained from drugs with well-characterized mechanisms, clustering of the signatures allow a researcher to infer the mechanism of action (Parsons *et al.*, 2004, 2006). At current stage, our target prediction procedure is possible by comparing the phenotypic (501 dimensional interaction) profiles wild-

type cells treated with compound against morphological data of deletion mutants. To take this phenotypic drug discovery approach to the next stage, it would be great if the laboratory of signal transduction ponders drug target profiling using morphological analysis of mutant cells treated with compound, which offers quite significant advantage (501 x n dimensional interaction profile) over its fitness assay where mutant cells treated with compound would generate n dimensional profile only.

Moreover, it has also been established that similarity between fitness or morphological profiles indicates a similarity in the mode of action of the corresponding compounds (Parsons *et al.*, 2006; Ohnuki *et al.*, 2010; Gebre *et al.*, 2015). The capability of chemical genomic profiles to estimate similarities in the mode of action, gene function and cellular response dare one to ask whether they can also be used to predict synergy. Such concept of using chemogenomic approaches for synergy prediction was attempted by Jansen and his colleagues (Jansen *et al.*, 2009). This suggests that relevant bioinformatics-driven approaches could be geared to efficiently predict compound synergy for their combinatorial therapies thereby eluding the failures of costly developed drugs due to either inherent or acquired resistance. By the same token, my systematic drug classifier could be considered as one of the new complementary methods to predict compound synergy. Therein, the approach shall use morphological profiles in order to identify compound profiles that have a statistically significant degree of similarity to a standard drug (*e.g.* fluconazole, or flucytosine or echinocandins) profile. The compounds identified will be then experimentally verified to be synergistic with standard compounds and with each other, in both *S. cerevisiae* and/or the fungal pathogen *Candida albicans*.

Furthermore, miniaturization is the concept fundamental to enhancing the state-of-the-art in high-content, high throughput drug screening, so as to facilitate dramatic cost savings through reduced usage of expensive biochemical reagents and to enable large-scale screening on primary cells. Natural products are selected for precise biological functions in nature and are therefore a rich source of specific small molecule inhibitors. In spite of these characteristics and their overwhelmingly favorable success, the use natural-based compounds by many pharmaceutical companies have declined of based on their incomparability with high-throughput screening approaches (Harvey, 2008). This is largely because natural products are

often difficult and expensive to obtain and are therefore available in very limited quantities. Moreover, from an industry perspective, drug development platforms for rare ("orphan") and/or neglected diseases are less interesting due to the low revenue on investment. In my study, I presented the adoption of an integrated approach to profile potentially useful anticancer and antifungal compounds, and I hope that this strategy will help to move forward the field of drug development for orphan and/or neglected diseases as well as from scarce natural products.

APPENDICES

SUPPLEMENTAL RESULTS AND DISCUSSION

Cellular effects of nystatin

The other test compound included for the comprehensive study of antifungal agents was the polyenes; e.g., nystatin. Nystatin, an ionophore ergosterol-targeting polyene agent, is known to bind to membrane ergosterol and increase the permeability of the fungal cell membrane, accelerating leakage of intracellular contents (Lampen *et al.*, 1962; Zygmunt & Tavormina, 1966; Hammond, 1977; Akaike & Hirata, 1994). For this reason, we expected that its effect might be so immediate that there may be insufficient time to observe changes in cell morphology. As expected, agent-treated cells were found to be dead without any significant effect on cellular morphology (Fig. S1A). In addition, the growth rates at dose-dependent agent concentrations revealed that cell growth was the extension of a lag phase without any significant alteration of doubling time (Fig. S1 B & C), suggesting its primary effect is killing, but the survived cells continued to proliferate independent of the presence of bioactive agent. As a result, we culled the data of this drug from processing for further study.

SUPPLEMENTAL EXPERIMENTAL PROCEDURE

Cell viability test

Owing to its mode of action, we assessed the effect on cell viability before evaluating the cellular responses to the polyene agent, nystatin. For this purpose, wild-type cells were cultured in YPD at 25°C overnight. Logarithmically growing cells were treated with or without 100 μg mL^{-1} nystatin for 1 h, and then collected by centrifugation and mixed with 4 mM propidium iodide (Sigma-Aldrich Co, St. Louis, MO, USA) in PBS for 5 min at room temperature to stain dead cells. After washing with PBS, the cell suspensions were mounted on glass slides and observed by fluorescence microscopy (AxioImager M1, Zeiss, Germany) using the filter set for Rhodamine-phalloidin.

SUPPLEMENTARY FIGURES

A

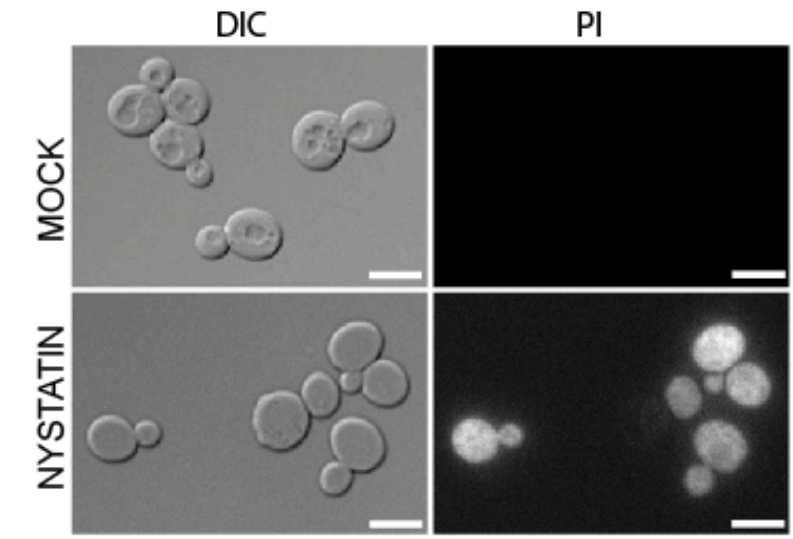

B

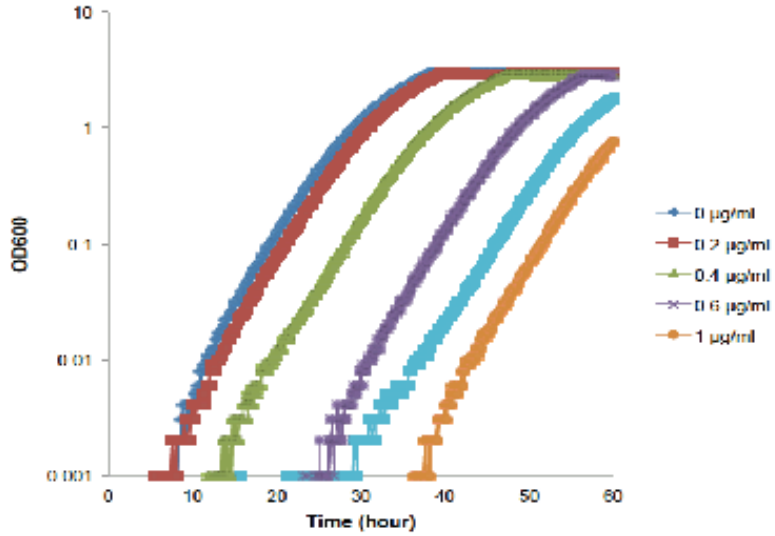

C

Concentration (μg/ml)	Doubling time (hour)	Ratio (%)
0.0	2.6	100.0
0.2	2.6	100.5
0.4	2.7	102.5
0.6	2.6	97.5
0.8	2.6	100.5
1.0	2.5	96.8

Figure S1. Growth inhibition and cellular effect of nystatin.

(A) Wild-type cells in culture were harvested after 1 h of incubation with nystatin (100 μg mL^{-1}, final concentration), stained with propidium iodide (PI), and directly observed under a fluorescence microscope with differential interference contrast (DIC, left panel) and a red filter (right panel). Microscopic examination shows images of dead cells without any significant morphological alteration. Bar, 5 μm. (B) Wild-type cells were grown in 4 ml of YPD medium containing the dose-dependent concentrations of nystatin at 25°C in L-shaped test tubes. The $OD_{600\ nm}$ was measured using a biophotorecorder. (C) The doubling time was calculated using consecutive data points of the measured values ranging from 0.1 to 0.2, and the relative growth inhibition ratio was calculated by dividing the doubling time of nystatin-treated cells by that of mock-treated cells.

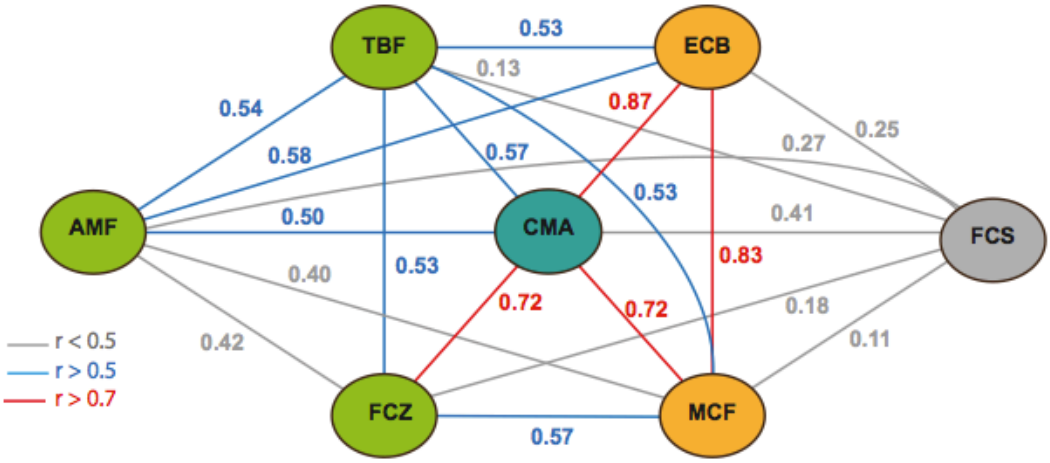

Figure S1. Correlational network for ergosterol-, V-ATPase-, and cell-wall-acting agents.

Correlation of the morphological profile was estimated from the 102 variables of the PC scores of each agent by the phenotypic profiling approach reported in Ohnuki *et al.* (Ohnuki *et al.*, 2010). Red and green lines, and score near each line, denote the degree of association—strong ($r > 0.7$), moderate ($r > 0.5$) and weak ($r < 0.5$) correlation. High degrees of similarities were noted across drugs.

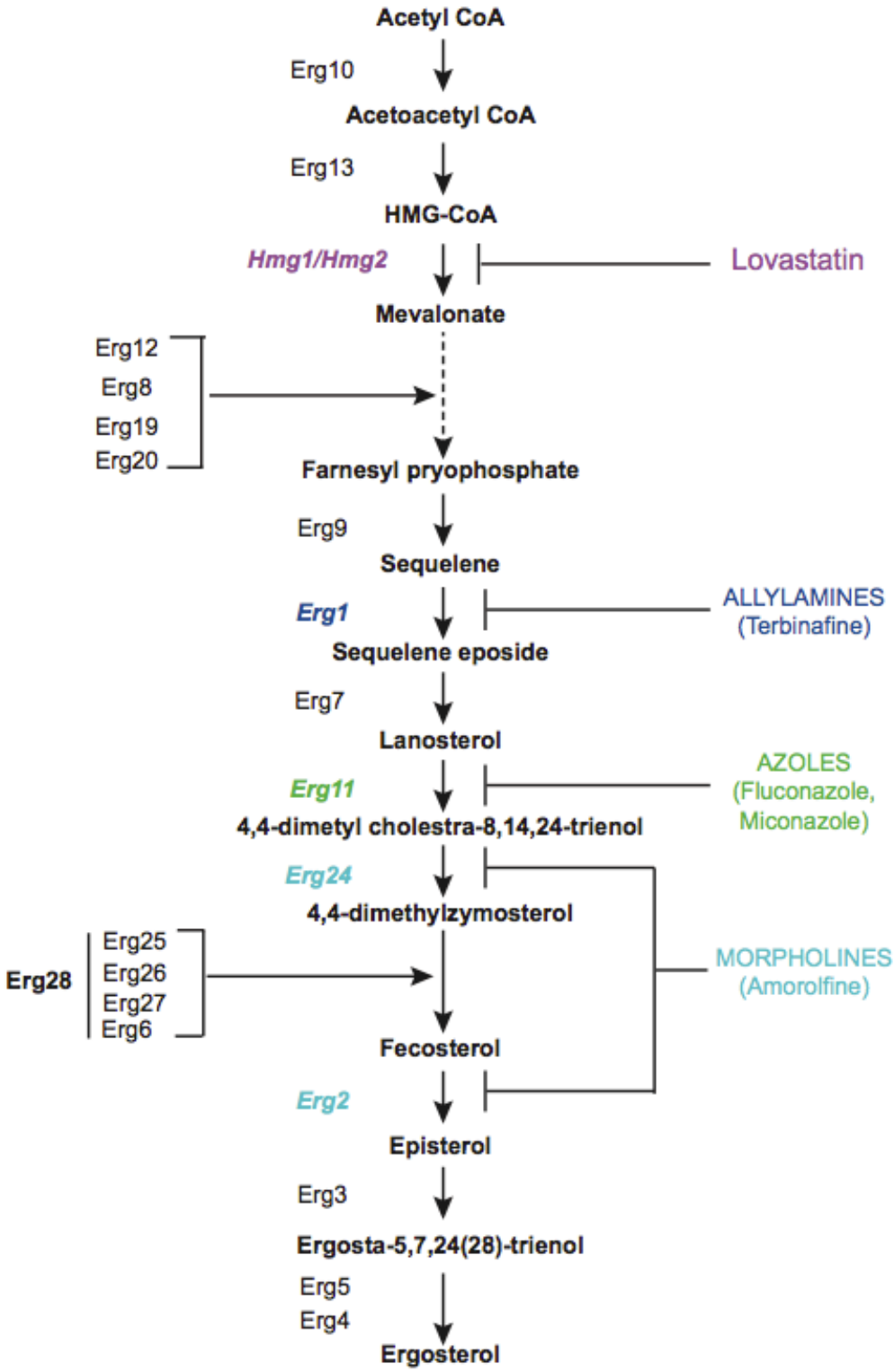

Figure S2. Commonly used antifungal drugs affecting ergosterol biosynthesis pathway of budding yeast, *S. cerevisiae.*

Important intermediates of the pathway are shown in schematic linear model. Principal enzymes and drugs inhibiting key intermediates are indicated on the left and right side respectively. Antifungal drugs used in this study include allylamines (terbinafine), azoles (fluconazole and miconazole), morpholines (amorolfine) and lovastatin are listed beneath the class names. The role position of Erg28 in the pathway was indicated in boldface. HMG, hydroxymethyl glutaryl; CoA, Coenzyme A.

SUPPLEMENTARY TABLES

Table S1A. List of parameters significantly affected by fluconazole

Rank	ID	Description	Z value	P value	Q value
1	DCV179_C	CV_of_Nuclear_minimum_radius_in_mother	4.1355	3.54E-05	0.0077
2	DCV14-1_A	CV_of_Nuclear_size	3.9443	8.00E-05	0.0077
3	C115_A1B	Mother_axis_ratio	-3.8486	1.19E-04	0.0077
4	CCV126_A1B	CV_of_Brightness_difference_of_cell_wall	3.8486	1.19E-04	0.0077
5	DCV14-1_C	CV_of_Nuclear_size_in_mother	3.7530	1.75E-04	0.0091
6	DCV173_A	CV_of_Maximal_distance_between_nuclear_gravity_center_and_nuclear_outline	3.7052	2.11E-04	0.0092
7	C115_A	Whole_cell_axis_ratio	-3.6574	2.55E-04	0.0095
8	ACV103_A1B	CV_of_Relative_distance_of_actin_patch_center_from_neck_in_mother	3.3705	7.50E-04	0.0244
9	C115_C	Mother_axis_ratio	-3.3227	8.91E-04	0.0258
10	C126_A	Brightness_difference_of_cell_wall	-3.2749	0.0011	0.0271
11	ACV8-1_A	CV_of_Actin_region_brightness	3.2271	0.0013	0.0271
12	DCV14-3_C	CV_of_Nuclear_size_in_whole_cell	3.2271	0.0013	0.0271
13	DCV176_A	CV_of_Nuclear_long_axis_length	3.0837	0.0020	0.0332
14	DCV179_A	CV_of_Nuclear_minimum_radius	3.0837	0.0020	0.0332
15	ACV123_A1B	CV_of_Ratio_of_actin_patches_to_actin_region	3.0837	0.0020	0.0332
16	A107	actin_c_api_ratio	-3.0837	0.0020	0.0332
17	A118	actin_e_ratio_to_budded_cells	3.0359	0.0024	0.0367

Table S1B. List of parameters significantly affected by terbinafine

Rank	ID	Description	Z value	P value	Q value
1	C115_A	Whole_cell_axis_ratio	-5.7297	1.01E-08	2.23E-06
2	C115_C	Mother_axis_ratio	-5.6572	1.54E-08	2.23E-06
3	C115_A1B	Mother_axis_ratio	-5.5846	2.34E-08	2.26E-06
4	C114_C	Bud_axis_ratio	-4.6780	2.90E-06	2.10E-04
5	C104_C	Short_axis_length_in_mother	4.4967	6.90E-06	4.00E-04
6	C13_A	Whole_cell_fitness_for_ellipse	-4.3517	1.35E-05	5.60E-04
7	CCV110_C	CV_of_Distance_between_bud_tip_and_mother_long_axis_extension	4.3517	1.35E-05	5.60E-04
8	C104_A1B	Short_axis_length_in_mother	4.2791	1.88E-05	6.80E-04
9	C13_C	Mother_cell_fitness_for_ellipse	-4.2429	2.21E-05	7.11E-04
10	C13_A1B	Mother_cell_fitness_for_ellipse	-3.9165	8.98E-05	0.0026
11	CCV106_C	CV_of_Bud_direction	3.8802	1.04E-04	0.0028
12	C109_A1B	Neck_width	3.8077	1.40E-04	0.0034
13	C126_A	Brightness_difference_of_cell_wall	-3.6989	2.17E-04	0.0048
14	DCV173_A	CV_of_Maximal_distance_between_nuclear_gravity_center_and_nuclear_outline	3.5901	3.31E-04	0.0064
15	C114_A1B	Bud_axis_ratio	-3.5901	3.31E-04	0.0064
16	C109_C	Neck_width	3.5539	3.80E-04	0.0069
17	D177_C	Nuclear_long_axis_length_in_bud	3.5176	4.35E-04	0.0074
18	C104_A	Short_axis_length_in_whole_cell	3.4451	5.71E-04	0.0083
19	C108_C	Short_axis_length_in_bud	3.4451	5.71E-04	0.0083
20	D174_C	Maximal_distance_between_nuclear_gravity_center_and_nuclear_outline_in_bud	3.4451	5.71E-04	0.0083
21	DCV176_A	CV_of_Nuclear_long_axis_length	3.3725	7.45E-04	0.0103
22	D14-2_C	Nuclear_size_in_bud	3.3549	7.94E-04	0.0103
23	DCV17-1_A	CV_of_Nuclear_fitness_for_ellipse	3.3363	8.49E-04	0.0103
24	C106_C	Bud_direction	-3.3363	8.49E-04	0.0103
25	C106_A1B	Bud_direction	-3.3000	9.67E-04	0.0108
26	D14-3_A1B	Nuclear_size	3.3000	9.67E-04	0.0108
27	C11-1_A1B	Mother_cell_size	3.2275	0.0012	0.0129
28	D15-3_A1B	Nuclear_brightness	3.2275	0.0012	0.0129
29	D157_C	Angle_between_C2D2-2_and_C2C4-2	3.1912	0.0014	0.0142
30	D188_A	Distance_between_nuclear_gravity_center_and_brightest_point	3.1187	0.0018	0.0170
31	D15-3_C	Nuclear_brightness_in_whole_cell	3.1187	0.0018	0.0170
32	D176_A	Nuclear_long_axis_length	3.0462	0.0023	0.0192
33	DCV14-1_A	CV_of_Nuclear_size	3.0462	0.0023	0.0192
34	DCV102_A	CV_of_Distance_between_nuclear_gravity_center_and_mother_tip	3.0462	0.0023	0.0192
35	C11-1_C	Mother_cell_size	3.0462	0.0023	0.0192

36	D175_A1B	Maximal_distance_between_nuclear_gravity_center_and_nuclear_outline	3.0099	0.0026	0.0205
37	CCV110_A1B	CV_of_Distance_between_bud_tip_and_mother_long_axis_extension	3.0099	0.0026	0.0205
38	D173_A	Maximal_distance_between_nuclear_gravity_center_and_nuclear_outline	2.9736	0.0029	0.0225
39	CCV106_A1B	CV_of_Bud_direction	2.9374	0.0033	0.0234
40	C101_C	Whole_cell_size	2.9374	0.0033	0.0234
41	D14-3_C	Nuclear_size_in_whole_cell	2.9374	0.0033	0.0234
42	D179_A	Nuclear_minimum_radius	2.9011	0.0037	0.0251
43	D156_C	Angle_between_C2D1-2_and_C2C4-2	2.9011	0.0037	0.0251
44	D15-1_A	Nuclear_brightness	2.8648	0.0042	0.0257
45	C111_C	Distance_between_bud_tip_and_mother_short_axis_extension	2.8648	0.0042	0.0257
46	D180_C	Nuclear_minimum_radius_in_bud	2.8648	0.0042	0.0257
47	DCV123_C	CV_of_Ratio_of_D121_to_C107	-2.8648	0.0042	0.0257
48	CCV104_A1B	CV_of_Short_axis_length_in_mother	2.8286	0.0047	0.0282
49	D14-1_A	Nuclear_size	2.7923	0.0052	0.0292
50	C112_A1B	Distance_between_middle_point_of_neck_and_mother_center	2.7923	0.0052	0.0292
51	C128_A1B	Distance_between_middle_point_of_neck_and_mother_hip	2.7923	0.0052	0.0292
52	D178_A1B	Nuclear_long_axis_length	2.7923	0.0052	0.0292

Table S1C. List of parameters significantly affected by amorolfine.

Rank	ID.	Description	Z value	P value	Q value
1	C115_A1B	Mother_axis_ratio	-4.0408	5.33E-05	0.0240
2	C126_A	Brightness_difference_of_cell_wall	-3.1801	1.47E-03	0.1022
3	CCV11-2_A1B	CV_of_Bud_cell_size	3.2757	1.05E-03	0.1022
4	C115_C	Mother_axis_ratio	-3.0844	2.04E-03	0.1022
5	CCV12-2_A1B	CV_of_Bud_cell_outline_length	3.2279	1.25E-03	0.1022
6	C126_A1B	Brightness_difference_of_cell_wall	-3.2757	1.05E-03	0.1022
7	CCV118_A1B	CV_of_Cell_size_ratio	3.1322	1.73E-03	0.1022
8	DCV145_A1B	CV_of_Distance_between_nuclear_outline_point_D7_and_mother_hip	3.0844	2.04E-03	0.1022
9	CCV13_C	CV_of_Mother_cell_fitness_for_ellipse	-3.3235	8.89E-04	0.1022

Table S1D. List of parameters significantly affected by flucytosine

Rank	ID	Description	Z value	P value	Q value
1	D17-1_A	Nuclear_fitness_for_ellipse	4.7570	1.96E-06	4.77E-04
2	A7-1_A	Size_of_actin_region	4.7092	2.49E-06	4.77E-04
3	D182_A	Nuclear_axis_ratio	4.5658	4.98E-06	6.37E-04
4	D154_A	Angle_between_C1D1-1_and_C1C1-2	-4.2789	1.88E-05	0.0018
5	A101_A	Actin_region_ratio_in_whole_cell	3.8964	9.76E-05	0.0062
6	D125_C	Distance_between_nuclear_gravity_center_in_mother_and_mother_hip	3.8964	9.76E-05	0.0062
7	DCV188_C	CV_of_Distance_between_nuclear_gravity_center_and_brightest_point_in_mother	3.8486	1.19E-04	0.0065
8	D141_C	Distance_between_nuclear_brightest_point_in_mother_and_mother_hip	3.7530	1.75E-04	0.0082
9	DCV182_A	CV_of_Nuclear_axis_ratio	3.6574	2.55E-04	0.0082
10	ACV7-1_A1B	CV_of_Size_of_actin_region_in_mother	3.6574	2.55E-04	0.0082
11	D17-1_C	Nuclear_fitness_for_ellipse_in_mother	3.6574	2.55E-04	0.0082
12	D103_C	Distance_between_nuclear_gravity_center_in_mother_and_mother_tip	3.6574	2.55E-04	0.0082
13	A106_A	Actin_b_ratio	-3.5140	4.41E-04	0.0119
14	A105_A	Actin_a_ratio	3.4662	5.28E-04	0.0119
15	ACV8-1_A1B	CV_of_Total_brightness_of_actin_region_in_mother	3.4662	5.28E-04	0.0119
16	D128_C	Distance_between_nuclear_brightest_point_in_mother_and_mother_tip	3.4662	5.28E-04	0.0119
17	A115	actin_b_ratio_to_no_bud_cells	-3.4662	5.28E-04	0.0119
18	ACV123_A	CV_of_Ratio_of_actin_patches_to_actin_region	3.3227	8.91E-04	0.0156
19	DCV105_A	CV_of_Ratio_of_D102_to_C103	3.3227	8.91E-04	0.0156
20	C113_A1B	Distance_between_bud_tip_and_mother_long_axis_through_middle_point_of_neck	3.3227	8.91E-04	0.0156
21	ACV9_A1B	CV_of_Proportion_of_actin_region_at_neck	3.3227	8.91E-04	0.0156
22	A114	actin_a_ratio_to_no_bud_cells	3.3227	8.91E-04	0.0156
23	D127_A	Distance_between_nuclear_brightest_point_and_cell_tip	3.2749	0.0011	0.0176
24	DCV102_A	CV_of_Distance_between_nuclear_gravity_center_and_mother_tip	3.2271	0.0013	0.0200
25	C102_A1B	Whole_cell_outline_length	3.1793	0.0015	0.0227
26	DCV17-1_A	CV_of_Nuclear_fitness_for_ellipse	3.1315	0.0017	0.0257
27	D203	nuclear_D_ratio	3.0904	0.0020	0.0271
28	CCV104_A	CV_of_Short_axis_length_in_whole_cell	3.0837	0.0020	0.0271
29	DCV127_A	CV_of_Distance_between_nuclear_	3.0837	0.0020	0.0271

		brightest_point_and_cell_tip			
30	D135_A	Distance_between_nuclear_brightest_point_and_cell_center	3.0359	0.0024	0.0307
31	A111	actin_ae_ratio	3.0127	0.0026	0.0321
32	A9_A1B	Proportion_of_actin_region_at_neck	-2.9881	0.0028	0.0327
33	A112	actin_bcd_ratio	-2.9881	0.0028	0.0327
34	D106_C	Ratio_of_D103_to_C103	2.9403	0.0033	0.0349
35	DCV173_C	CV_of_Maximal_distance_between_nuclear_gravity_center_and_nuclear_outline_in_mother	2.9403	0.0033	0.0349
36	D206	nuclear_A_ratio_to_no_bud_cells	-2.9048	0.0037	0.0349
37	DCV188_A	CV_of_Distance_between_nuclear_gravity_center_and_brightest_point	2.8925	0.0038	0.0349
38	C105_A1B	Neck_position	2.8925	0.0038	0.0349
39	A103_A1B	Relative_distance_of_actin_patch_center_from_neck_in_mother	2.8925	0.0038	0.0349
40	C117_C	Cell_outline_ratio	-2.8925	0.0038	0.0349
41	DCV176_C	CV_of_Nuclear_long_axis_length_in_mother	2.8925	0.0038	0.0349
42	DCV197_C	CV_of_Ratio_of_nuclear_size	2.8925	0.0038	0.0349
43	D170_A1B	Angle_between_C4-1D2-1_and_C4-1C1	2.8446	0.0044	0.0379
44	C118_C	Cell_size_ratio	-2.8446	0.0044	0.0379
45	D182_C	Nuclear_axis_ratio_in_mother	2.8446	0.0044	0.0379
46	D105_A	Ratio_of_D102_to_C103	2.7968	0.0052	0.0404
47	D155_A	Angle_between_C1D2-1_and_C1C1-2	-2.7968	0.0052	0.0404
48	C110_A1B	Distance_between_bud_tip_and_mother_long_axis_extension	2.7968	0.0052	0.0404
49	DCV182_C	CV_of_Nuclear_axis_ratio_in_mother	2.7968	0.0052	0.0404

Table S1E. List of parameters significantly affected by echinocandin B

Rank	ID	Description	Z value	P value	Q value
1	C124_C	Medium_bud_ratio	5.8580	4.68E-09	1.67E-07
2	C125_C	Large_bud_ratio	-5.8566	4.72E-09	1.67E-07
3	C115_A1B	Mother_axis_ratio	-5.7132	1.11E-08	1.67E-07
4	CCV11-1_A	CV_of_Whole_cell_size	5.6654	1.47E-08	1.67E-07
5	CCV112_A1B	CV_of_Distance_between_middle_point_of_neck_&_mother_center	5.6654	1.47E-08	1.67E-07
6	C115_C	Mother_axis_ratio	-5.6654	1.47E-08	1.67E-07
7	CCV12-1_A	CV_of_Whole_cell_outline_length	5.6176	1.94E-08	1.67E-07
8	CCV128_A1B	CV_of_Distance_between_middle_point_of_neck_and_mother_hip	5.6176	1.94E-08	1.67E-07
9	C109_C	Neck_width	5.6176	1.94E-08	1.67E-07
10	CCV104_A	CV_of_Short_axis_length_in_whole_cell	5.5698	2.55E-08	1.98E-07
11	CCV103_A	CV_of_Long_axis_length_in_whole_cell	5.4741	4.40E-08	3.10E-07
12	D203	nuclear_D_ratio	5.3775	7.55E-08	4.88E-07
13	D176_A	Nuclear_long_axis_length	5.2829	1.27E-07	6.61E-07
14	C117_C	Cell_outline_ratio	-5.2829	1.27E-07	6.61E-07
15	D173_A	Maximal_distance_between_nuclear_gravity_center_and_nuclear_outline	5.2351	1.65E-07	6.61E-07
16	DCV176_A	CV_of_Nuclear_long_axis_length	5.2351	1.65E-07	6.61E-07
17	C104_C	Short_axis_length_in_mother	5.2351	1.65E-07	6.61E-07
18	D179_C	Nuclear_minimum_radius_in_mother	5.2351	1.65E-07	6.61E-07
19	D17-1_A	Nuclear_fitness_for_ellipse	5.1873	2.13E-07	6.61E-07
20	D179_A	Nuclear_minimum_radius	5.1873	2.13E-07	6.61E-07
21	DCV127_A	CV_of_Distance_between_nuclear_brightest_point_and_cell_tip	5.1873	2.13E-07	6.61E-07
22	C118_C	Cell_size_ratio	-5.1873	2.13E-07	6.61E-07
23	A8-1_C	Total_brightness_of_actin_region_in_mother	5.1873	2.13E-07	6.61E-07
24	CCV11-2_C	CV_of_Bud_cell_size	5.1873	2.13E-07	6.61E-07
25	CCV112_C	CV_of_Distance_between_middle_point_of_neck_and_mother_center	5.1873	2.13E-07	6.61E-07
26	D14-1_A	Nuclear_size	5.1407	2.74E-07	7.36E-07
27	D178_A1B	Nuclear_long_axis_length	5.1395	2.75E-07	7.36E-07
28	CCV12-1_A1B	CV_of_Mother_cell_outline_length	5.1395	2.75E-07	7.36E-07
29	CCV108_C	CV_of_Short_axis_length_in_bud	5.1395	2.75E-07	7.36E-07
30	DCV102_A	CV_of_Distance_between_nuclear_gravity_center_and_mother_tip	5.0917	3.55E-07	8.34E-07
31	CCV102_C	CV_of_Whole_cell_outline_length	5.0917	3.55E-07	8.34E-07
32	CCV128_C	CV_of_Distance_between_middle	5.0917	3.55E-07	8.34E-07

		_point_of_neck_and_mother_hip			
33	A118	actin_e_ratio_to_budded_cells	5.0917	3.55E-07	8.34E-07
34	DCV179_A	CV_of_Nuclear_minimum_radius	5.0439	4.56E-07	9.56E-07
35	D14-3_A1B	Nuclear_size	5.0439	4.56E-07	9.56E-07
36	D14-1_C	Nuclear_size_in_mother	5.0439	4.56E-07	9.56E-07
37	CCV12-2_C	CV_of_Bud_cell_outline_length	5.0439	4.56E-07	9.56E-07
38	D206	nuclear_A_ratio_to_no_bud_cells	-5.0070	5.53E-07	1.03E-06
39	D204	nuclear_E_ratio	5.0006	5.72E-07	1.03E-06
40	D175_A1B	Maximal_distance_between_nuclear_gravity_center_and_nuclear_outline	4.9961	5.85E-07	1.03E-06
41	CCV103_A1B	CV_of_Long_axis_length_in_mother	4.9961	5.85E-07	1.03E-06
42	DCV181_A1B	CV_of_Nuclear_minimum_radius	4.9961	5.85E-07	1.03E-06
43	CCV101_C	CV_of_Whole_cell_size	4.9961	5.85E-07	1.03E-06
44	CCV107_C	CV_of_Long_axis_length_in_bud	4.9961	5.85E-07	1.03E-06
45	DCV14-1_A	CV_of_Nuclear_size	4.9482	7.49E-07	1.21E-06
46	D181_A1B	Nuclear_minimum_radius	4.9482	7.49E-07	1.21E-06
47	CCV11-1_A1B	CV_of_Mother_cell_size	4.9482	7.49E-07	1.21E-06
48	D14-3_C	Nuclear_size_in_whole_cell	4.9482	7.49E-07	1.21E-06
49	C115_A	Whole_cell_axis_ratio	-4.9004	9.56E-07	1.45E-06
50	DCV173_A	CV_of_Maximal_distance_between_nuclear_gravity_center_and_nuclear_outline	4.9004	9.56E-07	1.45E-06
51	DCV104_A1B	CV_of_Distance_between_nuclear_gravity_center_and_mother_tip	4.9004	9.56E-07	1.45E-06
52	A113_A	Actin_n_ratio	4.8566	1.19E-06	1.63E-06
53	D188_A	Distance_between_nuclear_gravity_center_and_brightest_point	4.8526	1.22E-06	1.63E-06
54	D15-3_A1B	Nuclear_brightness	4.8526	1.22E-06	1.63E-06
55	CCV104_A1B	CV_of_Short_axis_length_in_mother	4.8526	1.22E-06	1.63E-06
56	ACV8-1_A1B	CV_of_Total_brightness_of_actin_region_in_mother	4.8526	1.22E-06	1.63E-06
57	ACV102_A1B	CV_of_Bud_actin_region_ratio_to_total_region	4.8526	1.22E-06	1.63E-06
58	DCV196_A1B	CV_of_Maximal_intensity_of_nuclear_brightness_divided_by_average	4.8526	1.22E-06	1.63E-06
59	C104_A1B	Short_axis_length_in_mother	4.8048	1.55E-06	1.91E-06
60	C117_A1B	Cell_outline_ratio	-4.8048	1.55E-06	1.91E-06
61	C118_A1B	Cell_size_ratio	-4.8048	1.55E-06	1.91E-06
62	DCV126_A1B	CV_of_Distance_between_nuclear_gravity_center_and_mother_hip	4.8048	1.55E-06	1.91E-06
63	CCV12-1_C	CV_of_Mother_cell_outline_length	4.8048	1.55E-06	1.91E-06
64	D182_A	Nuclear_axis_ratio	4.7570	1.96E-06	2.24E-06
65	D17-3_A1B	Nuclear_fitness_for_ellipse	4.7570	1.96E-06	2.24E-06
66	ACV8-2_A1B	CV_of_Total_brightness_of_actin_region_in_bud	4.7570	1.96E-06	2.24E-06

67	A102_C	Bud_actin_region_ratio_to_total_region	-4.7570	1.96E-06	2.24E-06
68	D207	nuclear_A1_ratio_to_budded_cells	-4.7570	1.96E-06	2.68E-06
69	C125_A1B	Large_bud_ratio	-4.7126	2.45E-06	2.68E-06
70	DCV15-1_A	CV_of_Nuclear_brightness	4.7092	2.49E-06	2.68E-06
71	CCV117_C	CV_of_Cell_outline_ratio	4.7092	2.49E-06	2.68E-06
72	CCV118_C	CV_of_Cell_size_ratio	4.7092	2.49E-06	2.68E-06
73	ACV7-1_A1B	CV_of_Size_of_actin_region_in_mother	4.6614	3.14E-06	3.12E-06
74	C11-1_C	Mother_cell_size	4.6614	3.14E-06	3.12E-06
75	A7-1_C	Size_of_actin_region_in_mother	4.6614	3.14E-06	3.12E-06
76	D14-2_C	Nuclear_size_in_bud	4.6614	3.14E-06	3.12E-06
77	CCV11-1_C	CV_of_Mother_cell_size	4.6614	3.14E-06	3.12E-06
78	A112	actin_bcd_ratio	-4.6614	3.14E-06	3.12E-06
79	A102_A1B	Bud_actin_region_ratio_to_total_region	-4.6136	3.96E-06	3.83E-06
80	A103_A1B	Relative_distance_of_actin_patch_center_from_neck_in_mother	4.6136	3.96E-06	3.83E-06
81	CCV101_A1B	CV_of_Whole_cell_size	4.5658	4.98E-06	4.59E-06
82	D17-1_C	Nuclear_fitness_for_ellipse_in_mother	4.5658	4.98E-06	4.59E-06
83	D103_C	Distance_between_nuclear_gravity_center_in_mother_and_mother_tip	4.5658	4.98E-06	4.59E-06
84	D177_C	Nuclear_long_axis_length_in_bud	4.5658	4.98E-06	4.59E-06
85	D15-1_A	Nuclear_brightness	4.5180	6.24E-06	5.04E-06
86	C12-2_A1B	Bud_cell_outline_length	-4.5180	6.24E-06	5.04E-06
87	A109_A1B	Actin_e_ratio	4.5180	6.24E-06	5.04E-06
88	D15-1_C	Nuclear_brightness_in_mother	4.5180	6.24E-06	5.04E-06
89	D173_C	Maximal_distance_between_nuclear_gravity_center_and_nuclear_outline_in_mother	4.5180	6.24E-06	5.04E-06
90	D174_C	Maximal_distance_between_nuclear_gravity_center_and_nuclear_outline_in_bud	4.5180	6.24E-06	5.04E-06
91	D176_C	Nuclear_long_axis_length_in_mother	4.5180	6.24E-06	5.04E-06
92	CCV104_C	CV_of_Short_axis_length_in_mother	4.5180	6.24E-06	5.04E-06
93	CCV113_C	CV_of_Distance_between_bud_tip_and_mother_long_axis_through_middle_point_of_neck	4.5180	6.24E-06	5.04E-06
94	DCV186_C	CV_of_Total_length_of_two_straight_segments_D12-1C4-1_and_D12-2C4-1	4.5180	6.24E-06	5.04E-06
95	A109	actin_e_ratio	4.5180	6.24E-06	5.04E-06
96	D200	nuclear_A1_ratio	-4.5180	6.24E-06	5.04E-06
97	DCV117_A	CV_of_Distance_between_nuclear_gravity_center_and_cell_center	4.4702	7.82E-06	6.00E-06
98	DCV147_A	CV_of_Relative_distance_of_nuclear_gravity_center_to_cell_center	4.4702	7.82E-06	6.00E-06

99	DCV194_A	CV_of_Maximal_intensity_of_nuclear_brightness_divided_by_average	4.4702	7.82E-06	6.00E-06
100	D169_C	Angle_between_C4-1D1-1_and_C4-1C1	4.4702	7.82E-06	6.00E-06
101	DCV185_C	CV_of_Total_length_of_two_straight_segments_D11-1C4-1_and_D11-2C4-1	4.4702	7.82E-06	6.00E-06
102	A113	actin_n_ratio	4.4258	9.61E-06	7.30E-06
103	D128_C	Distance_between_nuclear_brightest_point_in_mother_and_mother_tip	4.4223	9.76E-06	7.35E-06
104	A7-2_A1B	Size_of_actin_region_in_bud	-4.3745	1.22E-05	8.73E-06
105	D131_C	Distance_between_nuclear_brightest_point_in_bud_and_middle_point_of_neck	-4.3745	1.22E-05	8.73E-06
106	D141_C	Distance_between_nuclear_brightest_point_in_mother_and_mother_hip	4.3745	1.22E-05	8.73E-06
107	D170_C	Angle_between_C4-1D2-1_and_C4-1C1	4.3745	1.22E-05	8.73E-06
108	ACV122_C	CV_of_Number_of_bright_actin_patches	4.3745	1.22E-05	8.73E-06
109	DCV14-3_A1B	CV_of_Nuclear_size	4.3267	1.51E-05	1.04E-05
110	D125_C	Distance_between_nuclear_gravity_center_in_mother_and_mother_hip	4.3267	1.51E-05	1.04E-05
111	CCV13_C	CV_of_Mother_cell_fitness_for_ellipse	4.3267	1.51E-05	1.04E-05
112	DCV15-1_C	CV_of_Nuclear_brightness_in_mother	4.3267	1.51E-05	1.04E-05
113	DCV179_C	CV_of_Nuclear_minimum_radius_in_mother	4.3267	1.51E-05	1.04E-05
114	A7-1_A1B	Size_of_actin_region_in_mother	4.2789	1.88E-05	1.25E-05
115	DCV14-1_C	CV_of_Nuclear_size_in_mother	4.2789	1.88E-05	1.25E-05
116	DCV177_C	CV_of_Nuclear_long_axis_length_in_bud	4.2789	1.88E-05	1.25E-05
117	C11-2_A1B	Bud_cell_size	-4.2311	2.33E-05	1.49E-05
118	C107_A1B	Long_axis_length_in_bud	-4.2311	2.33E-05	1.49E-05
119	D15-2_C	Nuclear_brightness_in_bud	4.2311	2.33E-05	1.49E-05
120	D15-3_C	Nuclear_brightness_in_whole_cell	4.2311	2.33E-05	1.49E-05
121	D180_C	Nuclear_minimum_radius_in_bud	4.2311	2.33E-05	1.49E-05
122	CCV115_A	CV_of_Whole_cell_axis_ratio	4.1833	2.87E-05	1.73E-05
123	A112_A1B	Actin_cd_ratio	-4.1833	2.87E-05	1.73E-05
124	D132_A1B	Distance_between_nuclear_brightest_point_and_middle_point_of_neck	4.1833	2.87E-05	1.73E-05
125	A108_C	Actin_d_iso_ratio	-4.1833	2.87E-05	1.73E-05
126	D109_C	Distance_between_nuclear_gravity_center_in_bud_and_middle_point_of_neck	-4.1833	2.87E-05	1.73E-05

127	DCV174_C	CV_of_Maximal_distance_between_nuclear_gravity_center_and_nuclear_outline_in_bud	4.1833	2.87E-05	1.73E-05
128	A117	actin_d_iso_ratio_to_budded_cells	-4.1833	2.87E-05	1.73E-05
129	D214	nuclear_A1_ratio_to_nuclear_A1BC_cells	-4.1833	2.87E-05	1.73E-05
130	DCV129_A1B	CV_of_Distance_between_nuclear_brightest_point_and_mother_tip	4.1355	3.54E-05	2.05E-05
131	C103_C	Long_axis_length_in_mother	4.1355	3.54E-05	2.05E-05
132	DCV130_C	CV_of_Distance_between_nuclear_brightest_point_in_mother_and_middle_point_of_neck	4.1355	3.54E-05	2.05E-05
133	D211	nuclear_A1_ratio_to_nuclear_AA1BC_cells	-4.1355	3.54E-05	2.05E-05
134	D216	nuclear_C_ratio_to_nuclear_A1BC_cells	4.1355	3.54E-05	2.05E-05
135	DCV17-1_A	CV_of_Nuclear_fitness_for_ellipse	4.0877	4.36E-05	2.45E-05
136	DCV135_A	CV_of_Distance_between_nuclear_brightest_point_and_cell_center	4.0877	4.36E-05	2.45E-05
137	A112_C	Actin_cd_ratio	-4.0877	4.36E-05	2.45E-05
138	CCV126_C	CV_of_Brightness_difference_of_cell_wall	4.0877	4.36E-05	2.45E-05
139	C123_A1B	Small_bud_ratio	4.0408	5.33E-05	2.86E-05
140	C11-1_A1B	Mother_cell_size	4.0399	5.35E-05	2.86E-05
141	ACV9_A1B	CV_of_Proportion_of_actin_region_at_neck	4.0399	5.35E-05	2.86E-05
142	C128_C	Distance_between_middle_point_of_neck_and_mother_hip	4.0399	5.35E-05	2.86E-05
143	DCV17-1_C	CV_of_Nuclear_fitness_for_ellipse_in_mother	4.0399	5.35E-05	2.86E-05
144	DCV112_C	CV_of_Ratio_of_D108_to_C128	4.0399	5.35E-05	2.86E-05
145	DCV151_C	CV_of_Ratio_of_distance_between_each_nucleus_and_middle_point_of_neck	4.0399	5.35E-05	2.86E-05
146	A8-2_A1B	Total_brightness_of_actin_region_in_bud	-3.9921	6.55E-05	3.45E-05
147	D144_C	Distance_between_nuclear_outline_point_D6-2_in_bud_and_middle_point_of_neck	-3.9921	6.55E-05	3.45E-05
148	C127_A	Thickness_difference_of_cell_wall	3.9443	8.00E-05	4.05E-05
149	DCV182_A	CV_of_Nuclear_axis_ratio	3.9443	8.00E-05	4.05E-05
150	C109_A1B	Neck_width	3.9443	8.00E-05	4.05E-05
151	DCV145_A1B	CV_of_Distance_between_nuclear_outline_point_D7_and_mother_hip	3.9443	8.00E-05	4.05E-05
152	DCV198_C	CV_of_Ratio_of_nuclear_brightness	3.9443	8.00E-05	4.05E-05
153	A111	actin_ae_ratio	3.9443	8.00E-05	4.05E-05
154	D110_A1B	Distance_between_nuclear_gravity_center_and_middle_point_of_neck	3.8964	9.76E-05	4.82E-05

155	DCV118_A1B	CV_of_Distance_between_nuclear_gravity_center_and_mother_center	3.8964	9.76E-05	4.82E-05
156	CCV103_C	CV_of_Long_axis_length_in_mother	3.8964	9.76E-05	4.82E-05
157	DCV15-3_C	CV_of_Nuclear_brightness_in_whole_cell	3.8964	9.76E-05	4.82E-05
158	A7-1_A	Size_of_actin_region	3.8486	1.19E-04	5.68E-05
159	C127_C	Thickness_difference_of_cell_wall	3.8486	1.19E-04	5.68E-05
160	A8-2_C	Total_brightness_of_actin_region_in_bud	-3.8486	1.19E-04	5.68E-05
161	DCV14-3_C	CV_of_Nuclear_size_in_whole_cell	3.8486	1.19E-04	5.68E-05
162	DCV119_C	CV_of_Distance_between_nuclear_gravity_center_in_bud_and_bud_center	3.8486	1.19E-04	5.68E-05
163	CCV126_A1B	CV_of_Brightness_difference_of_cell_wall	3.8008	1.44E-04	6.73E-05
164	C12-1_C	Mother_cell_outline_length	3.8008	1.44E-04	6.73E-05
165	D106_C	Ratio_of_D103_to_C103	3.8008	1.44E-04	6.73E-05
166	DCV176_C	CV_of_Nuclear_long_axis_length_in_mother	3.8008	1.44E-04	6.73E-05
167	ACV122_A	CV_of_Number_of_bright_actin_patches	3.7530	1.75E-04	7.92E-05
168	DCV142_A1B	CV_of_Distance_between_nuclear_brightest_point_and_mother_hip	3.7530	1.75E-04	7.92E-05
169	D112_C	Ratio_of_D108_to_C128	-3.7530	1.75E-04	7.92E-05
170	D123_C	Ratio_of_D121_to_C107	3.7530	1.75E-04	7.92E-05
171	DCV131_C	CV_of_Distance_between_nuclear_brightest_point_in_bud_and_middle_point_of_neck	3.7530	1.75E-04	7.92E-05
172	DCV105_A	CV_of_Ratio_of_D102_to_C103	3.7052	2.11E-04	9.30E-05
173	C112_C	Distance_between_middle_point_of_neck_and_mother_center	3.7052	2.11E-04	9.30E-05
174	D145_C	Distance_between_nuclear_outline_point_D7_in_mother_and_mother_hip	3.7052	2.11E-04	9.30E-05
175	D153_C	Mobility_of_nucleus_in_bud	-3.7052	2.11E-04	9.30E-05
176	DCV173_C	CV_of_Maximal_distance_between_nuclear_gravity_center_and_nuclear_outline_in_mother	3.7052	2.11E-04	9.30E-05
177	C104_A	Short_axis_length_in_whole_cell	3.6574	2.55E-04	1.08E-04
178	C126_A	Brightness_difference_of_cell_wall	-3.6574	2.55E-04	1.08E-04
179	A106_A	Actin_b_ratio	-3.6574	2.55E-04	1.08E-04
180	CCV126_A	CV_of_Brightness_difference_of_cell_wall	3.6574	2.55E-04	1.08E-04
181	ACV123_A	CV_of_Ratio_of_actin_patches_to_actin_region	3.6574	2.55E-04	1.08E-04
182	D113_C	Ratio_of_D109_to_C107	-3.6574	2.55E-04	1.08E-04
183	ACV102_C	CV_of_Bud_actin_region_ratio_to_total_region	3.6574	2.55E-04	1.08E-04

184	A108_A1B	Actin_d_iso_ratio	-3.6096	3.07E-04	1.26E-04
185	D190_A1B	Distance_between_nuclear_gravity_center_and_brightest_point	3.6096	3.07E-04	1.26E-04
186	DCV110_A1B	CV_of_Distance_between_nuclear_gravity_center_and_middle_point_of_neck	3.6096	3.07E-04	1.26E-04
187	DCV152_C	CV_of_Mobility_of_nucleus_in_mother	3.6096	3.07E-04	1.26E-04
188	DCV196_C	CV_of_Maximal_intensity_of_nuclear_brightness_divided_by_average_in_whole cell	3.6096	3.07E-04	1.26E-04
189	DCV188_A	CV_of_Distance_between_nuclear_gravity_center_and_brightest_point	3.5618	3.68E-04	1.48E-04
190	CCV110_C	CV_of_Distance_between_bud_tip_and_mother_long_axis_extension	3.5618	3.68E-04	1.48E-04
191	ACV9_C	CV_of_Proportion_of_actin_region_at_neck	3.5618	3.68E-04	1.48E-04
192	DCV14-2_C	CV_of_Nuclear_size_in_bud	3.5618	3.68E-04	1.48E-04
193	D209	nuclear_C_ratio_to_budded_cells	3.5618	3.68E-04	1.48E-04
194	A109_C	Actin_e_ratio	3.5387	4.02E-04	1.61E-04
195	C12-1_A1B	Mother_cell_outline_length	3.5140	4.41E-04	1.73E-04
196	C101_A1B	Whole_cell_size	3.5140	4.41E-04	1.73E-04
197	CCV13_A1B	CV_of_Mother_cell_fitness_for_ellipse	3.5140	4.41E-04	1.73E-04
198	DCV194_C	CV_of_Maximal_intensity_of_nuclear_brightness_divided_by_average_in_mother	3.5140	4.41E-04	1.73E-04
199	C124	medium_bud_ratio_to_buded_cells	3.4909	4.81E-04	1.87E-04
200	DCV148_A	CV_of_Relative_distance_of_nuclear_brightest_point_to_cell_center	3.4662	5.28E-04	2.02E-04
201	CCV106_C	CV_of_Bud_direction	3.4662	5.28E-04	2.02E-04
202	ACV120_C	CV_of_Total_length_of_actin_patch_link	3.4662	5.28E-04	2.02E-04
203	DCV197_C	CV_of_Ratio_of_nuclear_size	3.4662	5.28E-04	2.02E-04
204	D184_A1B	Nuclear_axis_ratio	3.4184	6.30E-04	2.37E-04
205	D188_C	Distance_between_nuclear_gravity_center_and_brightest_point_in_mother	3.4184	6.30E-04	2.37E-04
206	A108	actin_d_iso_ratio	-3.4184	6.30E-04	2.37E-04
207	A123_A	Ratio_of_actin_patches_to_actin_region	-3.3705	7.50E-04	2.76E-04
208	C101_C	Whole_cell_size	3.3705	7.50E-04	2.76E-04
209	A7-2_C	Size_of_actin_region_in_bud	-3.3705	7.50E-04	2.76E-04
210	A9_C	Proportion_of_actin_region_at_neck	-3.3705	7.50E-04	2.76E-04
211	DCV143_C	CV_of_Distance_between_nuclear_outline_point_D6-1_in_mother_and_middle_point_of_neck	3.3705	7.50E-04	2.76E-04
212	A9_A1B	Proportion_of_actin_region_at_ne	-3.3227	8.91E-04	3.23E-04

		ck			
213	A103_C	Relative_distance_of_actin_patch_center_from_neck_in_mother	3.3227	8.91E-04	3.23E-04
214	CCV105_C	CV_of_Neck_position	3.3227	8.91E-04	3.23E-04
215	C11-1_A	Whole_cell_size	3.2749	0.0011	3.71E-04
216	D114_A1B	Ratio_of_D110_to_C128	3.2749	0.0011	3.71E-04
217	D152_A1B	Mobility_of_nucleus_in_mother	3.2749	0.0011	3.71E-04
218	DCV15-3_A1B	CV_of_Nuclear_brightness	3.2749	0.0011	3.71E-04
219	A104_C	Relative_distance_of_actin_patch_center_from_neck_in_bud	-3.2749	0.0011	3.71E-04
220	DCV108_C	CV_of_Distance_between_nuclear_gravity_center_in_mother_and_middle_point_of_neck	3.2749	0.0011	3.71E-04
221	DCV144_C	CV_of_Distance_between_nuclear_outline_point_D6-2_in_bud_and_middle_point_of_neck	3.2749	0.0011	3.71E-04
222	C123_C	Small_bud_ratio	3.2405	0.0012	4.17E-04
223	A105_A	Actin_a_ratio	3.2271	0.0013	4.27E-04
224	D170_A1B	Angle_between_C4-1D2-1_and_C4-1C1	3.2271	0.0013	4.27E-04
225	DCV107_A1B	CV_of_Ratio_of_D104_to_C103	3.2271	0.0013	4.27E-04
226	D189_C	Distance_between_nuclear_gravity_center_and_brightest_point_in_bud	3.2271	0.0013	4.27E-04
227	D197_C	Ratio_of_nuclear_size	-3.2271	0.0013	4.27E-04
228	C124_A1B	Medium_bud_ratio	-3.1808	0.0015	4.87E-04
229	A101_A	Actin_region_ratio_in_whole_cell	3.1793	0.0015	4.87E-04
230	A8-1_A1B	Total_brightness_of_actin_region_in_mother	3.1793	0.0015	4.87E-04
231	C110_C	Distance_between_bud_tip_and_mother_long_axis_extension	-3.1793	0.0015	4.87E-04
232	DCV17-2_C	CV_of_Nuclear_fitness_for_ellipse_in_bud	3.1793	0.0015	4.87E-04
233	DCV155_C	CV_of_Angle_between_C1D2-1_and_C1C1-2	3.1793	0.0015	4.87E-04
234	A114	actin_a_ratio_to_no_bud_cells	3.1793	0.0015	4.87E-04
235	A115	actin_b_ratio_to_no_bud_cells	-3.1793	0.0015	4.87E-04
236	D136_A1B	Distance_between_nuclear_brightest_point_and_mother_center	3.1315	0.0017	5.62E-04
237	DCV132_A1B	CV_of_Distance_between_nuclear_brightest_point_and_middle_point_of_neck	3.1315	0.0017	5.62E-04
238	C106_C	Bud_direction	-3.1315	0.0017	5.62E-04
239	D134_C	Distance_between_two_nuclear_brightest_points_through_middle_point_of_neck	-3.1315	0.0017	5.62E-04
240	D139_C	Distance_between_nuclear_brightest_point_in_bud_and_bud_tip	3.1315	0.0017	5.62E-04
241	D205	nuclear_F_ratio	3.0847	0.0020	6.39E-04
242	C12-1_A	Whole_cell_outline_length	3.0837	0.0020	6.39E-04

243	C103_A1B	Long_axis_length_in_mother	3.0837	0.0020	6.39E-04
244	C128_A1B	Distance_between_middle_point_of_neck_and_mother_hip	3.0837	0.0020	6.39E-04
245	CCV106_A1B	CV_of_Bud_direction	3.0837	0.0020	6.39E-04
246	DCV143_A1B	CV_of_Distance_between_nuclear_outline_point_D6-1_and_middle_point_of_neck	3.0837	0.0020	6.39E-04
247	DCV15-2_C	CV_of_Nuclear_brightness_in_bud	3.0837	0.0020	6.39E-04
248	DCV180_C	CV_of_Nuclear_minimum_radius_in_bud	3.0837	0.0020	6.39E-04
249	ACV103_A1B	CV_of_Relative_distance_of_actin_patch_center_from_neck_in_mother	3.0359	0.0024	7.41E-04
250	ACV7-1_C	CV_of_Size_of_actin_region_in_mother	3.0359	0.0024	7.41E-04
251	DCV158_C	CV_of_Angle_between_D1-1D1-2_and_C1-1C1-2	3.0359	0.0024	7.41E-04
252	C112_A1B	Distance_between_middle_point_of_neck_and_mother_center	2.9881	0.0028	8.27E-04
253	C126_A1B	Brightness_difference_of_cell_wall	-2.9881	0.0028	8.27E-04
254	D142_A1B	Distance_between_nuclear_brightest_point_and_mother_hip	2.9881	0.0028	8.27E-04
255	D17-2_C	Nuclear_fitness_for_ellipse_in_bud	2.9881	0.0028	8.27E-04
256	D116_C	Distance_between_two_nuclear_gravity_centers_through_middle_point_of_neck	-2.9881	0.0028	8.27E-04
257	D194_C	Maximal_intensity_of_nuclear_brightness_divided_by_average_in_mother	-2.9881	0.0028	8.27E-04
258	ACV121_C	CV_of_Maximal_distance_between_patches	2.9881	0.0028	8.27E-04
259	DCV149_C	CV_of_Relative_distance_of_nuclear_gravity_center_in_bud_to_bud_center	2.9881	0.0028	8.27E-04
260	DCV195_C	CV_of_Maximal_intensity_of_nuclear_brightness_divided_by_average_in_bud	2.9881	0.0028	8.27E-04
261	C125	large_bud_ratio_to_buded_cells	-2.9881	0.0028	8.27E-04
262	A105	actin_a_ratio	2.9881	0.0028	8.27E-04
263	D213	nuclear_C_ratio_to_nuclear_AA1BC_cells	2.9881	0.0028	8.27E-04
264	DCV147_A1B	CV_of_Relative_distance_of_nuclear_gravity_center_to_mother_center	2.9403	0.0033	9.48E-04
265	ACV8-1_C	CV_of_Total_brightness_of_actin_region_in_mother	2.9403	0.0033	9.48E-04
266	DCV137_C	CV_of_Distance_between_nuclear_brightest_point_in_bud_and_bud_center	2.9403	0.0033	9.48E-04
267	DCV183_C	CV_of_Nuclear_axis_ratio_in_bud	2.9403	0.0033	9.48E-04
268	DCV189_C	CV_of_Distance_between_nuclear	2.9403	0.0033	9.48E-04

		_gravity_center_and_brightest_point_in_bud			
269	ACV8-1_A	CV_of_Actin_region_brightness	2.8925	0.0038	0.0011
270	D186_C	Total_length_of_two_straight_segments_D12-1C4-1_and_D12-2C4-1	2.8925	0.0038	0.0011
271	DCV109_C	CV_of_Distance_between_nuclear_gravity_center_in_bud_and_middle_point_of_neck	2.8925	0.0038	0.0011
272	DCV159_C	CV_of_Angle_between_D2-1D2-2_and_C1-1C1-2	2.8925	0.0038	0.0011
273	A113_A1B	Actin_n_ratio	2.8499	0.0044	0.0012
274	DCV155_A	CV_of_Angle_between_C1D2-1_and_C1C1-2	2.8446	0.0044	0.0012
275	D185_C	Total_length_of_two_straight_segments_D11-1C4-1_and_D11-2C4-1	2.8446	0.0044	0.0012
276	DCV123_C	CV_of_Ratio_of_D121_to_C107	-2.8446	0.0044	0.0012
277	D121_C	Distance_between_nuclear_gravity_center_in_bud_and_bud_tip	2.7968	0.0052	0.0014
278	ACV120_A	CV_of_Total_length_of_actin_patch_link	2.7490	0.0060	0.0016
279	A104_A1B	Relative_distance_of_actin_patch_center_from_neck_in_bud	-2.7490	0.0060	0.0016
280	CCV108_A1B	CV_of_Short_axis_length_in_bud	-2.7490	0.0060	0.0016
281	DCV152_A1B	CV_of_Mobility_of_nucleus_in_mother	2.7490	0.0060	0.0016
282	ACV121_A	CV_of_Maximal_distance_between_patches	2.7012	0.0069	0.0019
283	D126_A1B	Distance_between_nuclear_gravity_center_and_mother_hip	2.7012	0.0069	0.0019
284	CCV109_A1B	CV_of_Neck_width	2.7012	0.0069	0.0019
285	D143_A1B	Distance_between_nuclear_outline_point_D6-1_and_middle_point_of_neck	2.6534	0.0080	0.0022
286	ACV120_A1B	CV_of_Total_length_of_actin_patch_link	2.6534	0.0080	0.0022
287	C116_C	Axis_ratio_ratio	2.6534	0.0080	0.0022
288	C127_A1B	Thickness_difference_of_cell_wall	2.6062	0.0092	0.0025
289	CCV111_A1B	CV_of_Distance_between_bud_tip_and_mother_short_axis_extension	2.6056	0.0092	0.0025
290	ACV7-2_A1B	CV_of_Size_of_actin_region_in_bud	2.6056	0.0092	0.0025
291	CCV102_A1B	CV_of_Whole_cell_outline_length	2.5578	0.0105	0.0027
292	C102_C	Whole_cell_outline_length	2.5578	0.0105	0.0027
293	C111_C	Distance_between_bud_tip_and_mother_short_axis_extension	2.5578	0.0105	0.0027
294	D16-1_C	Maximal_intensity_of_nuclear_brightness_in_mother	-2.5578	0.0105	0.0027
295	D158_C	Angle_between_D1-1D1-2_and_C1-1C1-2	-2.5578	0.0105	0.0027
296	ACV101_C	CV_of_Actin_region_ratio_in_wh	2.5578	0.0105	0.0027

		ole_cell			
297	DCV135_C	CV_of_Distance_between_nuclear_brightest_point_in_mother_and_mother_center	2.5578	0.0105	0.0027
298	DCV167_C	CV_of_Angle_between_D2-1D2-2_and_C4-1C4-2	2.5578	0.0105	0.0027
299	A106	actin_b_ratio	-2.5578	0.0105	0.0027
300	A113_C	Actin_n_ratio	2.5086	0.0121	0.0031
301	C110_A1B	Distance_between_bud_tip_and_mother_long_axis_extension	-2.4622	0.0138	0.0035
302	ACV121_A1B	CV_of_Maximal_distance_between_patches	2.4622	0.0138	0.0035
303	D159_C	Angle_between_D2-1D2-2_and_C1-1C1-2	-2.4622	0.0138	0.0035
304	DCV134_C	CV_of_Distance_between_two_nuclear_brightest_points_through_middle_point_of_neck	2.4622	0.0138	0.0035
305	A122_A	Number_of_bright_actin_patches	-2.4149	0.0157	0.0039
306	D129_A1B	Distance_between_nuclear_brightest_point_and_mother_tip	2.4144	0.0158	0.0039
307	CCV110_A1B	CV_of_Distance_between_bud_tip_and_mother_long_axis_extension	2.4144	0.0158	0.0039
308	ACV101_A1B	CV_of_Actin_region_ratio_in_whole_cell	2.4144	0.0158	0.0039
309	DCV148_A1B	CV_of_Relative_distance_of_nuclear_brightest_point_to_mother_center	2.4144	0.0158	0.0039
310	A122_C	Number_of_bright_actin_patches	-2.4144	0.0158	0.0039
311	DCV148_C	CV_of_Relative_distance_of_nuclear_brightest_point_in_mother_to_mother_center	2.4144	0.0158	0.0039
312	C122	large_bud_ratio	-2.4144	0.0158	0.0039
313	CCV118_A1B	CV_of_Cell_size_ratio	2.3666	0.0180	0.0044
314	C108_C	Short_axis_length_in_bud	2.3666	0.0180	0.0044
315	ACV123_C	CV_of_Ratio_of_actin_patches_to_actin_region	2.3666	0.0180	0.0044
316	DCV139_C	CV_of_Distance_between_nuclear_brightest_point_in_bud_and_bud_tip	2.3666	0.0180	0.0044
317	D202	nuclear_C_ratio	2.3666	0.0180	0.0044
318	A101_A1B	Actin_region_ratio_in_whole_cell	-2.3187	0.0204	0.0049
319	D107_A1B	Ratio_of_D104_to_C103	-2.3187	0.0204	0.0049
320	CCV105_A1B	CV_of_Neck_position	2.3187	0.0204	0.0049
321	C113_C	Distance_between_bud_tip_and_mother_long_axis_through_middle_point_of_neck	2.3187	0.0204	0.0049
322	C126_C	Brightness_difference_of_cell_wall	-2.3187	0.0204	0.0049
323	D152_C	Mobility_of_nucleus_in_mother	-2.3187	0.0204	0.0049
324	C103_A	Long_axis_length_in_whole_cell	2.2709	0.0232	0.0055
325	D154_A	Angle_between_C1D1-1_and_C1C1-2	-2.2709	0.0232	0.0055

326	D135_A	Distance_between_nuclear_brightest_point_and_cell_center	2.2231	0.0262	0.0061
327	D155_A	Angle_between_C1D2-1_and_C1C1-2	-2.2231	0.0262	0.0061
328	C108_A1B	Short_axis_length_in_bud	-2.2231	0.0262	0.0061
329	D146_C	Distance_between_nuclear_outline_point_D8_in_bud_and_bud_tip	2.2231	0.0262	0.0061
330	CCV109_C	CV_of_Neck_width	2.2231	0.0262	0.0061
331	DCV154_C	CV_of_Angle_between_C1D1-1_and_C1C1-2	2.2231	0.0262	0.0061
332	A107_A1B	Actin_c_api_ratio	2.1773	0.0295	0.0068
333	DCV154_A	CV_of_Angle_between_C1D1-1_and_C1C1-2	2.1753	0.0296	0.0068
334	A101_C	Actin_region_ratio_in_whole_cell	-2.1753	0.0296	0.0068
335	DCV166_C	CV_of_Angle_between_D1-1D1-2_and_C4-1C4-2	2.1753	0.0296	0.0068
336	DCV188_C	CV_of_Distance_between_nuclear_gravity_center_and_brightest_point_in_mother	2.1753	0.0296	0.0068
337	D127_A	Distance_between_nuclear_brightest_point_and_cell_tip	2.1275	0.0334	0.0075
338	D104_A1B	Distance_between_nuclear_gravity_center_and_mother_tip	2.1275	0.0334	0.0075
339	DCV114_A1B	CV_of_Ratio_of_D110_to_C128	2.1275	0.0334	0.0075
340	D147_C	Relative_distance_of_nuclear_gravity_center_in_mother_to_mother_center	-2.1275	0.0334	0.0075
341	D191_C	Average_of_nuclear_brightness_in_mother	-2.1275	0.0334	0.0075
342	A107	actin_c_api_ratio	-2.1275	0.0334	0.0075
343	A119	actin_f_ratio_to_budded_cells	2.1275	0.0334	0.0075

Table S1F. List of parameters significantly affected by micafungin

Rank	ID	Description	Z value	P value	Q value
1	A7-1_A	Size_of_actin_region	6.4187	1.37E-10	6.90E-09
2	CCV104_A	CV_of_Short_axis_length_in_whole_cell	6.4187	1.37E-10	6.90E-09
3	CCV12-1_A	CV_of_Whole_cell_outline_length	6.3824	1.74E-10	6.90E-09
4	A106_A	Actin_b_ratio	-6.3652	1.95E-10	6.90E-09
5	A101_A	Actin_region_ratio_in_whole_cell	6.3099	2.79E-10	6.90E-09
6	CCV103_A	CV_of_Long_axis_length_in_whole_cell	6.3099	2.79E-10	6.90E-09
7	CCV11-1_A	CV_of_Whole_cell_size	6.2737	3.53E-10	6.90E-09
8	A115	actin_b_ratio_to_no_bud_cells	-6.2573	3.92E-10	6.90E-09
9	A105_A	Actin_a_ratio	6.2374	4.45E-10	6.90E-09
10	A111	actin_ae_ratio	6.2374	4.45E-10	6.90E-09
11	DCV102_A	CV_of_Distance_between_nuclear_gravity_center_and_mother_tip	6.1649	7.05E-10	9.94E-09
12	CCV128_A1B	CV_of_Distance_between_middle_point_of_neck_and_mother_hip	6.0923	1.11E-09	1.33E-08
13	A114	actin_a_ratio_to_no_bud_cells	6.0923	1.11E-09	1.33E-08
14	C124_C	Medium_bud_ratio	5.9504	2.67E-09	2.64E-08
15	C125_C	Large_bud_ratio	-5.9504	2.67E-09	2.64E-08
16	CCV112_A1B	CV_of_Distance_between_middle_point_of_neck_and_mother_center	5.9473	2.73E-09	2.64E-08
17	A105	actin_a_ratio	5.9300	3.03E-09	2.76E-08
18	C115_C	Mother_axis_ratio	-5.8385	5.27E-09	4.54E-08
19	ACV8-1_A	CV_of_Actin_region_brightness	5.8022	6.54E-09	5.07E-08
20	A112	actin_bcd_ratio	-5.8022	6.54E-09	5.07E-08
21	DCV127_A	CV_of_Distance_between_nuclear_brightest_point_and_cell_tip	5.7297	1.01E-08	7.43E-08
22	DCV14-1_A	CV_of_Nuclear_size	5.6934	1.25E-08	8.04E-08
23	C117_C	Cell_outline_ratio	-5.6934	1.25E-08	8.04E-08
24	C118_C	Cell_size_ratio	-5.6934	1.25E-08	8.04E-08
25	C115_A	Whole_cell_axis_ratio	-5.6572	1.54E-08	9.17E-08
26	DCV104_A1B	CV_of_Distance_between_nuclear_gravity_center_and_mother_tip	5.6572	1.54E-08	9.17E-08
27	DCV126_A1B	CV_of_Distance_between_nuclear_gravity_center_and_mother_hip	5.6209	1.90E-08	1.05E-07
28	CCV128_C	CV_of_Distance_between_middle_point_of_neck_and_mother_hip	5.6209	1.90E-08	1.05E-07
29	ACV123_A	CV_of_Ratio_of_actin_patches_t	5.5846	2.34E-08	1.25E-07

		o_actin_region			
30	A7-2_A1B	Size_of_actin_region_in_bud	-5.5121	3.55E-08	1.83E-07
31	C122	large_bud_ratio	-5.4758	4.35E-08	2.18E-07
32	A108	actin_d_iso_ratio	-5.4396	5.34E-08	2.59E-07
33	CCV12-1_A1B	CV_of_Mother_cell_outline_length	5.4033	6.54E-08	2.74E-07
34	CCV104_A1B	CV_of_Short_axis_length_in_mother	5.4033	6.54E-08	2.74E-07
35	ACV102_A1B	CV_of_Bud_actin_region_ratio_to_total_region	5.4033	6.54E-08	2.74E-07
36	CCV11-1_C	CV_of_Mother_cell_size	5.4033	6.54E-08	2.74E-07
37	CCV112_C	CV_of_Distance_between_middle_point_of_neck_and_mother_center	5.4033	6.54E-08	2.74E-07
38	C115_A1B	Mother_axis_ratio	-5.3671	8.00E-08	3.26E-07
39	CCV104_C	CV_of_Short_axis_length_in_mother	5.3308	9.78E-08	3.89E-07
40	C104_C	Short_axis_length_in_mother	5.2945	1.19E-07	4.62E-07
41	DCV179_A	CV_of_Nuclear_minimum_radius	5.2583	1.45E-07	5.50E-07
42	A7-1_A1B	Size_of_actin_region_in_mother	5.2220	1.77E-07	6.38E-07
43	DCV145_A1B	CV_of_Distance_between_nuclear_outline_point_D7_and_mother_hip	5.2220	1.77E-07	6.38E-07
44	CCV101_C	CV_of_Whole_cell_size	5.1857	2.15E-07	7.58E-07
45	C118_A1B	Cell_size_ratio	-5.1495	2.61E-07	8.44E-07
46	A103_A1B	Relative_distance_of_actin_patch_center_from_neck_in_mother	5.1495	2.61E-07	8.44E-07
47	CCV11-1_A1B	CV_of_Mother_cell_size	5.1495	2.61E-07	8.44E-07
48	CCV111_A1B	CV_of_Distance_between_bud_tip_and_mother_short_axis_extension	5.1495	2.61E-07	8.44E-07
49	C125	large_bud_ratio_to_buded_cells	-5.0777	3.82E-07	1.19E-06
50	A117	actin_d_iso_ratio_to_budded_cells	-5.0769	3.84E-07	1.19E-06
51	CCV106_A1B	CV_of_Bud_direction	5.0407	4.64E-07	1.38E-06
52	A118	actin_e_ratio_to_budded_cells	5.0407	4.64E-07	1.38E-06
53	C124_A1B	Medium_bud_ratio	-5.0252	5.03E-07	1.47E-06
54	C104_A1B	Short_axis_length_in_mother	5.0044	5.60E-07	1.61E-06
55	C123_A1B	Small_bud_ratio	4.9877	6.11E-07	1.72E-06
56	A8-1_A1B	Total_brightness_of_actin_region_in_mother	4.9682	6.76E-07	1.84E-06
57	D132_A1B	Distance_between_nuclear_brightest_point_and_middle_point_of_neck	4.9682	6.76E-07	1.84E-06
58	DCV176_A	CV_of_Nuclear_long_axis_length	4.8956	9.80E-07	2.49E-06
59	C117_A1B	Cell_outline_ratio	-4.8956	9.80E-07	2.49E-06
60	ACV8-2_A1B	CV_of_Total_brightness_of_actin_region_in_bud	4.8956	9.80E-07	2.49E-06
61	CCV12-1_C	CV_of_Mother_cell_outline_length	4.8956	9.80E-07	2.49E-06

62	A108_A1B	Actin_d_iso_ratio	-4.8782	1.07E-06	2.68E-06
63	CCV103_A1B	CV_of_Long_axis_length_in_mother	4.8594	1.18E-06	2.90E-06
64	A109_A1B	Actin_e_ratio	4.7868	1.69E-06	3.86E-06
65	CCV13_A1B	CV_of_Mother_cell_fitness_for_ellipse	4.7868	1.69E-06	3.86E-06
66	A8-1_C	Total_brightness_of_actin_region_in_mother	4.7868	1.69E-06	3.86E-06
67	A9_C	Proportion_of_actin_region_at_neck	-4.7868	1.69E-06	3.86E-06
68	DCV185_C	CV_of_Total_length_of_two_straight_segments_D11-1C4-1_and_D11-2C4-1	4.7868	1.69E-06	3.86E-06
69	ACV9_C	CV_of_Proportion_of_actin_region_at_neck	4.7506	2.03E-06	4.56E-06
70	A8-1_A	Actin_region_brightness	4.7143	2.43E-06	5.08E-06
71	DCV15-1_A	CV_of_Nuclear_brightness	4.7143	2.43E-06	5.08E-06
72	DCV173_A	CV_of_Maximal_distance_between_nuclear_gravity_center_and_nuclear_outline	4.7143	2.43E-06	5.08E-06
73	CCV105_A1B	CV_of_Neck_position	4.7143	2.43E-06	5.08E-06
74	ACV9_A1B	CV_of_Proportion_of_actin_region_at_neck	4.7143	2.43E-06	5.08E-06
75	CCV13_A	CV_of_Whole_cell_fitness_for_ellipse	4.6780	2.90E-06	5.76E-06
76	A102_A1B	Bud_actin_region_ratio_to_total_region	-4.6780	2.90E-06	5.76E-06
77	C11-1_C	Mother_cell_size	4.6780	2.90E-06	5.76E-06
78	DCV186_C	CV_of_Total_length_of_two_straight_segments_D12-1C4-1_and_D12-2C4-1	4.6780	2.90E-06	5.76E-06
79	C11-2_A1B	Bud_cell_size	-4.6418	3.45E-06	6.61E-06
80	C116_C	Axis_ratio_ratio	4.6418	3.45E-06	6.61E-06
81	CCV117_C	CV_of_Cell_outline_ratio	4.6418	3.45E-06	6.61E-06
82	CCV101_A1B	CV_of_Whole_cell_size	4.6055	4.11E-06	7.59E-06
83	ACV7-1_A1B	CV_of_Size_of_actin_region_in_mother	4.6055	4.11E-06	7.59E-06
84	CCV11-2_C	CV_of_Bud_cell_size	4.6055	4.11E-06	7.59E-06
85	C12-1_C	Mother_cell_outline_length	4.5692	4.89E-06	8.62E-06
86	C112_C	Distance_between_middle_point_of_neck_and_mother_center	4.5692	4.89E-06	8.62E-06
87	A7-1_C	Size_of_actin_region_in_mother	4.5692	4.89E-06	8.62E-06
88	CCV113_C	CV_of_Distance_between_bud_tip_and_mother_long_axis_through_middle_point_of_neck	4.5692	4.89E-06	8.62E-06
89	C128_C	Distance_between_middle_point_of_neck_and_mother_hip	4.5330	5.82E-06	9.80E-06
90	CCV103_C	CV_of_Long_axis_length_in_mother	4.5330	5.82E-06	9.80E-06
91	CCV108_C	CV_of_Short_axis_length_in_bud	4.5330	5.82E-06	9.80E-06
92	DCV14-3_C	CV_of_Nuclear_size_in_whole_c	4.5330	5.82E-06	9.80E-06

		ell			
93	CCV118_C	CV_of_Cell_size_ratio	4.4605	8.18E-06	1.35E-05
94	ACV7-1_C	CV_of_Size_of_actin_region_in_mother	4.4605	8.18E-06	1.35E-05
95	C107_A1B	Long_axis_length_in_bud	-4.3879	1.14E-05	1.85E-05
96	CCV107_C	CV_of_Long_axis_length_in_bud	4.3879	1.14E-05	1.85E-05
97	CCV110_A1B	CV_of_Distance_between_bud_tip_and_mother_long_axis_extension	4.3517	1.35E-05	2.14E-05
98	DCV14-3_A1B	CV_of_Nuclear_size	4.3517	1.35E-05	2.14E-05
99	CCV109_A1B	CV_of_Neck_width	4.2429	2.21E-05	3.46E-05
100	D110_A1B	Distance_between_nuclear_gravity_center_and_middle_point_of_neck	4.2066	2.59E-05	3.98E-05
101	DCV15-1_C	CV_of_Nuclear_brightness_in_mother	4.2066	2.59E-05	3.98E-05
102	DCV105_A	CV_of_Ratio_of_D102_to_C103	4.1703	3.04E-05	4.49E-05
103	DCV129_A1B	CV_of_Distance_between_nuclear_brightest_point_and_mother_tip	4.1703	3.04E-05	4.49E-05
104	DCV179_C	CV_of_Nuclear_minimum_radius_in_mother	4.1703	3.04E-05	4.49E-05
105	A109	actin_e_ratio	4.1703	3.04E-05	4.49E-05
106	C12-2_A1B	Bud_cell_outline_length	-4.1341	3.56E-05	5.02E-05
107	ACV8-1_A1B	CV_of_Total_brightness_of_actin_region_in_mother	4.1341	3.56E-05	5.02E-05
108	CCV13_C	CV_of_Mother_cell_fitness_for_ellipse	4.1341	3.56E-05	5.02E-05
109	CCV102_C	CV_of_Whole_cell_outline_length	4.1341	3.56E-05	5.02E-05
110	CCV106_C	CV_of_Bud_direction	4.1341	3.56E-05	5.02E-05
111	A106	actin_b_ratio	-4.0978	4.17E-05	5.82E-05
112	DCV181_A1B	CV_of_Nuclear_minimum_radius	4.0616	4.87E-05	6.69E-05
113	C123	small_bud_ratio_to_budded_cells	4.0616	4.87E-05	6.69E-05
114	A112_A1B	Actin_cd_ratio	-4.0440	5.25E-05	7.14E-05
115	CCV12-2_C	CV_of_Bud_cell_outline_length	4.0253	5.69E-05	7.47E-05
116	CCV105_C	CV_of_Neck_position	4.0253	5.69E-05	7.47E-05
117	ACV8-1_C	CV_of_Total_brightness_of_actin_region_in_mother	4.0253	5.69E-05	7.47E-05
118	DCV159_C	CV_of_Angle_between_D2-1D2-2_and_C1-1C1-2	4.0253	5.69E-05	7.47E-05
119	CCV115_A	CV_of_Whole_cell_axis_ratio	3.9890	6.63E-05	8.57E-05
120	CCV110_C	CV_of_Distance_between_bud_tip_and_mother_long_axis_extension	3.9890	6.63E-05	8.57E-05
121	C11-1_A1B	Mother_cell_size	3.9528	7.73E-05	9.82E-05
122	DCV158_C	CV_of_Angle_between_D1-1D1-2_and_C1-1C1-2	3.9528	7.73E-05	9.82E-05
123	D200	nuclear_A1_ratio	-3.9165	8.98E-05	1.13E-04
124	DCV117_A	CV_of_Distance_between_nuclear_gravity_center_and_cell_center	3.8077	1.40E-04	1.75E-04
125	C119	no_bud_ratio	3.7714	1.62E-04	2.01E-04

126	A104_C	Relative_distance_of_actin_patch_center_from_neck_in_bud	-3.7352	1.88E-04	2.31E-04
127	ACV123_A1B	CV_of_Ratio_of_actin_patches_to_actin_region	3.6989	2.17E-04	2.62E-04
128	DCV15-3_C	CV_of_Nuclear_brightness_in_whole_cell	3.6989	2.17E-04	2.62E-04
129	C125_A1B	Large_bud_ratio	-3.6329	2.80E-04	3.35E-04
130	A9_A1B	Proportion_of_actin_region_at_neck	-3.6264	2.87E-04	3.35E-04
131	ACV7-2_C	CV_of_Size_of_actin_region_in_bud	-3.6264	2.87E-04	3.35E-04
132	DCV103_C	CV_of_Distance_between_nuclear_gravity_center_in_mother_and_mother_tip	3.6264	2.87E-04	3.35E-04
133	D210	nuclear_A_ratio_to_nuclear_AA1BC_cells	3.6264	2.87E-04	3.35E-04
134	C12-1_A1B	Mother_cell_outline_length	3.5901	3.31E-04	3.77E-04
135	C106_C	Bud_direction	-3.5901	3.31E-04	3.77E-04
136	D144_C	Distance_between_nuclear_outline_point_D6-2_in_bud_&_middle_point_of_neck	-3.5901	3.31E-04	3.77E-04
137	C110_A1B	Distance_between_bud_tip_and_mother_long_axis_extension	-3.5539	3.80E-04	4.20E-04
138	DCV14-1_C	CV_of_Nuclear_size_in_mother	3.5539	3.80E-04	4.20E-04
139	DCV194_C	CV_of_Maximal_intensity_of_nuclear_brightness_divided_by_average_in_mother	3.5539	3.80E-04	4.20E-04
140	D211	nuclear_A1_ratio_to_nuclear_AA1BC_cells	-3.5539	3.80E-04	4.20E-04
141	D203	nuclear_D_ratio	3.5350	4.08E-04	4.48E-04
142	D109_C	Distance_between_nuclear_gravity_center_in_bud_and_middle_point_of_neck	-3.5176	4.35E-04	4.75E-04
143	D105_A	Ratio_of_D102_to_C103	3.4813	4.99E-04	5.33E-04
144	A123_A1B	Ratio_of_actin_patches_to_actin_region	3.4813	4.99E-04	5.33E-04
145	D15-3_A1B	Nuclear_brightness	3.4813	4.99E-04	5.33E-04
146	C127_A1B	Thickness_difference_of_cell_wall	3.4451	5.71E-04	6.06E-04
147	DCV196_C	CV_of_Maximal_intensity_of_nuclear_brightness_divided_by_average_in_whole cell	3.4088	6.52E-04	6.83E-04
148	C124	medium_bud_ratio_to_buded_cells	3.4088	6.52E-04	6.83E-04
149	ACV122_A	CV_of_Number_of_bright_actin_patches	3.3725	7.45E-04	7.59E-04
150	DCV107_A1B	CV_of_Ratio_of_D104_to_C103	3.3725	7.45E-04	7.59E-04
151	D143_C	Distance_between_nuclear_outline_point_D6-1_in_mother_and_middle_point_of_neck	3.3725	7.45E-04	7.59E-04
152	DCV125_C	CV_of_Distance_between_nuclea	3.3725	7.45E-04	7.59E-04

		r_gravity_center_in_mother_and_mother_hip			
153	A107_C	Actin_c_api_ratio	-3.3196	9.02E-04	9.13E-04
154	C123_C	Small_bud_ratio	3.3081	9.39E-04	9.46E-04
155	D193_A1B	Average_of_nuclear_brightness	3.3000	9.67E-04	9.61E-04
156	DCV142_A1B	CV_of_Distance_between_nuclear_brightest_point_and_mother_hip	3.3000	9.67E-04	9.61E-04
157	D204	nuclear_E_ratio	3.2778	0.0010	0.0010
158	CCV126_A	CV_of_Brightness_difference_of_cell_wall	3.2637	0.0011	0.0011
159	DCV135_A	CV_of_Distance_between_nuclear_brightest_point_and_cell_center	3.2637	0.0011	0.0011
160	D131_C	Distance_between_nuclear_brightest_point_in_bud_and_middle_point_of_neck	-3.2637	0.0011	0.0011
161	A102_C	Bud_actin_region_ratio_to_total_region	-3.2275	0.0012	0.0012
162	D151_C	Ratio_of_distance_between_each_nucleus_and_middle_point_of_neck	-3.2275	0.0012	0.0012
163	CCV116_A1B	CV_of_Axis_ratio_ratio	3.1912	0.0014	0.0013
164	A121_C	Maximal_distance_between_patches	3.1912	0.0014	0.0013
165	DCV128_C	CV_of_Distance_between_nuclear_brightest_point_in_mother_and_mother_tip	3.1912	0.0014	0.0013
166	D135_A	Distance_between_nuclear_brightest_point_and_cell_center	3.1550	0.0016	0.0015
167	D16-3_A1B	Maximal_intensity_of_nuclear_brightness	3.1550	0.0016	0.0015
168	DCV196_A1B	CV_of_Maximal_intensity_of_nuclear_brightness_divided_by_average	3.1550	0.0016	0.0015
169	ACV7-1_A	CV_of_Size_of_actin_region	3.1187	0.0018	0.0016
170	C110_C	Distance_between_bud_tip_and_mother_long_axis_extension	-3.1187	0.0018	0.0016
171	DCV14-2_C	CV_of_Nuclear_size_in_bud	3.1187	0.0018	0.0016
172	DCV141_C	CV_of_Distance_between_nuclear_brightest_point_in_mother_and_mother_hip	3.1187	0.0018	0.0016
173	D117_A	Distance_between_nuclear_gravity_center_and_cell_center	3.0824	0.0021	0.0018
174	D191_A	Average_of_nuclear_brightness	3.0824	0.0021	0.0018
175	C101_C	Whole_cell_size	3.0824	0.0021	0.0018
176	C13_A1B	Mother_cell_fitness_for_ellipse	3.0466	0.0023	0.0020
177	C106_A1B	Bud_direction	-3.0462	0.0023	0.0020
178	C112_A1B	Distance_between_middle_point_of_neck_and_mother_center	3.0462	0.0023	0.0020
179	D154_A1B	Angle_between_C1D1-1_and_C1C1-2	3.0462	0.0023	0.0020
180	A120_C	Total_length_of_actin_patch_link	3.0462	0.0023	0.0020

181	D14-1_A	Nuclear_size	3.0099	0.0026	0.0022
182	A107_A1B	Actin_c_api_ratio	2.9922	0.0028	0.0024
183	D15-1_A	Nuclear_brightness	2.9736	0.0029	0.0024
184	D16-1_A	Maximal_intensity_of_nuclear_brightness	2.9736	0.0029	0.0024
185	D155_A	Angle_between_C1D2-1_and_C1C1-2	-2.9736	0.0029	0.0024
186	CCV114_A1B	CV_of_Bud_axis_ratio	2.9736	0.0029	0.0024
187	DCV110_A1B	CV_of_Distance_between_nuclear_gravity_center_and_middle_point_of_neck	2.9736	0.0029	0.0024
188	D114_A1B	Ratio_of_D110_to_C128	2.9374	0.0033	0.0027
189	DCV130_C	CV_of_Distance_between_nuclear_brightest_point_in_mother_and_middle_point_of_neck	2.9374	0.0033	0.0027
190	C128_A1B	Distance_between_middle_point_of_neck_and_mother_hip	2.9011	0.0037	0.0030
191	D152_A1B	Mobility_of_nucleus_in_mother	2.9011	0.0037	0.0030
192	D117_C	Distance_between_nuclear_gravity_center_in_mother_and_mother_center	2.9011	0.0037	0.0030
193	DCV177_C	CV_of_Nuclear_long_axis_length_in_bud	2.9011	0.0037	0.0030
194	A120_A1B	Total_length_of_actin_patch_link	2.8648	0.0042	0.0033
195	A121_A1B	Maximal_distance_between_patches	2.8648	0.0042	0.0033
196	CCV115_A1B	CV_of_Mother_axis_ratio	2.8648	0.0042	0.0033
197	A120_A	Total_length_of_actin_patch_link	2.8286	0.0047	0.0037
198	D147_A	Relative_distance_of_nuclear_gravity_center_to_cell_center	2.7923	0.0052	0.0041
199	DCV194_A	CV_of_Maximal_intensity_of_nuclear_brightness_divided_by_average	2.7561	0.0059	0.0045
200	A123_C	Ratio_of_actin_patches_to_actin_region	2.7561	0.0059	0.0045
201	D155_C	Angle_between_C1D2-1_and_C1C1-2	-2.7561	0.0059	0.0045
202	D157_C	Angle_between_C2D2-2_and_C2C4-2	2.7561	0.0059	0.0045
203	D207	nuclear_A1_ratio_to_budded_cells	-2.7561	0.0059	0.0045
204	D143_A1B	Distance_between_nuclear_outline_point_D6-1_and_middle_point_of_neck	2.7198	0.0065	0.0049
205	CCV126_A1B	CV_of_Brightness_difference_of_cell_wall	2.7198	0.0065	0.0049
206	DCV118_A1B	CV_of_Distance_between_nuclear_gravity_center_and_mother_center	2.7198	0.0065	0.0049
207	D108_C	Distance_between_nuclear_gravity_center_in_mother_and_middle_point_of_neck	2.7198	0.0065	0.0049
208	D206	nuclear_A_ratio_to_no_bud_cells	-2.6903	0.0071	0.0053

209	C116_A1B	Axis_ratio_ratio	2.6835	0.0073	0.0053
210	ACV101_A1B	CV_of_Actin_region_ratio_in_whole_cell	2.6835	0.0073	0.0053
211	C103_C	Long_axis_length_in_mother	2.6835	0.0073	0.0053
212	DCV155_C	CV_of_Angle_between_C1D2-1_and_C1C1-2	2.6835	0.0073	0.0053
213	A112_C	Actin_cd_ratio	-2.6665	0.0077	0.0056
214	ACV103_A1B	CV_of_Relative_distance_of_actin_patch_center_from_neck_in_mother	2.6473	0.0081	0.0057
215	C109_C	Neck_width	2.6473	0.0081	0.0057
216	D15-2_C	Nuclear_brightness_in_bud	2.6473	0.0081	0.0057
217	D194_C	Maximal_intensity_of_nuclear_brightness_divided_by_average_in_mother	-2.6473	0.0081	0.0057
218	D198_C	Ratio_of_nuclear_brightness	2.6473	0.0081	0.0057
219	CCV111_C	CV_of_Distance_between_bud_tip_and_mother_short_axis_extension	2.6473	0.0081	0.0057
220	C101_A1B	Whole_cell_size	2.6110	0.0090	0.0063
221	D199	nuclear_A_ratio	2.6110	0.0090	0.0063
222	D176_A	Nuclear_long_axis_length	2.5747	0.0100	0.0070
223	D135_C	Distance_between_nuclear_brightest_point_in_mother_and_mother_center	2.5385	0.0111	0.0077
224	DCV155_A	CV_of_Angle_between_C1D2-1_and_C1C1-2	2.5022	0.0123	0.0085
225	D123_C	Ratio_of_D121_to_C107	2.5022	0.0123	0.0085
226	A113_A1B	Actin_n_ratio	2.4952	0.0126	0.0086
227	CCV113_A1B	CV_of_Distance_between_bud_tip_and_mother_long_axis_through_middle_point_of_neck	2.4659	0.0137	0.0093
228	DCV188_C	CV_of_Distance_between_nuclear_gravity_center_and_brightest_point_in_mother	2.4659	0.0137	0.0093
229	D170_A1B	Angle_between_C4-1D2-1_and_C4-1C1	2.4297	0.0151	0.0101
230	D159_C	Angle_between_D2-1D2-2_and_C1-1C1-2	-2.4297	0.0151	0.0101
231	ACV102_C	CV_of_Bud_actin_region_ratio_to_total_region	2.4297	0.0151	0.0101
232	C109_A1B	Neck_width	2.3934	0.0167	0.0112
233	A110_A1B	Actin_f_ratio	-2.3790	0.0174	0.0115
234	D118_A1B	Distance_between_nuclear_gravity_center_and_mother_center	2.3572	0.0184	0.0120
235	CCV102_A1B	CV_of_Whole_cell_outline_length	2.3572	0.0184	0.0120
236	D153_C	Mobility_of_nucleus_in_bud	-2.3572	0.0184	0.0120
237	DCV106_C	CV_of_Ratio_of_D103_to_C103	2.3572	0.0184	0.0120
238	DCV137_C	CV_of_Distance_between_nuclear_brightest_point_in_bud_and_bud_center	2.3572	0.0184	0.0120

239	ACV120_A1B	CV_of_Total_length_of_actin_patch_link	2.3209	0.0203	0.0130
240	C111_C	Distance_between_bud_tip_and_mother_short_axis_extension	2.3209	0.0203	0.0130
241	D14-1_C	Nuclear_size_in_mother	2.3209	0.0203	0.0130
242	D113_C	Ratio_of_D109_to_C107	-2.3209	0.0203	0.0130
243	D205	nuclear_F_ratio	2.3179	0.0205	0.0130
244	C104_A	Short_axis_length_in_whole_cell	2.2846	0.0223	0.0139
245	D148_A	Relative_distance_of_nuclear_brightest_point_to_cell_center	2.2846	0.0223	0.0139
246	D185_C	Total_length_of_two_straight_segments_D11-1C4-1_and_D11-2C4-1	2.2846	0.0223	0.0139
247	D186_C	Total_length_of_two_straight_segments_D12-1C4-1_and_D12-2C4-1	2.2846	0.0223	0.0139
248	DCV108_C	CV_of_Distance_between_nuclear_gravity_center_in_mother_and_middle_point_of_neck	2.2846	0.0223	0.0139
249	DCV174_C	CV_of_Maximal_distance_between_nuclear_gravity_center_and_nuclear_outline_in_bud	2.2846	0.0223	0.0139
250	D173_A	Maximal_distance_between_nuclear_gravity_center_and_nuclear_outline	2.2484	0.0246	0.0152
251	D158_C	Angle_between_D1-1D1-2_and_C1-1C1-2	-2.2484	0.0246	0.0152

Table S2A. Parameters that describe major alteration induced by terbinafine treatment

PC	ID	Description	Loadings	P value
PC1*	D14-3_A1B	Nuclear_size	0.780	3.42E-26
	C104_C	Short_axis_length_in_mother	0.779	4.25E-26
	D14-2_C	Nuclear_size_in_bud	0.774	1.58E-25
	C101_C	Whole_cell_size	0.767	7.54E-25
	C11-1_C	Mother_cell_size	0.765	1.21E-24
	C104_A1B	Short_axis_length_in_mother	0.754	1.27E-23
	C128_A1B	Distance_between_middle_point_of_neck_and_mother_hip	0.751	2.28E-23
	C11-1_A1B	Mother_cell_size	0.751	2.33E-23
	D14-3_C	Nuclear_size_in_whole_cell	0.745	7.05E-23
	D180_C	Nuclear_minimum_radius_in_bud	0.746	1.01E-22
	D177_C	Nuclear_long_axis_length_in_bud	0.738	3.32E-22
	D174_C	Maximal_distance_between_nuclear_gravity_center_and_nuclear_outline_in_bud	0.699	3.66E-19
	D176_A	Nuclear_long_axis_length	0.695	6.64E-19
	D178_A1B	Nuclear_long_axis_length	0.683	4.63E-18
	D173_A	Maximal_distance_between_nuclear_gravity_center_and_nuclear_outline	0.679	8.76E-18
	D14-1_A	Nuclear_size	0.673	1.93E-17
	D179_A	Nuclear_minimum_radius	0.672	2.24E-17
	C112_A1B	Distance_between_middle_point_of_neck_and_mother_center	0.671	2.97E-17
	D175_A1B	Maximal_distance_between_nuclear_gravity_center_and_nuclear_outline	0.668	4.26E-17
	C108_C	Short_axis_length_in_bud	0.608	1.15E-13
	C13_A1B	Mother_cell_fitness_for_ellipse	-0.591	7.72E-13
	C115_C	Mother_axis_ratio	-0.566	1.14E-11
	C109_A1B	Neck_width	0.551	4.98E-11
	C109_C	Neck_width	0.541	1.23E-10
	C115_A1B	Mother_axis_ratio	-0.519	8.58E-10
	C104_A	Short_axis_length_in_whole_cell	0.517	1.10E-09
	D188_A	Distance_between_nuclear_gravity_center_and_brightest_point	0.502	3.90E-09
	C13_C	Mother_cell_fitness_for_ellipse	-0.506	4.30E-09
PC2*	DCV176_A	CV_of_Nuclear_long_axis_length	0.697	4.67E-19
	DCV173_A	CV_of_Maximal_distance_between_nuclear_gravity_center_and_nuclear_outline	0.673	2.17E-17
	DCV14-1_A	CV_of_Nuclear_size	0.659	1.67E-16
	D14-1_A	Nuclear_size	0.647	8.67E-16
	D173_A	Maximal_distance_between_nuclear_gravity_center_and_nuclear_ou	0.631	6.34E-15

		tline		
	D176_A	Nuclear_long_axis_length	0.622	2.16E-14
	D179_A	Nuclear_minimum_radius	0.585	1.51E-12
	C104_A1B	Short_axis_length_in_mother	-0.553	3.97E-11
	C112_A1B	Distance_between_middle_point_of_neck_and_mother_center	-0.552	4.47E-11
	C11-1_A1B	Mother_cell_size	-0.534	2.39E-10
	D14-3_C	Nuclear_size_in_whole_cell	0.516	1.16E-09
	DCV17-1_A	CV_of_Nuclear_fitness_for_ellipse	0.515	1.26E-09
	D174_C	Maximal_distance_between_nuclear_gravity_center_and_nuclear_outline_in_bud	0.514	1.43E-09
	C104_C	Short_axis_length_in_mother	-0.510	1.90E-09
PC3*	D15-3_A1B	Nuclear_brightness	0.629	8.12E-15
	D15-1_A	Nuclear_brightness	0.616	4.40E-14
	D15-3_C	Nuclear_brightness_in_whole_cell	0.611	7.99E-14
	C106_C	Bud_direction	-0.556	3.08E-11
	CCV110_C	CV_of_Distance_between_bud_tip_and_mother_long_axis_extension	0.521	7.82E-10
	CCV106_C	CV_of_Bud_direction	0.513	1.51E-09
PC4*	D15-3_A1B	Nuclear_brightness	0.583	1.80E-12
	D15-3_C	Nuclear_brightness_in_whole_cell	0.574	4.82E-12
	CCV110_A1B	CV_of_Distance_between_bud_tip_and_mother_long_axis_extension	-0.569	7.69E-12
	D15-1_A	Nuclear_brightness	0.564	1.40E-11
	CCV106_A1B	CV_of_Bud_direction	-0.559	2.22E-11
PC5*	D156_C	Angle_between_C2D1-2_and_C2C4-2	-0.838	2.10E-33
	D157_C	Angle_between_C2D2-2_and_C2C4-2	-0.751	2.16E-23
	DCV123_C	CV_of_Ratio_of_D121_to_C107	0.726	3.06E-21

*Principal component 1, 2, 3, 4, and 5, respectively.

Table S2B. Parameters that describe major alteration induced by flucytosine treatment

PC	ID	Description	Loadings	P value
PC1*	A106_A	Actin_b_ratio	0.972	2.38E-77
	A105_A	Actin_a_ratio	-0.971	9.61E-77
	A115	actin_b_ratio_to_no_bud_cells	0.971	2.11E-76
	A101_A	Actin_region_ratio_in_whole_cell	-0.970	7.26E-76
	A114	actin_a_ratio_to_no_bud_cells	-0.970	1.28E-75
	A7-1_A	Size_of_actin_region	-0.940	6.00E-58
	A111	actin_ae_ratio	-0.929	5.65E-54
	A112	actin_bcd_ratio	0.910	8.47E-48
	ACV123_A	CV_of_Ratio_of_actin_patches_to_actin_region	-0.791	1.99E-27
	ACV7-1_A1B	CV_of_Size_of_actin_region_in_mother	-0.530	3.37E-10
PC2*	D128_C	Distance_between_nuclear_brightest_point_in_mother_and_mother_tip	-0.725	3.77E-21
	D103_C	Distance_between_nuclear_gravity_center_in_mother_and_mother_tip	-0.721	8.27E-21
	D135_A	Distance_between_nuclear_brightest_point_and_cell_center	-0.681	5.83E-18
	D141_C	Distance_between_nuclear_brightest_point_in_mother_and_mother_hip	-0.629	8.11E-15
	D106_C	Ratio_of_D103_to_C103	-0.568	8.95E-12
	D125_C	Distance_between_nuclear_gravity_center_in_mother_and_mother_hip	-0.565	1.28E-11
	C102_A1B	Whole_cell_outline_length	-0.559	2.25E-11
	D127_A	Distance_between_nuclear_brightest_point_and_cell_tip	-0.553	4.19E-11
	C113_A1B	Distance_between_bud_tip_and_mother_long_axis_through_middle_point_of_neck	-0.521	7.57E-10
	D170_A1B	Angle_between_C4-1D2-1_and_C4-1C1	-0.518	1.01E-09
	D105_A	Ratio_of_D102_to_C103	-0.509	2.17E-09
PC3*	D17-1_C	Nuclear_fitness_for_ellipse_in_mother	0.555	3.35E-11
	D141_C	Distance_between_nuclear_brightest_point_in_mother_and_mother_hip	-0.536	2.07E-10
	D128_C	Distance_between_nuclear_brightest_point_in_mother_and_mother_tip	-0.529	3.68E-10
	D103_C	Distance_between_nuclear_gravity_center_in_mother_and_mother_tip	-0.525	5.23E-10
	DCV173_C	CV_of_Maximal_distance_between_nuclear_gravity_center_and_nuclear_outline_in_mother	0.515	1.28E-09
	D125_C	Distance_between_nuclear_gravity_center_in_mother_and_mother_hip	-0.514	1.40E-09
	D106_C	Ratio_of_D103_to_C103	-0.506	2.78E-09
	DCV176_C	CV_of_Nuclear_long_axis_length_in_mother	0.504	3.38E-09
	C117_C	Cell_outline_ratio	-0.502	3.93E-09
PC4*	DCV173_C	CV_of_Maximal_distance_between_nuclear_gravity_center_and_nuclear_outline	0.625	1.43E-14

		_in_mother		
	DCV176_C	CV_of_Nuclear_long_axis_length_in_mother	0.565	1.17E-11
PC5*	D17-1_A	Nuclear_fitness_for_ellipse	-0.546	7.95E-11
	DCV17-1_A	CV_of_Nuclear_fitness_for_ellipse	-0.542	1.12E-10
	D182_A	Nuclear_axis_ratio	-0.511	1.79E-09
PC6*	C110_A1B	Distance_between_bud_tip_and_mother_long_axis_extension	-0.711	4.36E-20
	C105_A1B	Neck_position	-0.703	1.68E-19

*Principal component 1, 2, 3, 4, 5, and 6, respectively.

Table S2C. Parameters that describe major alteration induced by micafungin treatment

PC	ID	Description	Loadings	P value
PC1*	C112_A1B	Distance_between_middle_point_of_neck_and_mother_center	-0.840	1.15E-33
	C104_A1B	Short_axis_length_in_mother	-0.818	1.42E-30
	C12-1_A1B	Mother_cell_outline_length	-0.805	5.63E-29
	C11-1_A1B	Mother_cell_size	-0.802	1.36E-28
	C104_C	Short_axis_length_in_mother	-0.793	1.31E-27
	C112_C	Distance_between_middle_point_of_neck_and_mother_center	-0.788	5.27E-27
	C11-1_C	Mother_cell_size	-0.766	9.52E-25
	C12-1_C	Mother_cell_outline_length	-0.742	1.36E-22
	C101_C	Whole_cell_size	-0.738	2.95E-22
	C128_A1B	Distance_between_middle_point_of_neck_and_mother_hip	-0.726	3.38E-21
	D117_A	Distance_between_nuclear_gravity_center_and_cell_center	-0.714	2.81E-20
	D135_A	Distance_between_nuclear_brightest_point_and_cell_center	-0.694	8.02E-19
	C103_C	Long_axis_length_in_mother	-0.687	2.28E-18
	C101_A1B	Whole_cell_size	-0.681	5.71E-18
	A7-1_A1B	Size_of_actin_region_in_mother	0.677	1.06E-17
	C128_C	Distance_between_middle_point_of_neck_and_mother_hip	-0.671	2.64E-17
	D117_C	Distance_between_nuclear_gravity_center_in_mother_and_mother_center	-0.652	3.95E-16
	D186_C	Total_length_of_two_straight_segments_D12-1C4-1_and_D12-2C4-1	-0.652	4.14E-16
	D185_C	Total_length_of_two_straight_segments_D11-1C4-1_and_D11-2C4-1	-0.649	6.45E-16
	A109_A1B	Actin_e_ratio	0.634	4.47E-15
	A118	actin_e_ratio_to_budded_cells	0.633	4.95E-15
	D108_C	Distance_between_nuclear_gravity_center_in_mother_and_middle_point_of_neck	-0.629	7.96E-15
	C115_A1B	Mother_axis_ratio	0.623	1.75E-14
	A112_A1B	Actin_cd_ratio	-0.622	1.98E-14
	A102_A1B	Bud_actin_region_ratio_to_total_region	-0.614	5.63E-14
	A111	actin_ae_ratio	0.609	1.01E-13
	A112	actin_bcd_ratio	-0.608	1.06E-13
	D147_A	Relative_distance_of_nuclear_gravity_center_to_cell_center	-0.605	1.52E-13
	C104_A	Short_axis_length_in_whole_cell	-0.602	2.17E-13
	D148_A	Relative_distance_of_nuclear_brightest_point_to_cell_center	-0.597	4.04E-13
	C115_C	Mother_axis_ratio	0.590	8.27E-13
	A109	actin_e_ratio	0.580	2.53E-12
	A101_A	Actin_region_ratio_in_whole_cell	0.569	7.78E-12

	DCV14-1_A	CV_of_Nuclear_size	0.539	1.52E-10
	D105_A	Ratio_of_D102_to_C103	-0.539	1.58E-10
	C13_A1B	Mother_cell_fitness_for_ellipse	0.532	2.81E-10
	A7-1_C	Size_of_actin_region_in_mother	0.531	3.13E-10
	D143_C	Distance_between_nuclear_outline_point_D6-1_in_mother_and_middle_point_of_neck	-0.522	6.92E-10
	A8-1_A1B	Total_brightness_of_actin_region_in_mother	0.521	7.53E-10
PC2*	A123_C	Ratio_of_actin_patches_to_actin_region	0.848	7.31E-35
	A123_A1B	Ratio_of_actin_patches_to_actin_region	0.845	2.46E-34
	A120_A1B	Total_length_of_actin_patch_link	0.838	2.54E-33
	A121_A1B	Maximal_distance_between_patches	0.837	3.20E-33
	A121_C	Maximal_distance_between_patches	0.821	6.19E-31
	A120_C	Total_length_of_actin_patch_link	0.819	1.12E-30
	A120_A	Total_length_of_actin_patch_link	0.796	5.78E-28
	ACV120_A1B	CV_of_Total_length_of_actin_patch_link	-0.766	8.37E-25
	ACV122_A	CV_of_Number_of_bright_actin_patches	-0.703	1.67E-19
	ACV123_A	CV_of_Ratio_of_actin_patches_to_actin_region	-0.667	4.69E-17
	A105	actin_a_ratio	-0.661	1.20E-16
	ACV123_A1B	CV_of_Ratio_of_actin_patches_to_actin_region	-0.627	1.18E-14
	A115	actin_b_ratio_to_no_bud_cells	0.605	1.52E-13
	A114	actin_a_ratio_to_no_bud_cells	-0.604	1.80E-13
	A106_A	Actin_b_ratio	0.6034	1.90E-13
	A105_A	Actin_a_ratio	-0.593	6.01E-13
	A8-1_A1B	Total_brightness_of_actin_region_in_mother	0.589	8.90E-13
	A8-1_A	Actin_region_brightness	0.583	1.79E-12
	DCV15-1_A	CV_of_Nuclear_brightness	0.579	2.90E-12
	A111	actin_ae_ratio	-0.571	6.74E-12
	A112	actin_bcd_ratio	0.545	8.33E-11
	DCV15-3_C	CV_of_Nuclear_brightness_in_whole_cell	0.543	1.06E-10
	A101_A	Actin_region_ratio_in_whole_cell	-0.532	2.94E-10
	D15-3_A1B	Nuclear_brightness	-0.531	3.10E-10
	D15-2_C	Nuclear_brightness_in_bud	-0.529	3.68E-10
	DCV15-1_C	CV_of_Nuclear_brightness_in_mother	0.529	3.94E-10
	A7-1_A	Size_of_actin_region	-0.516	1.17E-09
	A8-1_C	Total_brightness_of_actin_region_in_mother	0.505	3.10E-09
PC3*	C11-2_A1B	Bud_cell_size	-0.797	5.41E-28
	C12-2_A1B	Bud_cell_outline_length	-0.794	9.63E-28
	C107_A1B	Long_axis_length_in_bud	-0.746	5.96E-23
	A7-2_A1B	Size_of_actin_region_in_bud	-0.717	1.63E-20
	A107_A1B	Actin_c_api_ratio	0.659	1.47E-16
	C117_A1B	Cell_outline_ratio	-0.636	3.52E-15
	C118_A1B	Cell_size_ratio	-0.634	4.66E-15

	C123_A1B	Small_bud_ratio	0.620	2.53E-14
	A106	actin_b_ratio	0.615	4.82E-14
	C101_A1B	Whole_cell_size	-0.603	2.00E-13
	C123	small_bud_ratio_to_budded_cells	0.602	2.27E-13
	D210	nuclear_A_ratio_to_nuclear_AA1BC_cells	0.594	5.26E-13
	C119	no_bud_ratio	0.588	1.12E-12
	C122	large_bud_ratio	-0.562	1.65E-11
	D199	nuclear_A_ratio	0.549	5.76E-11
	C110_A1B	Distance_between_bud_tip_and_mother_long_axis_extension	-0.544	9.23E-11
	A108	actin_d_iso_ratio	-0.543	1.04E-10
PC4*	D16-3_A1B	Maximal_intensity_of_nuclear_brightness	0.570	7.21E-12
	DCV14-2_C	CV_of_Nuclear_size_in_bud	-0.561	1.90E-11
	D193_A1B	Average_of_nuclear_brightness	0.548	6.61E-11
	D14-1_C	Nuclear_size_in_mother	-0.519	8.88E-10
	D16-1_A	Maximal_intensity_of_nuclear_brightness	0.518	1.01E-09
PC5*	CCV12-1_C	CV_of_Mother_cell_outline_length	0.655	2.70E-16
	CCV11-1_C	CV_of_Mother_cell_size	0.625	1.43E-14
	CCV104_C	CV_of_Short_axis_length_in_mother	0.609	9.13E-14
	CCV101_C	CV_of_Whole_cell_size	0.609	9.34E-14
	CCV128_C	CV_of_Distance_between_middle_point_of_neck_and_mother_hip	0.560	1.99E-11
	DCV185_C	CV_of_Total_length_of_two_straight_segments_D11-1C4-1_and_D11-2C4-1	0.549	5.46E-11
	CCV102_C	CV_of_Whole_cell_outline_length	0.539	1.41E-10
	DCV186_C	CV_of_Total_length_of_two_straight_segments_D12-1C4-1_and_D12-2C4-1	0.534	2.33E-10
PC9*	D159_C	Angle_between_D2-1D2-2_and_C1-1C1-2	0.571	6.40E-12
	D158_C	Angle_between_D1-1D1-2_and_C1-1C1-2	0.566	1.11E-11
	C106_C	Bud_direction	0.555	3.21E-11
	C111_C	Distance_between_bud_tip_and_mother_short_axis_extension	-0.535	2.15E-10
PC10*	CCV104_A1B	CV_of_Short_axis_length_in_mother	0.559	2.09E-11
	CCV12-1_A1B	CV_of_Mother_cell_outline_length	0.558	2.50E-11
	CCV11-1_A1B	CV_of_Mother_cell_size	0.540	1.38E-10
	CCV103_A1B	CV_of_Long_axis_length_in_mother	0.523	6.50E-10
PC11*	DCV125_C	CV_of_Distance_between_nuclear_gravity_center_in_mother_and_mother_hip	0.624	1.71E-14
	DCV106_C	CV_of_Ratio_of_D103_to_C103	0.618	3.25E-14
	DCV103_C	CV_of_Distance_between_nuclear_gravity_center_in_mother_and_mother_tip	0.606	1.37E-13
	DCV141_C	CV_of_Distance_between_nuclear_brightest_point_in_mother_and_mother_hip	0.565	1.23E-11
	DCV128_C	CV_of_Distance_between_nuclear_brightest_point_in_mother_and_mother_tip	0.534	2.37E-10

*Principal component 1, 2, 3, 4, 5, 9, 10, and 11, respectively.

Table S3. Vacuole morphology of antifungal agent-treated yeast cells

Strain	**Drug**	Percentage of quinacrine-stained cells (%)*		
		Stained Vacuole	Stained Entire cell	Unstained Cells
BY4741	MOCK	41.6 ± 5.4	9.3 ± 2.2	49.1 ± 7.5
BY4741	FCZ	26.7 ± 8.0	13.9 ± 3.1	59.4 ± 10.1
BY4741	TBF	27.6 ± 5.6	21.3 ± 2.9	51.1 ± 4.1

* Cell count as a mean from three independent experiment ± standard error of the mean

Table S4. List of parameters involved in three PCs that optimally classified antifungal drugs at FRD= 0.1

PC	ID	Parameter description
PC63*	C125	Large bud ratio to budded cells
	C11-2_A1B	Bud cell size
	A7-2_A1B	Size of actin region in bud
	DCV179_A	Coefficient of variation of D179 A
	C118_A1B	Cell size ratio
	A108_A1B	Actin d ratio
	DCV196_A1B	Coefficient of variation of D196 A1B
	D143_A1B	Distance between nuclear outline point D6-1 and middle point of neck
	DCV102_A	Coefficient of variation of D102 A
	C12-2_A1B	Bud cell outline length
	C117_A1B	Cell outline ratio
	A108	actin d ratio
	C107_A1B	Long axis length in bud
	A110_A1B	Actin f ratio
	D144_C	Distance between nuclear outline point D6-2 in bud and middle point of neck
	DCV104_A1B	Coefficient of variation of D104 A1B
	D117_A	Distance between nuclear gravity center and cell center
	A107_A1B	Actin c ratio
	CCV112_A1B	Coefficient of variation of C112 A1B
	A9_C	Proportion of actin region at neck
PC54*	CCV11-1_C	Coefficient of variation of C11-1 C
	CCV110_C	Coefficient of variation of C110 C
	CCV126_A1B	Coefficient of variation of C126 A1B
	DCV193_A1B	Coefficient of variation of D193 A1B
	CCV12-1_C	Coefficient of variation of C12-1 C
	CCV109_C	Coefficient of variation of C109 C
	CCV103_C	Coefficient of variation of C103 C
	CCV101_C	Coefficient of variation of C101 C
	DCV158_C	Coefficient of variation of D158 C
	DCV159_C	Coefficient of variation of D159 C
	D137_C	Distance between nuclear brightest point in bud and bud center
PC77*	A113_A1B	Actin n ratio
	DCV196_C	Coefficient of variation of D196 C
	D131_C	Distance between nuclear brightest point in bud and middle point of neck
	A8-1_C	Total brightness of actin region in mother
	D153_C	Mobility of nucleus in bud
	A117	actin d ratio to budded cells
	D194_C	Maximal intensity of nuclear brightness divided by average in

	whole cell
C128_C	Distance between middle point of neck and mother hip
ACV121_C	Coefficient of variation of A121 C
A102_A1B	Bud actin region ratio to total region
A108_A1B	Actin d ratio
A108	Actin d ratio
D144_C	Distance between nuclear outline point D6-2 in bud and middle point of neck
CCV128_A1B	Coefficient of variation of C128 A1B
C125_C	Large bud ratio
C12-1_C	Mother cell outline length
D109_C	Distance between nuclear gravity center in bud and middle point of neck
C104_C	Short axis length in mother
C11-1_C	Mother cell size
DCV186_C	Coefficient of variation of D186 C
DCV185_C	Coefficient of variation of D185 C
D16-1_C	Maximal intensity of nuclear brightness in mother
CCV103_A1B	Coefficient of variation of C103 A1B
DCV177_C	Coefficient of variation of D177 C
CCV101_A1B	Coefficient of variation of C101 A1B
A7-1_C	Size of actin region in mother
C124_C	Medium bud ratio
C12-2_A1B	Bud cell outline length
C117_A1B	Cell outline ratio
C107_A1B	Long axis length in bud
D113_C	Ratio of D109 to C107
CCV12-1_A1B	Coefficient of variation of C12-1 A1B
CCV107_C	Coefficient of variation of C107 C
ACV120_C	Coefficient of variation of A120 C
DCV179_A	Coefficient of variation of D179 A
C118_A1B	Cell size ratio
DCV196_A1B	Coefficient of variation of D196 A1B
C112_C	Distance between middle point of neck and mother center
C118_C	Cell size ratio
C117_C	Cell outline ratio
A104_C	Relative distance of actin patch center from neck in bud
C123_A1B	Small bud ratio
CCV104_A1B	Coefficient of variation of C104 A1B
D123_C	Ratio of D121 to C107
A103_A1B	Relative distance of actin patch center from neck in mother
CCV13_C	Coefficient of variation of C13 C
A109_C	Actin e ratio
A102_C	Bud actin region ratio to total region
CCV12-2_C	Coefficient of variation of C12-2 C
DCV174_C	Coefficient of variation of D174 C
CCV102_C	Coefficient of variation of C102 C

DCV129_A1B	Coefficient of variation of D129 A1B
A109_A1B	Actin e ratio
C11-2_A1B	Bud cell size
CCV103_A	Coefficient of variation of C103 A
A104_A1B	Relative distance of actin patch center from neck in bud
ACV120_A1B	Coefficient of variation of A120 A1B
ACV9_A1B	Coefficient of variation of A9 A1B
CCV11-2_C	Coefficient of variation of C11-2 C
DCV195_C	Coefficient of variation of D195 C
A112_A1B	Actin cd ratio
DCV194_A	Coefficient of variation of D194 A
A7-2_A1B	Size of actin region in bud
A118	actin e ratio to budded cells
DCV15-1_A	Coefficient of variation of D15-1 A
C104_A1B	Short axis length in mother
CCV113_C	Coefficient of variation of C113 C
CCV108_C	Coefficient of variation of C108 C
A7-1_A1B	Size of actin region in mother
CCV112_A1B	Coefficient of variation of C112 A1B
C113_C	Distance between bud tip and mother long axis through middle point of neck
A109	actin e ratio
D132_A1B	Distance between nuclear brightest point and middle point of neck
ACV121_A1B	Coefficient of variation of A121 A1B
C101_C	Whole cell size
ACV122_C	Coefficient of variation of A122 C
C127_A	Thickness difference of cell wall

* Principal component 63, 54, and C77

Table S5. Results of GO term analysis showing the genes related to the effect of antifungal agents

Agent	GO category	GO ID	GO term	P-value	FDR	No. of AQG	No. of QG	No. of ABG	No. of BG	Gene(s) annotated to the term
FCZ	Cellular process	GO: 0007035	Vacuolar acidification	1.31E-07	0	8	65	23	4708	*VMA1, VMA3, VMA16, VMA5, VPH2, VMA6, VMA4, VMA11*
		GO:0051453	Regulation of intracellular pH	1.95E-07	0	8	65	24	4708	*VMA1, VMA3, VMA16, VMA5, VPH2, VMA6, VMA4, VMA11*
		GO:0030004	Cellular monovalent inorganic cation homeostasis	3.34E-06	0	8	65	33	4708	*VMA1, VMA3, VMA16, VMA5, VPH2, VMA6, VMA4, VMA11*
	Cellular function	GO:0044769	ATPase activity, coupled to transmembrane movement of ions, rotational mechanism	5.87E-07	0	7	65	22	4708	*VMA1, VMA16, VMA5, VMA6, VMA4, VMA11, ATP15*
		GO:0015077	Monovalent inorganic cation transmembrane transporter activity	4.85E-05	0	8	65	57	4708	*VMA1, VMA3, VMA16, VMA5, VMA6, VMA4, VMA11, ATP15*
	Cellular component	GO:0016471	Vacuolar proton-transporting V-type ATPase complex	9.50E-09	0	7	65	13	4708	*VMA1, VMA3, VMA16, VMA5, VMA6, VMA4, VMA11*
		GO:0000220	Vacuolar proton-transporting V-type ATPase, V0 domain	4.18E-05	0	4	65	6	4708	VMA3, VMA16, VMA6, VMA11
		GO:0033178	Proton-transporting two-sector ATPase complex, catalytic domain	0.0006	0	4	65	10	4708	VMA1, VMA5, VMA4, ATP15
		GO:0000221	Vacuolar proton-transporting V-type ATPase, V1 domain	0.0073	0	3	65	7	4708	VMA1, VMA5, VMA4

Note: **No. AQG**: number of annotated query genes; **No. QG**: number of query genes; **No. ABG**: number of annotated background genes; **No. BG**: number of background genes

Table S5. Results of GO term analysis showing the genes related to the effect of the antifungal agents on the WT yeast (Continued)

Agent	GO category	GO ID	GO term	P-value	FDR	No. of AQG	No. of QG	No. of ABG	No. of BG	Gene(s) annotated to the term
TBF	Cellular process	GO:0007035	Vacuolar acidification	3.12E-07	0	11	197	23	4708	*VMA2, VMA1, VPS3, VMA3, VMA7, VMA16, VMA5, VPH2, VMA6, VMA4, VMA11*
		GO:0030004	Cellular monovalent inorganic cation homeostasis	2.32E-06	0	12	197	33	4708	*VMA2, VMA1, VPS3, VMA3, VMA7, VMA16, TOK1, VMA5, VPH2, VMA6, VMA4, VMA11*
	Cellular function	GO:0046961	Proton-transporting ATPase activity, rotational mechanism	2.58E-06	0	8	197	14	4708	*VMA2, VMA1, VMA7, VMA16, VMA5, VMA6, VMA4, VMA11*
	Cellular component	GO:0016471	Vacuolar proton-transporting V-type ATPase complex	3.23E-08	0	9	197	13	4708	*VMA2, VMA1, VMA3, VMA7, VMA16, VMA5, VMA6, VMA4, VMA11*
		GO:0022627	Cytosolic small ribosomal subunit	1.67E-06	0	14	197	51	4708	*FUN12, RPS14A, RPS26B, RPS28B, RPS30A, RPS29A, RPS17A, RPS1B, ASC1, RPS16A, RPS7B, RPS7A, RPS30B, RPS10A*
		GO:0000221	Vacuolar proton-transporting V-type ATPase, V1 domain	0.0004	0	5	197	7	4708	*VMA2, VMA1, VMA7, VMA5, VMA4*
		GO:0000220	Vacuolar proton-transporting V-type ATPase, V0 domain	0.0066	0	4	197	6	4708	*VMA3, VMA16, VMA6, VMA11*

Note:- **No. AQG**: number of annotated query genes; **No. QG**: number of query genes; **No. ABG**: number of annotated background genes; **No. BG**: number of background genes

Table S5. Results of GO term analysis showing the genes related to the effect of antifungal agents (Continued)

Agent	GO category	GO ID	GO term	P-value	FDR	No. of AQG	No. of QG	No. of ABG	No. of BG	*Gene(s) annotated to the term*
AMF	Cellular process	GO:0007035	Vacuolar acidification	8.41E-08	0	13	306	22	4708	*VMA2,VMA1,RRG1,RAV2,VMA 3,VMA8,VMA7,VMA5,VPH2,MI H1,VMA6,VMA4,VMA11*
		GO:0051452	Intracellular pH reduction	8.41E-08	0	13	306	22	4708	*VMA2,VMA1,RRG1,RAV2,VMA 3,VMA8,VMA7,VMA5,VPH2,MI H1,VMA6,VMA4,VMA11*
		GO:0045851	pH reduction	8.41E-08	0	13	306	22	4708	*VMA2,VMA1,RRG1,RAV2,VMA 3,VMA8,VMA7,VMA5,VPH2,MI H1,VMA6,VMA4,VMA11*
		GO:0030641	Regulation of cellular pH	1.82E-07	0	13	306	23	4708	*VMA2,VMA1,RRG1,RAV2,VMA 3,VMA8,VMA7,VMA5,VPH2,MI H1,VMA6,VMA4,VMA11*
	Cellular function	GO:0046961	Proton-transporting ATPase activity, rotational mechanism	5.43E-05	0	8	306	13	4708	*VMA2,VMA1,VMA8,VMA7,VMA 5,VMA6,VMA4,VMA11*
		GO:0015078	H+ transmembrane transporter activity	0.00219	0	12	306	43	4708	*VMA2,VMA1,VMA3,VMA8,VMA 7,COX6,VMA5,VMA6,VNX1,VM A4,VMA11*
		GO:0042625	ATPase activity, coupled to transmembrane movement of ions	0.00817	0	9	306	28	4708	*VMA2,VMA1,VMA8,VMA7,VMA 5,VMA6,VMA4,VMA11*

Note:- **No. AQG**: number of annotated query genes; **No. QG**: number of query genes; **No. ABG**: number of annotated background genes; **No. BG**: number of background genes

Table S5. Results of GO term analysis showing the genes related to the effect of antifungal agents (Continued)

Agent	GO category	GO ID	GO term	P-value	FDR	No. of AQG	No. of QG	No. of ABG	No. of BG	*Gene(s) annotated to the term*
AMF	Cellular component	GO:0016471	Vacuolar proton-transporting V-type ATPase complex	7.61E-07	0	9	306	12	4708	*VMA2,VMA1,VMA3,VMA8,VMA7,VMA5,VMA6,VMA4,VMA11*
		GO:0033176	Proton-transporting V-ATPase complex	7.61E-07	0	9	306	12	4708	*VMA2,VMA1,VMA3,VMA8,VMA7,VMA5,VMA6,VMA4,VMA11*
		GO:0016469	Proton-transporting two-sector ATPase complex	8.32E-05	0	10	306	22	4708	*VMA2,VMA1,VMA3,VMA8,VMA7,VMA5,VMA6,VMA4,VMA11*
		GO:0000221	Vacuolar proton-transporting V-type ATPase, V1 domain	0.00011	0	6	306	7	4708	*VMA2,VMA1,VMA8,VMA7,VMA5,VMA4*
		GO:0033180	Proton-transporting V-type ATPase, V1 domain	0.00011	0	6	306	7	4708	*VMA2,VMA1,VMA8,VMA7,VMA5,VMA4*

Note:- **No. AQG**: number of annotated query genes; **No. QG**: number of query genes; **No. ABG**: number of annotated background genes; **No. BG**: number of background genes

Table S5. Results of GO term analysis showing the genes related to the effect of antifungal agents (Continued)

Agent	GO category	GO ID	GO term	P-value	FDR	No. of AQG	No. of QG	No. of ABG	No. of BG	*Gene(s) annotated to the term*
AMF	Cellular component	GO:0016471	Vacuolar proton-transporting V-type ATPase complex	7.61E-07	0	9	306	12	4708	*VMA2,VMA1,VMA3,VMA8,VMA7,VMA5,VMA6,VMA4,VMA11*
		GO:0033176	Proton-transporting V-ATPase complex	7.61E-07	0	9	306	12	4708	*VMA2,VMA1,VMA3,VMA8,VMA7,VMA5,VMA6,VMA4,VMA11*
		GO:0016469	Proton-transporting two-sector ATPase complex	8.32E-05	0	10	306	22	4708	*VMA2,VMA1,VMA3,VMA8,VMA7,VMA5,VMA6,VMA4,VMA11*
		GO:0000221	Vacuolar proton-transporting V-type ATPase, V1 domain	0.00011	0	6	306	7	4708	*VMA2,VMA1,VMA8,VMA7,VMA5,VMA4*
		GO:0033180	Proton-transporting V-type ATPase, V1 domain	0.00011	0	6	306	7	4708	*VMA2,VMA1,VMA8,VMA7,VMA5,VMA4*

Note:- **No. AQG**: number of annotated query genes; **No. QG**: number of query genes; **No. ABG**: number of annotated background genes; **No. BG**: number of background genes

Table S5. Results of GO term analysis showing the genes related to the effect of antifungal agents (Continued)

Agent	**GO category**	**GO ID**	**GO term**	**P-value**	**FDR**	**No. of AQG**	**No. of QG**	**No. of ABG**	**No. of BG**	***Gene(s) annotated to the term***
FCS	Cellular process	GO:0042274	Ribosomal small subunit biogenesis	2.57E-11	0	15	98	52	4708	*FUN12, RPS14A, BUD23, RPS18A, RPS24A, LTV1, RPS0B, FYV7, RPS17A, RPS18B, RPS1B, RPS16A, RPS19B, RPS19A, BUD21*
		GO:0051029	rRNA transport	0.0000	0	8	98	11	4708	*RPS18A, RPS26B, RPS0B, RPS28B, RPS18B, RPS19B, RPS19A, RPS10A*
		GO:0000462	Maturation of SSU-rRNA from tricistronic rRNA transcript (SSU-rRNA, 5.8S rRNA, LSU-rRNA)	1.87E-08	0	11	98	34	4708	*FUN12, RPS14A, BUD23, RPS18A, RPS24A, RPS0B, FYV7, RPS18B, RPS1B, RPS16A, BUD21*
		GO:0006405	RNA export from nucleus	3.98E-05	0	10	98	52	4708	*NPL3, RPS18A, RPS26B, RPS0B, RPS28B, RPS18B, RPS19B, THP1, RPS19A, RPS10A*
		GO:0000466	Maturation of 5.8S rRNA from tricistronic rRNA transcript	5.70E-04	0	6	98	18	4708	*BUD23, RPS18A, LRP1, RPS0B, RPS18B, BUD21*
		GO:0031123	RNA 3'-end processing	0.0093	0	7	98	41	4708	*CCR4, LRP1, CTK2, RPS0B, CTK3, POP2, THP1*
	Cellular component	GO:0022627	Cytosolic small ribosomal subunit	5.39E-18	0	19	98	51	4708	*FUN12, RPS14A, RPS18A, RPS24A, RPS26B, RPS4B, RPS4A, RPS0B, RPS28B, RPS30A, RPS22B, RPS17A, RPS18B, RPS1B*

Note: **No. AQG**: number of annotated query genes; **No. QG**: number of query genes; **No. ABG**: number of annotated background genes; **No. BG**: number of background genes

Table S5. Results of GO term analysis showing the genes related to the effect of antifungal agents (Continued)

Agent	GO category	GO ID	GO term	P-value	FDR	No. of AQG	No. of QG	No. of ABG	No. of BG	*Gene(s) annotated to the term*
ECB	Cellular process	GO:0007035	Vacuolar acidification	6.10E-06	0	11	253	23	4708	*VMA2, VMA3, VMA7, VMA16, RAV1, VMA5, VPH2, VMA6, VMA4, VMA11, VMA13*
		GO:0042274	Ribosomal small subunit biogenesis	3.00E-04	0	14	253	52	4708	*FUN12, RPS14A, BUD23, RPS16B, LSM6, RPS24A, LTV1, RPS17A, RPS1B, LSM7, RPS19B, RPS19A, BUD21, YAR1*
		GO:0030004	Cellular monovalent inorganic cation homeostasis	5.40E-04	0	11	253	33	4708	*VMA2, VMA3, VMA7, VMA16, RAV1, VMA5, VPH2, VMA6, VMA4, VMA11, VMA13*
	Cellular function	GO:0044769	ATPase activity, coupled to transmembrane movement of ions, rotational mechanism	3.05E-08	0	12	253	22	4708	*VMA2, VMA7, VMA16, VMA5, VMA6, ATP18, VMA4, ATP4, VMA11, ATP15, ATP20, VMA13*
		GO:0046961	Proton-transporting ATPase activity, rotational mechanism	8.73E-07	0	9	253	14	4708	*VMA2, VMA7, VMA16, VMA5, VMA6, VMA4, ATP4, VMA11, VMA13*
		GO:0042626	ATPase activity, coupled to transmembrane movement of substances	1.85E-05	0	14	253	48	4708	*VMA2, SPF1, VMA7, VMA16, VMA5, VMA6, ATP18, PDR18, VMA4, ATP4, VMA11, ATP15, ATP20, VMA13, VMA2, VMA3*

Note: **No. AQG**: number of annotated query genes; **No. QG**: number of query genes; **No. ABG**: number of annotated background genes; **No. BG**: number of background genes

Table S5. Results of GO term analysis showing the genes related to the effect of antifungal agents (Continued)

Agent	GO category	GO ID	GO term	P-value	FDR	No. of AQG	No. of QG	No. of ABG	No. of BG	*Gene(s) annotated to the term*
ECB	Cellular component	GO:0016471	Vacuolar proton-transporting V-type ATPase complex	3.98E-07	0	9	253	13	4708	*VMA7, VMA16, VMA5, VMA6, VMA4, VMA11, VMA13*
		GO:0022627	Cytosolic small ribosomal subunit	6.89E-06	0	15	253	51	4708	*FUN12, RPS14A, PAT1, RPS16B, RPS24A, RPS22B, RPS29A, RPS17A, RPS1B, ASC1, RPS19B, RPS19A, RPS7A, RPS30B, RPS10A*
		GO:0033177	Proton-transporting two-sector ATPase complex, transporting domain	0.00032	0	7	253	13	4708	*VMA3, VMA16, VMA6, ATP18, ATP4, VMA11, ATP20*
		GO:0000221	Vacuolar proton-transporting V-type ATPase, V1 domain	0.00171	0	5	253	7	4708	*VMA2, VMA7, VMA5, VMA4, VMA13*

Note:- **No. AQG**: number of annotated query genes; **No. QG**: number of query genes; **No. ABG**: number of annotated background genes; **No. BG**: number of background genes

Table S5. Results of GO term analysis showing the genes related to the effect of antifungal agents (Continued)

Agent	GO category	GO ID	GO term	P-value	FDR	No. of AQG	No. of QG	No. of ABG	No. of BG	*Gene(s) annotated to the term*
MCF	Cellular function	GO:0015078	Hydrogen ion transmembrane transporter activity	0.00264	0	8	134	44	4708	*VMA3, VMA5, VMA6, ATP18, VMA4, ATP4, VMA11, ATP15*
		GO:0046961	Proton-transporting ATPase activity, rotational mechanism	0.00285	0	5	134	14	4708	*VMA5, VMA6, VMA4, ATP4, VMA11*
	Cellular component	GO:0016471	Vacuolar proton-transporting V-type ATPase complex	0.00327	0	5	134	13	4708	*VMA3, VMA5, VMA6, VMA4, VMA11*
		GO:0033177	Proton-transporting two-sector ATPase complex, transporting domain	0.00327	0	5	134	13	4708	*VMA3, VMA6, ATP18, ATP4, VMA11*

Note: -

(1) **No. AQG**: number of annotated query genes; **No. QG**: number of query genes; **No. ABG**: number of annotated background genes; **No. BG**: number of background genes.

(2) The analysis was executed by "GO term finder (ver. 0.83)" in *Saccharomyces* genome database http://www.yeastgenome.org/. Query genes were selected as those genes deletion mutants were morphologically similar to cells treated by indicated drug 65, 197, 306, 98, 253, and 134 for FCZ, TBF, AMF, FCS, ECB, and MCF, respectively; $P < 0.001$ after Bonferroni correction; Fig. 1-3, Fig. 1-5). And 4,708 of 4,718 non-essential genes were considered as the background gene set. To simplify the result, GO term which had the lowest *P* value was selected as representative of subset of GO terms that shared the same annotated genes and GO category.

Table S6. Independent morphological features describing triple mutants

PC#	Param. ID	Parameter description	Loadings	p values	Independent features represented
PC1	D175_A1B	Maximal_distance_between_nuclear_gravity_center_and_nuclear_outline	0.715	3.88221E-09	Nuclear brightness increased at G1 phase
	D178_A1B	Nuclear_long_axis_length	0.714	4.06952E-09	
	D181_A1B	Nuclear_minimum_radius	0.649	2.58464E-07	
	D15-2_C	Nuclear_brightness_in_bud	0.786	8.14499E-12	
	D192_C	Average_of_nuclear_brightness_in_bud	0.651	2.25623E-07	Increased actin region & brightness in mother, increased cell size, and increased nuclear brightness in S/G2 phase
	D16-2_C	Max_intensity_of_nuclear_brightness_in_bud	0.663	1.15067E-07	
	D16-1_A	Maximal_intensity_of_nuclear_brightness	0.739	5.5488E-10	
	D16-3_C	Max_intensity_of_nuclear_brightness_in_whole_cell	0.621	1.15819E-06	
	D14-3_A1B	Nuclear_size	0.857	1.07458E-15	
	D15-3_C	Nuclear_brightness_in_whole_cell	0.682	3.67276E-08	
	C112_A1B	Distance_between_middle_point_of_neck_and_mother_center	0.663	1.17904E-07	
	C11-1_A1B	Mother_cell_size	0.605	2.59802E-06	
	C104_A1B	Short_axis_length_in_mother	0.672	6.5541E-08	
	D15-3_A1B	Nuclear brightness	0.672	7.71858E-13	
	C101_A1B	Whole_cell_size	0.712	4.69903E-09	
	D179_A	Nuclear_minimum_radius	0.707	6.4548E-09	Increased nuclear brightness in mother & bud and increased nuclear brightness in the cell in M phase
	A7-1_A1B	Size_of_actin_region_in_mother	0.553	2.54224E-05	
	C103_A	Long_axis_length_in_whole_cell	0.408	1.11632E-06	
	A101_A1B	Actin_region_ratio_in_whole_cell	0.554	2.49405E-05	
	A8-1_A1B	Total_brightness_of_actin_region_in_mother	0.621	1.14999E-06	
	D136_A1B	Distance_between_nuclear_brightest_point_and_mother_center	0.571	1.2246E-05	

Table S6. Independent morphological features describing triple mutants (Continued)

PC No.	Parameter ID	Parameter description	Loadings	*p* values	Independent feature represented
PC2	C113_C	Distance_between_bud_tip_and_mother_long_axis_through_middle_point_of_neck	0.556	2.31037E-05	
	C102_C	Whole_cell_outline_length	0.793	4.01602E-12	
	D186_C	Total_length_of_two_straight_segments_D12-1C4-1_and_D12-2C4-1	0.687	2.55296E-08	
	D185_C	Total_length_of_two_straight_segments_D11-1C4-1_and_D11-2C4-1	0.687	2.53765E-08	
	C107_C	Long_axis_length_in_bud	0.687	2.51394E-08	
	C118_A1B	Cell_size_ratio	-0.615	1.5566E-06	Increase cell size in M phase
	C123_A1B	Small_bud_ratio	0.596	3.96526E-06	
	C128_C	Distance_between_middle_point_of_neck_and_mother_hip	0.639	4.34514E-07	
	C104_C	Short_axis_length_in_mother	0.700	1.07846E-08	
	C12-1_C	Mother_cell_outline_length	0.755	1.50259E-10	
	D14-3_C	Nuclear_size_in_whole_cell	0.755	1.38529E-05	
	C117_A1B	Cell_outline_ratio	-0.634	5.90011E-07	
	C103_C	Long_axis_length_in_mother	0.687	2.5627E-08	
	C11-1_C	Mother_cell_size	0.747	2.97838E-10	
	C101_C	Whole_cell_size	0.808	7.72521E-13	

Table S6. Independent morphological features describing triple mutants (Continued)

PC#	Param. ID	Parameter description	Loadings	p values	Independent features represented
PC3	D198_C	Ratio_of_nuclear_brightness	0.572	1.14397E-05	Variation in nuclear brightness at G1 stage
	D193_A1B	Average_of_nuclear_brightness	0.572	1.32956E-06	
	D16-1_C	Max_intensity_nuclear_brightness_in_mother	-0.574	1.08118E-05	Average nuclear brightness at S/G2 stage
	DCV15-1_A	Coefficient_of_variation_of_D15-1_A	0.732	1.03126E-09	Nuclear brightness in mother cell
	D15-1_C	Nuclear_brightness_in_mother	-0.590	5.19487E-06	
	DCV191_A	Coefficient_of_variation_of_D191_A	0.626	9.17129E-07	
	DCV16-1_A	Coefficient_of_variation_of_D16-1_A	0.597	3.71716E-06	
PC4	D176_C	Nuclear_long_axis_length_in_mother	0.562	1.76726E-05	
	D173_C	Maximal_distance_between_nuclear_gravity_center_and_nuclear_outline_in_mother	0.575	1.01286E-05	Nuclear mobility in mother at S/G2 phase
	D152_A1B	Mobility_of_nucleus_in_mother	-0.623	1.03284E-06	
	D143_C	Distance_between_nuclear_outline_D6-1 in_mother_and_middle_point_of_neck	-0.679	4.30786E-08	
	D108_C	Distance_between_nuclear_gravity_center _in_mother_and_middle_point_of_neck	-0.627	8.51759E-07	
	D130_C	Distance_between_nuclear_brightest_point _in_mother_and_middle_point_of_neck	-0.635	5.68895E-07	
PC5	DCV16-3_C	Coefficient_of_variation_of_D16-3_C	-0.555	2.36605E-05	
PC6	D116_C	Distance_between_two_nuclear_gravity_centers_through_middle_point_of_neck	0.553	2.59907E-05	
	C110_A1B	Distance_between_bud_tip_and_mother	0.556	2.2393E-05	
	C12-1_A1B	Mother_cell_outline_length	0.559	1.94535E-05	
PC11	D147_A	Relative_distance_of_nuclear_gravity_center_to_cell_center	-0.581	7.74174E-06	

Table S7. Description of *S. cerevisiae* hypersensitive deletion strains used in this study

Strain	Alias	Genotype*	Description
Y8835	WT	Ura3*Δ*::natR; can1*Δ*::STE2pr-Sp_his5 lyp1*Δ*; his3*Δ*1 leu2*Δ*0 ura3*Δ*0 met15^0 LYS2+	
Y12669	*pdr1Δ*	Pdr1*Δ*::NATMX; his3*Δ*1 leu2*Δ*0 ura3*Δ*0 met15*Δ*0 LYS2+	Transcription factor that regulates the pleiotropic drug response (PDR)
Y13118	*pdr3Δ pdr1Δ*	Pdr3*Δ*::KIura3; pdr1*Δ*::NATMX; can1*Δ*::STE2pr-Sp_his5 lyp1*Δ*; his3*Δ*1 leu2*Δ*0 ura3*Δ*0 met15*Δ*0 LYS2+	
Y13206	*snq2Δ pdr3Δ pdr1Δ*	Snq2*Δ*::KILeu2; pdr3*Δ*::KIura3; pdr1*Δ*::NATMX;can1*Δ*::STE2pr-Sp_his5 lyp1*Δ*; his3*Δ*1 leu2*Δ*0 ura3*Δ*0 met15*Δ*0 LYS2+	
Y13282	*snq2Δ*	Snq2*Δ*::KILeu2; lyp1*Δ* his3*Δ*1 leu2 *Δ*0 ura3*Δ*0 met15*Δ*0 LYS2+	Plasma membrane ATP-binding cassette (ABC) transporter
Y13287	*snq2Δ pdr1Δ*	Snq2*Δ*::KILeu2; pdr1*Δ*::NATMX; can1*Δ*::STE2pr-Sp_his5 lyp1*Δ*;his3*Δ*1 leu2*Δ*0 ura3*Δ*0 met15*Δ*0 LYS2+	
Y13291	*snq2Δ pdr3Δ*	Snq2*Δ*::KILeu2; pdr3*Δ*::KIura3; can1*Δ*::STE2pr-Sp_his5 lyp1*Δ*;his3*Δ*1 leu2*Δ*0 ura3*Δ*0 met15*Δ*0 LYS2+	
Y13307	*pdr3Δ*	Pdr3*Δ*::KIura3; can1*Δ*::STE2pr-Sp_his5 lyp1*Δ*; his3*Δ*1 leu2*Δ*0 ura3*Δ*0 met15*Δ*0 LYS2+	Transcriptional activator of the PDR network; Regulates expression of ABC transporters

*Adapted from: Andrusiak K (2012)

Table S8. Representative gene set enrichment for the GO terms in antimicrobial agents treated hypersensitive strain

Drug	GO category	GOID	GO term	No. AQG	No. QG	No. ABG	No. BGG	*p*-value	FDR	Expected FP	Gene(s) annotated to the term
BML	Process	7021	Tubulin complex assembly	5	20	9	1980	1.22E-06	0	0	GIM4, PAC2, CIN4, CIN1, CIN2
		6457	Protein folding	5	20	35	1980	0.00267	0	0	PLP1, PAC2, CIN4, CIN1, CIN2
	Function	15631	Tubulin binding	4	20	17	1980	0.00023	0	0	GIM4, PAC2, ASE1, CIN1
		8092	Cytoskeletal protein binding	4	20	30	1980	0.00246	0	0	GIM4, PAC2, ASE1, CIN1
TCM	Process	1901137	Carbohydrate derivative biosynthetic process	16	165	55	1980	0.00324	0	0	PMT2, MNN2, MNN10, ERD1, SAM2, GDA1, GUP1, LAS21, HOC1, ARV1, EOS1, IRA2, PPM2, ALG6, OST3, ALG5
		9101	Glycoprotein biosynthetic process	10	165	24	1980	0.00635	0	0	PMT2, MNN2, MNN10, ERD1, GDA1, HOC1, EOS1, ALG6, OST3, ALG5
ECB	process	70651	Nonfunctional rRNA decay	4	60	4	1980	0.00036	0	0	XRN1, RTT101, HBS1, MMS1
		71840	Cellular component organization or biogenesis	38	60	697	1980	0.00287	0	0	MDM10, SLA1, REI1, WHI4, RAD55, SPO71, NUM1, MNN10, ESC2, SLX8, BEM2, XRN1, PAC10, VMA21, KSP1, EST3, APQ12, RTT101, HOC1, LHS1, BUD2, NUP133, HBS1, RTT109, RPS28B, MMS22, TSR2, UBX2, CIK1, MRE11, GAS1, RPS19B, BUB3, RPS10A, RMI1, BEM4, CTF4, KAR3

Note: No. AQG-number of query genes; No.QG - number of query genes; No. ABG-number of annotated background genes; No. BG-number of background genes

Table S8. Representative gene set enrichment for the GO terms in antimicrobial agents treated hypersensitive strain (Continued)

Drug	GO category	GOID	GO_term	No. AQG	No. QG	No. ABG	No. BGG	P-value	FDR	EFP	Gene(s) annotated to the term
MMS	Process	6259	DNA metabolic process	89	563	159	1980	3.96E-11	0	0	SAW1,SWD1,HEK2,HHT,RDH54,HSM3,DPB3,DCC1,RIM1,SLX5,RPN4,RAD59,BRE1,RAD57,RAD28,RAD55,MSH6,DPB4,SAC3,HTA1,IRC3, ESC2,SEM1,RAD51,SLX8,RAD4,LIF1,SOH1,RAD54,SAE2,SKI8,RTF1,CLB6,RRM3,WSS1,RTT107,CTF8,EST3,FKH1,:RTT101, SET2,POL32,RAD27,APN1,NUP133,RTT109,BRE2,RAD5,HOG1,SWI6,TOP3,MMS22,REC102,RSC2,PSY3,CTF3,CST9,CDC73,TSA1, RAD52,CSM3,CTF18,MLH1,SGS1,MRE11,FKH2,PSY2,TOF1,MCK1,STB1,MSH2,HMI1,DIA2,LEO1,ELG1,IES4,RFM1,VTS1,RAD1, RMI1,ELC1,LGE1,CTI6,HSP82,REC8,CLB5,CTF4,MMS1
		90304	Nucleic acid metabolic process	191	563	452	1980	5.44E-10	0	0	ATS1,SAW1,SWD1,BUD14,FMT1,RRN10,HEK2,YBL055C,NUP170,HHT1,RPS11B,RDH54,TEC1,HSM3,DPB3,DCC1,RIM1,SNT1,BUD31, HCM1,PAT1,PTC1,SLX5,RPN4,SLM3,RAD59,BRE1,TRM3,RAD57,RPS11A,RAD28,RAD55,MSH6,DPB4,INO2,RPA14,SAC3,HMO1,HTA1, IRC3,ESC2,SEM1,SPT3,LRS4,SDC1,EDC3,RAD51,SWI4,SLX8,RTR1,RAD4,PDR1,CKB1,DBP3,LIF1,ARC1,SOH1,MRM2,RAD54,XRN1, BUD13,SAE2,HOS2,SKI8,RTF1,SLX9,CLB6,RPS23A,GTR2,ELP2,YAP3,RPS27B,RRM3,PIH1,UBA4,WSS1,RTT107,STB5,CTF8,SKN7,EST3,V ID28,NOT3,AIR1,FKH1,MLP2,IST3,DAL81,MGA2,RTT101,SAP185,ASF1,LSM1,SET2,POL32,RAD27,APN1,CTK1,TOF2,IRS4,DBP7,SAP190, SET3,RPS21A,MSA2,NUP133,RTT109,PPR1,BRE2,RAD5,RPS0B,HOG1,PUS5,SWI6,TOP3,RPS28B,MMS22,REC102,RSC2,PSY3,CTF3, IKI3,CST9,SKI2,CDC73,RPS18B,TSA1,RAD52,RPS1B,NGL3,GTR1,CSM3,MOT3,CTF18,YMR087W,RPS16A,MLH1,SPT21,SGS1,ESC1, MRE11,ELP6,FKH2,LSM7,PSY2,RTT106,SIN4,TOF1,MCK1,STB1,DAL82,CSE2,MPP6,HTZ1,MSH2,HMI1,SKM1,HST3,CIN5,HIR2,CKA2,MS A1,BUD21,DIA2,LEO1,ELG1,IES4,NPT1,PUS7,RFM1,VTS1,RAD1,RMI1,ELC1,LGE1,ELP3,RLM1,RPS6A,CBC2,CTI6,LEA1,USV1, HSP82,HAL1,REC8,HAA1,ROX1,CLB5,RPS23B,CTF4,MMS1
		6974	Cellular response to DNA damage stimulus	63	563	102	1980	8.78E-10	0	0	SAW1,HHT1,RDH54,HSM3,DPB3,DCC1,SLX5,RPN4,RAD59,BRE1,RAD57,RAD28,RAD55,MSH6,DPB4,SAC3,HTA1,ESC2,SLX8,RAD4, CKB1,LIF1,SOH1,RAD54,SAE2,RTF1,RRM3,WSS1,RTT107,RTT101,POL32,GRR1,RAD27,APN1,NUP133,RTT109,RAD5,YLR235C,MMS22, RSC2,PSY3,CDC73,TSA1,RAD52,CSM3,CTF18,MLH1,SGS1,MRE11,MKT1,PSY2,TOF1,MCK1,MSH2,CKA2,LEO1,ELG1,IES4,RAD1, RMI1,ELC1,CTF4,MMS1
		6725	Cellular aromatic compound metabolic process	209	563	519	1980	9.98E-09	0	0	ATS1,SAW1,SWD1,BUD14,FMT1,RRN10,HEK2,URA7,YBL055C,NUP170,HHT1,RPS11B,RDH54,TEC1,PHO3,HSM3,DPB3,DCC1,RIM1, SNT1,BUD31,HCM1,PAT1,PTC1,SLX5,RPN4,SLM3,RAD59,BRE1,TRM3,RAD57,TRP1,RPS11A,RAD28,RAD55,MSH6,DPB4,INO2,RPA14, SAC3,HMO1,HTA1,HNT2,IRC3,ESC2,SEM1,SPT3,LRS4,SDC1,SAM2,FDC1,EDC3,RAD51,SWI4,SLX8,RTR1,RAD4,PDR1,CKB1,DBP3,LIF1, ARC1,SOH1,MRM2,RAD54,XRN1,BUD13,SAE2,HOS2,SKI8,RTF1,SLX9,CLB6,RPS23A,GTR2,ELP2,YAP3,RPS27B,RRM3,PIH1,UBA4, WSS1,RTT107,STB5,CTF8,SKN7,EST3,VID28,HIS6,NOT3,AIR1,FKH1,MLP2,IST3,DAL81,MGA2,RTT101,SAP185,ASF1,LSM1,SET2,POL32, RAD27,APN1,CTK1,TOF2,IRS4,DBP7,SAP190,SET3,RPS21A,MSA2,NUP133,RTT109,PPR1,BRE2,RAD5,RPS0B,HOG1,PUS5,SWI6,TOP3, RPS28B,MMS22,REC102,RSC2,PSY3,CTF3,IKI3,CST9,SKI2,CDC73,APT1,RPS18B,TSA1,RAD52,RPS1B,NGL3,GTR1,CSM3,MOT3,CTF18, YMR087W,RPS16A,MLH1,SPT21,SGS1,PFK2,ESC1,MRE11,COX7,ABZ2,ADH2,ELP6,FKH2,LSM7,PSY2,RTT106,SIN4,TOF1,MCK1,STB1, DAL82,CSE2,MPP6,HTZ1,THI20,IRA2,MSH2,HMI1,SKM1,HST3,CIN5,HIR2,CKA2,MSA1,BUD21,DIA2,LEO1,ELG1,IES4,NPT1,PUS7,RFM1, VTS1,RAD1,RMI1,ELC1,LGE1,ELP3,RLM1,RPS6A,COX10,CBC2,CTI6,LEA1,THI6,USV1,HSP82,HAL1,REC8,HAA1,ROX1,CLB5,THI22, RPS23B,CTF4,MMS1,QCR2
		46483	Heterocycle metabolic process	209	563	523	1980	2.58E-08	0	0	ATS1,SAW1,SWD1,BUD14,FMT1,RRN10,HEK2,URA7,YBL055C,NUP170,HHT1,RPS11B,RDH54,TEC1,PHO3,HSM3,DPB3,DCC1,RIM1, SNT1,BUD31,HCM1,PAT1,PTC1,SLX5,RPN4,SLM3,RAD59,BRE1,TRM3,RAD57,TRP1,RPS11A,RAD28,RAD55,MSH6,DPB4,INO2,RPA14, SAC3,HMO1,HTA1,HNT2,IRC3,ESC2,SEM1,SPT3,LRS4,SDC1,SAM2,EDC3,RAD51,SWI4,SLX8,RTR1,RAD4,PDR1,CKB1,DBP3,LIF1,ARC1, SOH1,MRM2,RAD54,XRN1,BUD13,SAE2,HOS2,SKI8,RTF1,SLX9,CLB6,RPS23A,GTR2,ELP2,YAP3,RPS27B,RRM3,PIH1,UBA4,WSS1, RTT107,STB5,CTF8,SKN7,EST3,VID28,HIS6,NOT3,AIR1,FKH1,MLP2,IST3,DAL81,DAL4,MGA2,RTT101,SAP185,ASF1,LSM1,SET2,POL32, RAD27,APN1,CTK1,TOF2,IRS4,DBP7,SAP190,SET3,RPS21A,MSA2,NUP133,RTT109,PPR1,BRE2,RAD5,RPS0B,HOG1,PUS5,SWI6,TOP3, RPS28B,MMS22,REC102,RSC2,PSY3,CTF3,IKI3,CST9,SKI2,CDC73,APT1,RPS18B,TSA1,RAD52,RPS1B,NGL3,GTR1,CSM3,MOT3,CTF18, YMR087W,RPS16A,MLH1,SPT21,SGS1,PFK2,ESC1,MRE11,COX7,ABZ2,ADH2,ELP6,FKH2,LSM7,PSY2,RTT106,SIN4,TOF1,MCK1,STB1, DAL82,CSE2,MPP6,HTZ1,THI20,IRA2,MSH2,HMI1,SKM1,HST3,CIN5,HIR2,CKA2,MSA1,BUD21,DIA2,LEO1,ELG1,IES4,NPT1,PUS7, RFM1,VTS1,RAD1,RMI1,ELC1,LGE1,ELP3,RLM1,RPS6A,COX10,CBC2,CTI6,LEA1,THI6,USV1,HSP82,HAL1,REC8,HAA1,ROX1,CLB5, THI22,RPS23B,CTF4,MMS1,QCR2
		51276	Chromosome organization	99	563	200	1980	3.37E-08	0	0	SWD1,SHE1,HEK2,NUP170,HHT1,RDH54,MSI1,DPB3,DCC1,BIK1,SNT1,PAT1,CSM1,SLX5,RAD59,BRE1,RAD57,DPB4,SAC3,HMO1,HTA1, MCM21,SWR1,ESC2,SEM1,SPT3,LRS4,SDC1,GMC1,CIN8,BIM1,CHZ1,RAD51,SLX8,RAD4,IOC3,SOH1,RAD54,SAE2,HOS2,RTF1,RRM3, ARP1,CTF8,EST3,HOP1,HOS4,FKH1,MLP2,MGA2,ASF1,SET2,BUD2,RAD27,TOF2,IRS4,SET3,NUP133,RTT109,BRE2,APC9,TOP3,MMS22,R SC2,CTF3,CST9,CDC73,RAD52,CAC2,GTR1,CSM3,CTF18,SPT21,SGS1,CIK1,ESC1,FKH2,RTT106,TOF1,MCK1,HTZ1,MSH2,RTS1,HST3, BUB3,HIR2,DIA2,LEO1,ELG1,IES4,NPT1,RMI1,LGE1,CTI6,HSP82,REC8,CLB2,CTF4,KAR3

Table S8. Representative gene set enrichment for the GO terms in antimicrobial agents treated hypersensitive strain (Continued)

Drug	GO category	GOID	GO_term	No. AQG	No. QG	No. AGB	No. BGG	P-value	FDR	Expected FP	Gene(s) annotated to the term
HU	Process	90304	Nucleic acid metabolic process	252	770	452	1980	1.59E-13	0	0	ATS1,SAW1,OAF1,SWD1,BUD14,HIR1,FMT1,RRN10,HEK2,,TOD6,SNT1,RPS8A,,NUP170,HHF1,HHT1,RPS11B,MUM2,RDH54,TEC1,HPC2,HSM3,DPB3,DCC1,RIM1,BUD31,HCM1,PAT1,PTC1, SLX5,RPN4,SLM3,LHP1,RAD59,BRE1,RXT3,TRM3,PRR2,RAD57,RPS11A,RAD28,RAD55,MSH6,TMA64,TRM1,DPB4,INO2,SWI5,RPA14,SAC3,CWC15,HMO1,HTA1,SUM1,IRC3,ESC2,SEM1, SPT3,LRS4,SDC1,EDC3,RAD23,RAD51,SWI4,SLX8,SCS2,RTR1,RAD4,TOG1,DEG1,GAT1,PDR1,CKB1,PNC1,DST1,DBP3,LIF1,ARC1,SOH1,MRM2,RAD54,XRN1,BUD13,SAE2,GTS1,HOS2,SKI8, RTF1,SLX9,CLB6,RPS23A,GTR2,ELP2,YAP3,RPS27B,RRM3,PIH1,UBA4,WSS1,RTT107,STB5,CTF8,SKN7,EST3,VID28,NOT3,AIR1,FKH1,MLP2,IMP2',IST3,DAL81,MGA2,RTT101,SAP185,ASF1, LSM1,RPS21B,SET2,RPS14B,POL32,EAF6,IXR1,RAD27,APN1,CTK1,ELF1,ASH1,TOF2,IRS4,DBP7,SAP190,SET3,DAL80,UTH1,NAP1,RPS21A,MSA2,NUP133,SIR1,RTT109,PPR1,BRE2,IRC25, RAD5,RPS0B,SPT8,HOG1,PUS5,RFX1,SWI6,YKE2,TOP3,RPS28B,MMS22,REC102,NUP2,RSC2,PSY3,CTF3,IKI3,CST9,SKI2,CDC73,LEU3,RPS18B,TSA1,YML028W,USA1,YML029W,RAD52, MFT1,RPS1B,NGL3,GTR1,SUB1,ARG80,CSM3,MOT3,RCO1,CTF18,NAM7,YMR087W,RPS16A,MLH1,SPT21,HSC82,SGS1,ESC1,MRE11,ZDS1,YKU70,ELP6,FKH2,NCS2,EAF7,LSM7,PSY2, RTT106,SIN4,TOF1,YNL273W,CLA4,TRF5,MCK1,STB1,DAL82,CSE2,MPP6,HTZ1,RTG1,MSH2,HMI1,SKM1,TRM11,HST3,CIN5,HIR2,CKA2,MSA1,BUD21,DIA2,LEO1,ELG1,IES4,NPT1,PUS7, RFM1,SNU66,YOR338W,VTS1,IRC15,RAD1,RMI1,TRM44,ELC1,SGF11,LGE1,ELP3,RLM1,RPS6A,ELP4,CBC2,CTI6,LEA1,USV1,HSP82,HAL1,REC8,HAA1,ROX1,CLB5,RPS23B,CTF4,MMS1
		6725	Cellular aromatic compound metabolic process	280	770	519	1980	6.05E-13	0	0	ATS1,SAW1,OAF1,SWD1,BUD14,HIR1,FMT1,RRN10,HEK2,URA7,TOD6,YBL055C,RPS8A,YBL072C,NUP170,HHF1,HHT1,RPS11B,MUM2,RDH54,TEC1,PHO3,HPC2,HSM3,DPB3,DCC1,RIM1, SNT1,BUD31,HCM1,PAT1,PTC1,SLX5,RPN4,SLM3,LHP1,RAD59,BRE1,RXT3,TRM3,HNT1,PRR2,RAD57,TRP1,RPS11A,RAD28,RAD55,MSH6,TMA64,TRM1,DPB4,INO2,SWI5,RPA14,SAC3, CWC15,HMO1,HTA1,HNT2,SUM1,IRC3,ESC2,SEM1,SPT3,LRS4,SDC1,SAM2,FDC1,EDC3,RAD23,YEF1,RAD51,SWI4,SLX8,SCS2,RTR1,RAD4,TOG1,DEG1,GAT1,PDR1,CKB1,PNC1,DST1,DBP3, LIF1,ARC1,SOH1,MRM2,RAD54,XRN1,BUD13,SAE2,GTS1,HOS2,SKI8,RTF1,SLX9,CLB6,RPS23A,GTR2,ELP2,YAP3,RPS27B,RRM3,PIH1,UBA4,WSS1,RTT107,STB5,CTF8,SKN7,EST3,VID28, HIS6,NOT3,RNR3,AIR1,COX5B,FKH1,MLP2,IMP2',IST3,DAL81,MGA2,RTT101,SAP185,ASF1,LSM1,RPS21B,SET2,RPS14B,POL32,CYC1,EAF6,IXR1,RAD27,APN1,PGM1,CTK1,ELF1,ASH1, TOF2,IRS4,DBP7,SAP190,SET3,DAL80,UTH1,NAP1,RPS21A,SIS2,MSA2,NUP133,SIR1,RTT109,PPR1,BRE2,IRC25,RAD5,PDC1,RPS0B,SPT8,HOG1,PUS5,RFX1,SWI6,YKE2,YLR200W,PNP1, YLR209C,TOP3,RPS28B,MMS22,REC102,NUP2,RSC2,PSY3,CTF3,IKI3,CST9,SKI2,CDC73,LEU3,APT1,RPS18B,TSA1,USA1,RAD52,MFT1,RPS1B,NGL3,GTR1,SUB1,ARG80,CSM3,MOT3,RCO1, CTF18,NAM7,YMR087W,RPS16A,YMR143W,MLH1,SPT21,HSC82,SGS1,PFK2,ESC1,MRE11,COX7,ZDS1,YKU70,ABZ2,ADH2,ELP6,FKH2,NCS2,EAF7,LSM7,PSY2,RTT106,SIN4,TOF1,CLA4, TRF5,MCK1,STB1,DAL82,CSE2,MPP6,ABZ1,HTZ1,THI20,RTG1,IRA2,MSH2,HMI1,SKM1,TRM11,HST3,CIN5,HIR2,CKA2,MSA1,BUD21,DIA2,LEO1,ELG1,IES4,NPT1,PUS7,RFM1,SNU66, YOR338W,VTS1,IRC15,RAD1,RMI1,TRM44,ELC1,SGF11,LGE1,ELP3,RLM1,RPS6A,ELP4,COX10,CBC2,CTI6,LEA1,THI6,USV1,HSP82,HAL1,REC8,HAA1,ROX1,CLB5,THI22,RPS23B,CTF4, MMS1, QCR2
		6259	DNA metabolic process	104	770	159	1980	2.85E-09	0	0	SAW1,SWD1,HEK2,YBL055C,HHT1,MUM2,RDH54,HSM3,DPB3,DCC1,RIM1,SLX5,RPN4,HEK2,BRE1,RAD57,RAD28,RAD55,MSH6,DPB4,SWI5,SAC3,HTA1,SUM1,IRC3,ESC2,SEM1,RAD51,SL X8,RAD4,PNC1,LIF1,SOH1,RAD54,SAE2,SKI8,RTF1,CLB6,RRM3,WSS1,RTT107,CTF8,EST3,FKH1,RTT101,SET2,POL32,EAF6,IXR1,RAD27,APN1,ASH1,NUP133,RTT109,BRE2,RAD5,HOG1,SW I6,TOP3,MMS22,REC102,RSC2,PSY3,CTF3,CST9,CDC73,TSA1,RAD52,MFT1,SUB1,CSM3,RCO1,CTF18,NAM7,MLH1,HSC82,SGS1,MRE11,YKU70,FKH2,EAF7,PSY2,TOF1,MCK1,STB1,MSH2,H MI1,DIA2,LEO1,ELG1,IES4,RFM1,VTS1,IRC15,RAD1,RMI1,ELC1,LGE1,CTI6,HSP82,REC8,CLB5,CTF4,MMS1
		44260	Cellular macromolecule metabolic process	370	770	765	1980	9.30E-09	0	0	SSA1,ATS1,SAW1,OAF1,PEX22,CNE1,SWD1,BUD14,KIN3,HIR1,FMT1,FUS3,RRN10,BIK1,TOD6,YBL055C,RPS8A,SSA3,NUP170,HHF1,HHT1,RKM3,RPS11B,MUM2,RDH54,UBC4,TEC1,SLI15, HPC2,HSM3,DPB3,DCC1,STE50,RIM1,SNT1,BUD31,HCM1,IMG2,PAT1,PTC1,SLX5,RPN4,SLM3,LHP1,RAD59,BRE1,RXT3,RPP1A,TRM3,PRR2,WHI4,OST4,PHO13,RAD57,RPS11A,RAD28, VMS1,RAD55,MSH6,TMA64,TRM1,DPB4,KIN1,INO2,SWF1,SWI5,RPA14,SAC3,NBP2,CWC15,HMO1,HTA1,MNN10,SWM1,SUM1,IRC3,RQC1,GGA1,ESC2,SEM1,RPP2B,SPT3,ERD1,PPM1,LRS4, SDC1,RPL27B,EDC3,RAD23,AFG1,BIM1,RPL34A,PCL6,RAD51,SWI4,SLX8,SCS2,YCK3,RTR1,RAD4,TOG1,DEG1,GAT1,BUD27,BST1,UBP6,PDR1,CKB1,PNC1,DST1,TIF4632,DBP3,GUP1,LIF1, ARC1,SOH1,MRM2,RAD54,XRN1,BUD13,SAE2,GTS1,HOS2,SKI8,RTF1,EFM5,SLX9,DBF2,PCP1,CLB6,RPS23A,GTR2,UBR1,CRH1,ELP2,YAP3,RPS27B,RRM3,PIH1,KSP1,UBA4,ARP1,WSS1, RTT107,STB5,PTH1,CTF8,RPN10,SKN7,EST3,VID28,NOT3,PKP1,PIG2,AIR1,RSM25,HOS4,FKH1,RPL16A,MLP2,IMP2',IST3,DAL81,MGA2,RTT101,BCK1,SAP185,ASF1,LSM1,PBS2,RPS21B, YAK1,SNA3,HAL5,SET2,RPS14B,HUL4,POL32,HOC1,EAF6,GRR1,RPS4A,RPL14A,IXR1,VPS24,ELM1,TEF4,BUD2,HSL1,RAD27,APN1,SSH4,PGM1,CTK1,ELF1,NNK1,ASH1,PEX1,TOF2,IRS4, DBP7,BCH2,SAP190,SET3,DAL80,UTH1,NAP1,RPS21A,MSA2,SIR1,RTT109,SSK1,PPR1,BRE2,IRC25,UBR2,RAD5,RPS0B,SPT8,APC9,HOG1,PUS5,RFX1,SWI6,YKE2,TOP3,ARV1,RPS28B,GUF1, UBC12,MMS22,REC102,NUP2,RSC2,VID22,PSY3,CTF3,IKI3,CST9,SKI2,RPL31B,CDC73,RPN13,ATG17,LEU3,PPZ1,RPS18B,TSA1,USA1,RAD52,MFT1,RPS1B,BUL2,NGL3,GTR1,CSI1,IMP2, MIH1,SUB1,ARG80,CSM3,MOT3,RCO1,YMR075W,CTF18,NAM7,YMR087W,ASC1,RPS16A,MLH1,SPT21,HSC82,SGS1,ESC1,MRE11,RPS10B,ZDS1,YKU70,TDA1,ELP6,ARK1,YDJ1,FKH2,EOS1, NCS2,EAF7,LSM7,PSY2,RTT106,URE2,SIN4,TOF1,PCL1,CLA4,TRF5,RPS19B,MCK1,STB1,SKP2,DAL82,CSE2,MPP6,PPG1,PET494,BRE5,PFA4,HTZ1,CMK2,RTG1,MSH2,HMI1,SKM1,RRI2, TRM11,RTS1,SFM1,HST3,BUB3,CIN5,HIR2,CKA2,MSA1,BUD21,DIA2,LEO1,ELG1,NFI1,RPS30B,IES4,LIP5,NPT1,PUS7,RFM1,RPS10A,SNU66,RPL20B,YOR338W,VTS1,LSP1,RQC2,IRC15, RAD1,RMI1,TRM44,ELC1,SGF11,LGE1,ELP3,RLM1,RPS6A,ELP4,CBC2,CTI6,LEA1,USV1,HSP82,CLN2,HAL1,REC8,HAA1,ROX1,UBA3,LTP1,CLB2,CLB5,SCD6,RPS23B,CTF4,GPH1,MMS1
	Function	5488	Binding	223	770	458	1980	0.00029	0	0	SSA1,SAW1,OAF1,PEX22,CNE1,HIR1,RRN10,SHE1,HEK2,EDE1,TOD6,SSA3,NUP170,HCM1,HHT1,MUM2,RDH54,UBC4,TEC1,CCZ1,TBS1,AMN1,SSE2,MSI1,BEM1,HPC2,YPT10,REI1,DPB3, BIK1,STE50,RVS161,RIM1,HCM1,PAT1,ABP1,SLX5,RPN4,GPR1,LHP1,RAD59,BRE1,VAM6,ATG20,HNT1,DLD2,WHI4,OST4,RAD57,RAD55,MSH6,TMA64,DPB4,SWI5,NUM1,SAC3,NBP2, HMO1,HTA1,JVY1,PMP3,GIC2,SUM1,YSP2,MSN5,GGA1,GIM4,EDC3,RAD23,BIM1,CHZ1,GET2,RAD51,SWI4,SCS2,BEM2,RAD4,TOG1,GAT1,IOC3,FAB1,PDR1,DST1,TIF4632,LIF1,ARC1, PMR1,XRN1,SAE2,GTS1,RTF1,PAC10,GTR2,ELP2,MVB12,HSV2,SCW4,YAP3,PIH1,KSP1,STB5,RPN10,SKN7,EST3,NOT3,HOP1,FKH1,RPL16A,MLP2,ASF1,LSM1,PBS2,SNA3,ATG27,RPS14B, RCY1,CPR7,MOG1,GRR1,BUD4,RPL14A,IXR1,TEF4,SHE2,ELF1,ASH1,PEX1,SET3,DAL80,NAP1,SIR1,SSK1,PPR1,RAD5,SPT8,HOG1,RFX1,PEX13,YKE2,GUF1,NUP2,ROM2,IKI3,CST9,SKI2, CDC73,RPN13,ATG17,LEU3,TSA1,USA1,MFT1,CAC2,SOK2,SUB1,ARG80,MOT3,NAM7,ASC1,MLH1,HSC82,CIK1,PFK2,MRE11,YKU70,ELP6,SFB2,YDJ1,FKH2,LSM7,RTT106,URE2,SIN4, MCK1,STB1,SKP2,DAL82,ATP11,VPS27,MPP6,BRE5,HTZ1,TLG2,MSH2,TRM11,BUB3,STI1,CIN5,SHE4,HIR2,VPS5,BUD21,DIA2,ARF3,CEX1,LEO1,ELG1,NFI1,RUD3,HES1,RFM1,VTS1,SCP1, LSP1,RQC2,IRC15,RAD1,RMI1,RLM1,CBC2,CTI6,USV1,YAR1,HSP82,REC8,ROX1,CLB2,SCD6,CTF4,KAR3,CUR1,VPS4
	Component	44428	Nuclear part	141	770	248	1980	2.50E-07	0	0	OAF1,SWD1,RRN10,SHE1,HEK2,TOD6,NUP170,HHF1,HHT1,DPB3,BIK1,SNT1,BUD31,MUM2,CSM1,SLX5,LHP1,BRE1,RXT3,RAD57,RAD55,MSH6,TRM1,DPB4,INO2,RPA14,SAC3,CWC15, HMO1,HTA1,SWM1,MCM21,SWR1,SPT3,LRS4,SDC1,KRE28,RAD23,CIN8,RAD51,SWI4,SLX8,SCS2,RAD4,IOC3,KAP122,CKB1,YBP2,DBP3,LIF1,SOH1,BUD13,HOS2,SKI8,RTF1,SLX9,GTR2, YGR283C,RRM3,WSS1,SPO12,EST3,APQ12,HOP1,AIR1,HOS4,MLP2,IST3,HUL4,POL32,EAF6,IXR1,CTK1,ELF1,ASH1,TOF2,DBP7,SET3,NUP133,SRP40,SIR1,BRE2,POM34,RAD5,SPT8,APC9, SWI6,REC102,NUP2,RSC2,CTF3,CST9,CDC73,RAD52,MFT1,CSI1,CSM3,RCO1,CTF18,MLH1,SGS1,ESC1,MRE11,GFD1,YKU70,MKT1,EAF7,LSM7,PSY2,IES2,SIN4,TOF1,TRF5,STB1,CSE2, MPP6,HTZ1,MSH2,RRI2,RTS1,BUB3,CKA2,BUD21,DIA2,CEX1,LEO1,NFI1,IES4,RFM1,SNU66,RAD1,RMI1,ELC1,SGF11,CBC2,CTI6,UIP4,LEA1,REC8,ROX1,CTF4

Table S8. Representative gene set enrichment for the GO terms in antimicrobial agents treated hypersensitive strain (Continued)

Drug	GO category	GOID	GO_term	No. AQG	No. QG	No. AGB	No. BGG	P-value	FDR	Expected FP	Gene(s) annotated to the term
BTZ	Process	90304	nucleic acid metabolic process	183	466	452	1980	1.90E-17	0	0	SAW1,BUD14,HIR1,YBL055C,NUP170,TEL1,HHT1,RPS11B,MUM2,RDH54,TEC1,HSM3,DPB3,DCC1,RIM1,SNT1,BUD31,HCM1,PAT1,RPN4,SLM3,RAD59,BRE1,PHO2,TRM3,RAD57,RAD28,RAD55,TMA64,DPB4,INO2,RPA14,SAC3,HMO1,HTA1,IPK1,ESC2,SEM1,SPT3,LRS4,FIR1,RAD51,SWI4,SLX8,RAD4,CKB1,DST1,SGF73,LIF1,ARC1,SOH1,MRM2,RAD54,XRN1,BUD13,SAE2,RTF1,UPF3,SLX9,CLB6,RPS23A,ELP2,YAP3,RRM3,SRB2,UBA4,WSS1,RTT107,STB5,CTF8,SKN7,EST3,VID28,NOT3,MLP2,IMP2',MPH1,IST3,DAL81,MGA2,RTT101,ASF1,SET2,POL32,RAD27,APN1,ASH1,TOF2,IRS4,SAP190,SET3,MSA2,NUP133,RTT109,PPR1,IRC25,RAD5,SPT8,HOG1,PUS5,RFX1,SWI6,TOP3,RPS28B,MMS22,RSC2,PSY3,CST9,SKI2,CDC73,LEU3,RPS18B,TSA1,USA1,RAD52,MFT1,RPS1B,NGL3,GTR1,SUB1,CSM3,MOT3,RCO1,CTF18,YMR087W,MLH1,SPT21,HSC82,SGS1,ESC1,MRE11,YKU70,ELP6,FKH2,NCS2,EAF7,LSM7,GCR2,PSY2,RTT106,SIN4,TOF1,CLA4,MCK1,STB1,CSE2,MPP6,TOP1,HTZ1,MSH2,HMI1,SKM1,HST3,HIR2,CKB2,CKA2,MSA1,DIA2,LEO1,ELG1,IES4,NPT1,PUS7,RFM1,SNU66,YOR338W,RAD1,RMI1,LGE1,ELP3,RPS6A,ELP4,CTI6,LEA1,USV1,HSP82,HAL1,REC8,HAA1,CLB5,RPS23B,CTF4,MMS1
		6259	DNA metabolic process	89	466	159	1980	3.78E-17	0	0	SAW1,YBL055C,TEL1,HHT1,MUM2,RDH54,HSM3,DPB3,DCC1,RIM1,RPN4,RAD59,BRE1,RAD57,RAD28,RAD55,DPB4,SAC3,HTA1,ESC2,SEM1,RAD51,SLX8,RAD4,LIF1,SOH1,RAD54,SAE2,RTF1,UPF3,CLB6,RRM3,WSS1,RTT107,CTF8,EST3,MPH1,RTT101,SET2,POL32,RAD27,APN1,ASH1,NUP133,RTT109,RAD5,HOG1,SWI6,TOP3,MMS22,RSC2,PSY3,CST9,CDC73,TSA1,RAD52,MFT1,SUB1,CSM3,RCO1,CTF18,MLH1,HSC82,SGS1,MRE11,YKU70,FKH2,EAF7,PSY2,TOF1,MCK1,STB1,TOP1,MSH2,HMI1,DIA2,LEO1,ELG1,IES4,RFM1,RAD1,RMI1,LGE1,CTI6,HSP82,REC8,CLB5,CTF4,MMS1
		6974	cellular response to DNA damage stimulus	66	466	102	1980	1.28E-16	0	0	SAW1,TEL1,HHT1,RDH54,HSM3,DPB3,DCC1,RPN4,RAD59,BRE1,RAD57,RAD28,RAD55,DPB4,SAC3,HTA1,ESC2,SLX8,RAD4,CKB1,LIF1,SOH1,RAD54,SAE2,RTF1,RRM3,WSS1,RTT107,MPH1,RTT101,POL32,GRR1,RAD27,APN1,NUP133,RTT109,RAD5,YLR235C,MMS22,RSC2,PSY3,CDC73,TSA1,RAD52,SUB1,CSM3,CTF18,MLH1,SGS1,MRE11,YKU70,MKT1,EAF7,PSY2,TOF1,MCK1,MSH2,CKB2,CKA2,LEO1,ELG1,IES4,RAD1,RMI1,CTF4,MMS1
		46483	heterocycle metabolic process	198	466	523	1980	3.18E-15	0	0	SAW1,BUD14,HIR1,URA7,YBL055C,NUP170,TEL1,HHT1,RPS11B,MUM2,RDH54,TEC1,PHO3,HSM3,DPB3,DCC1,RIM1,SNT1,BUD31,HCM1,PAT1,RPN4,SLM3,RAD59,BRE1,PHO2,TRM3,HNT1,RAD57,RAD28,RAD55,TMA64,DPB4,INO2,RPA14,SAC3,HMO1,HTA1,HNT2,IPK1,ESC2,SEM1,SPT3,LRS4,SAM2,FIR1,RAD51,SWI4,SLX8,RAD4,CKB1,DST1,SGF73,LIF1,ARC1,SOH1,MRM2,RAD54,XRN1,BUD13,SAE2,RTF1,UPF3,SLX9,CLB6,RPS23A,ELP2,YAP3,RRM3,SRB2,UBA4,WSS1,RTT107,STB5,CTF8,SKN7,EST3,VID28,HIS6,NOT3,COX5B,MLP2,IMP2',MPH1,IST3,DAL81,DAL4,MGA2,RTT101,ASF1,SET2,POL32,RAD27,APN1,ASH1,TOF2,IRS4,SAP190,SET3,MSA2,NUP133,RTT109,PPR1,IRC25,RAD5,SPT8,HOG1,PUS5,RFX1,SWI6,PNP1,TOP3,RPS28B,MMS22,RSC2,PSY3,CST9,SKI2,CDC73,LEU3,RPS18B,TSA1,USA1,RAD52,MFT1,RPS1B,NGL3,GTR1,SUB1,CSM3,MOT3,RCO1,CTF18,YMR087W,MLH1,SPT21,HSC82,SGS1,PFK2,ESC1,MRE11,COX7,YKU70,ABZ2,ADH2,ELP6,FKH2,NCS2,EAF7,LSM7,GCR2,PSY2,RTT106,SIN4,TOF1,CLA4,MCK1,STB1,CSE2,MPP6,TOP1,HTZ1,IRA2,MSH2,HMI1,SKM1,HST3,HIR2,CKB2,CKA2,MSA1,DIA2,LEO1,ELG1,IES4,NPT1,PUS7,RFM1,SNU66,YOR338W,RAD1,RMI1,LGE1,ELP3,RPS6A,ELP4,CTI6,LEA1,USV1,HSP82,HAL1,REC8,HAA1,CLB5,THI22,RPS23B,CTF4,MMS1
	Function	5488	binding	148	466	458	1980	0.00017	0	0	SAW1,PEX22,CNE1,SLA1,HIR1,SHE1,EDE1,NUP170,TEL1,HHT1,MUM2,RDH54,UBC4,TEC1,TBS1,MSI1,BEM1,REI1,DPB3,BIK1,RIM1,HCM1,PAT1,RPN4,RAD59,BRE1,VAM6,PHO2,ATG20,HNT1,RAD57,RAD55,TMA64,DPB4,NUM1,SAC3,NBP2,HMO1,HTA1,IVY1,GGA1,GIM4,BIM1,CHZ1,RAD51,SWI4,RAD4,FAB1,DST1,LIF1,ARC1,PMR1,XRN1,SAE2,RTF1,UPF3,PAC10,ELP2,YAP3,SRB2,KSP1,CRP1,STB5,RPN10,SKN7,EST3,NOT3,HOP1,RPL16A,MLP2,MPH1,ASF1,PHO86,SNA3,ATG27,RCY1,MOG1,GRR1,LHS1,
		5515	protein binding	78	466	218	1980	0.00309	0	0	PEX22,CNE1,SLA1,HIR1,SHE1,EDE1,NUP170,MUM2,UBC4,MSI1,BEM1,BIK1,PAT1,RAD59,VAM6,RAD57,RAD55,DPB4,NUM1,SAC3,NBP2,GGA1,GIM4,BIM1,CHZ1,DST1,RTF1,PAC10,ELP2,SRB2,RPN10,NOT3,ASF1,PHO86,SNA3,RCY1,MOG1,GRR1,LHS1,PEX1,SET3,SSK1,SPT8,CDC73,RPN13,ATG17,UBX2,TSA1,USA1,MFT1,CAC2,UBX4,MOT3,ASC1,HSC82,CIK1,MRE11,YDJ1,FKH2,GCR2,RTT106,SIN4,MCK1,STB1,SKP2,ATP11,BUB3,HIR2,LEO1,RFM1,SCP1,CTI6,YAR1,HSP82,CLB2,KAR3,CUR1,VPS4
		46983	protein dimerization activity	9	466	10	1980	0.00505	0	0	BIK1,RAD57,RAD55,BIM1,PEX1,SSK1,CIK1,KAR3,VPS4
	Component	44428	nuclear part	102	466	248	1980	8.27E-09	0	0	SHE1,NUP170,HHT1,DPB3,BIK1,SNT1,BUD31,HCM1,CSM1,BRE1,RAD57,RAD55,DPB4,INO2,RPA14,SAC3,HMO1,HTA1,MCM21,SWR1,SPT3,LRS4,KRE28,CIN8,RAD51,SWI4,SLX8,RAD4,CKB1,YBP2,SGF73,LIF1,SOH1,BUD13,RTF1,UPF3,SLX9,RRM3,SRB2,WSS1,SPO12,EST3,APQ12,HOP1,MLP2,IST3,HUL4,POL32,ASH1,TOF2,SET3,NUP133,RAD5,SPT8,APC9,SWI6,RSC2,CST9,CDC73,RAD52,MFT1,CSI1,CSM3,RCO1,CTF18,MLH1,SGS1,ESC1,MRE11,GFD1,YKU70,MKT1,EAF7,LSM7,GCR2,PSY2,IES2,SIN4,TOF1,STB1,CSE2,MPP6,TOP1,HTZ1,MSH2,RTS1,BUB3,CKB2,CKA2,DIA2,CEX1,LEO1,IES4,RFM1,SNU66,RAD1,RMI1,CTI6,UIP4,LEA1,REC8,CTF4

REFERENCES

Ablordeppey SY, Fan P, Ablordeppey JH & Mardenborough L (1999) Systemic antifungal agents against AIDS-related opportunistic infections: current status and emerging drugs in development. *Curr Med Chem* **6**: 1151–1195.

Agarwal AK, Xu T, Jacob MR, Feng Q, Li XC, Walker LA & Clark AM (2008) Genomic and genetic approaches for the identification of antifungal drug targets. *Infect Disord Drug Targets* **8**: 2–15.

Ahmad MH, Rechenmacher A & Böck A (1980) Interaction between aminoglycoside uptake and rib osomal resistance mutations. *Antimicrob Agents Chemother* **18**: 798–806.

Akaike N & Hirata N (1994) Nystatin perforated patch recording and its applications to analyses of intracellular mechanisms. *Japanes J Physiol* **44**: 433–473.

Alberts a W, Chen J, Kuron G, *et al.* (1980) Mevinolin: a highly potent competitive inhibitor of hydroxymethylglutaryl-coenzyme A reductase and a cholesterol-lowering agent. *Proc Natl Acad Sci U S A* **77**: 3957–3961.

Andriole VT (1999) Current and future antifungal therapy: new targets for antifungal agents. *J Antimicrob Chemother* **44**: 151–162.

Andrusiak K (2012) Adapting S. cerevisiae chemical genomics for identifying the modes of action of natural compounds. University of Toronto, Master Thesis.

Ballou CE (1990) Isolation, characterization, and properties of *Saccharomyces cerevisiae mnn* mutants with nonconditional protein glycosylation defects. *Methods Enzymol* **185**: 440–470.

Bammert GF & Fostel JM (2000) Genome-wide expression patterns in *Saccharomyces cerevisiae*: Comparison of drug treatments and genetic alterations affecting biosynthesis of ergosterol. *Antimicrob Agents Chemother* **44**: 1255–1265.

Bharucha N & Kumar A (2007) Yeast genomics and drug target identification. *Comb Chem High Throughput Screen* **10**: 618–634.

Bloch KE (1983) Sterol structure and membrane function. *CRC Crit Rev Biochem* **14**: 47–92.

Bodey GP (1992) Azole antifungal agents. *Clin Infect Dis* **14 Suppl 1**: S161–S169.

Borovinskaya M, Shoji S, Fredrick K & Cate JHD (2008) Structural basis for hygromycin B inhibition of protein biosynthesis Structural basis for hygromycin B inhibition of protein biosynthesis. *RNA* **14**: 1590–1599.

Botstein D & Fink GR (2011) Yeast: An experimental organism for 21st century biology. *Genetics* **189**: 695–704.

Botstein D, Chervitz SA, Cherry JM, *et al.* (1997) Yeast as a model organism. *Science* **277**: 1259–1260.

Boyle EI, Weng S, Gollub J, Jin H, Botstein D, Cherry JM & Sherlock G (2004) GO::TermFinder - Open source software for accessing gene ontology information and finding significantly enriched gene ontology terms associated with a list of genes. *Bioinformatics* **20**: 3710–3715.

Butts A & Krysan DJ (2012) Antifungal drug discovery: something old and something new. Goldman WE, ed. *PLoS Pathog* **8**: e1002870.

Carrillo-Muñoz AJ, Giusiano G, Ezkurra PA & Quindós G (2006) Antifungal agents: mode of action in yeast cells. *Rev Esp Quimioter* **19**: 130–139.

Castro M (2012) Linear discriminant analysis versus artificial neural network as classifiers for elbow angular position recognition purposes. *Proceedings of the International Conference on Bio-inspired Systems and Signal Processing*, (Sabine VH, Correia C, Fred A & Gamboa H, eds), pp. 351–355. Scitepress, Vilamoura, Algarve, Portugal.

Chang C & Cheng Y (1978) Ribonucleotide reductase isolated. *Biochem Pharmacol* **27**: 2297–2300.

Chang M, Bellaoui M, Boone C & Brown GW (2002) A genome-wide screen for methyl methanesulfonate-sensitive mutants reveals genes required for S phase progression in the presence of DNA damage. *Proc Natl Acad Sci U S A* **99**: 16934–16939.

Chen J & Stubbe J (2005) Bleomycins: towards better therapeutics. *Nat Rev Cancer* **5**: 102–112.

Chen X, Ren B, Chen M, Liu MX, Ren W, Wang QX, Zhang LX & Yan GY (2014) ASDCD: Antifungal synergistic drug combination database. *PLoS One* **9**: 2008–9401.

Concu R, Podda G, Ubeira FM & González-Díaz H (2010) Review of QSAR models for enzyme classes of drug targets: Theoretical background and applications in parasites, hosts, and other organisms. *Curr Pharm Des* **16**: 2710–2723.

Creighton C & Hanash S (2003) Mining gene expression databases for association rules. *Bioinformatics* **19**: 79–86.

Davies J (2006) Where have all the antibiotics gone? *Can J Infect Dis Med Microbiol* **17**: 287–290.

Dröse S, Bindseil KU, Bowman EJ, Siebers a, Zeeck a & Altendorf K (1993) Inhibitory effect of modified bafilomycins and concanamycins on P- and V-type adenosinetriphosphatases. *Biochemistry* **32**: 3902–3906.

Dudley AM, Janse DM, Tanay A, Shamir R & Church GM (2005) A global view of pleiotropy and phenotypically derived gene function in yeast. *Mol Syst Biol* **1**: 2005.0001.

Eggert US (2013) The why and how of phenotypic small-molecule screens. *Nat Publ Gr* **9**: 206–209.

Elledge SJ & Davis RW (1987) Identification and isolation of the gene encoding the small subunit of ribonucleotide reductase from *Saccharomyces cerevisiae*: DNA damage-inducible gene required for mitotic viability. *Mol Cell Biol* **7**: 2783–2793.

Elledge SJ & Davis RW (1990) Two genes differentially regulated in the cell cycle and by DNA-damaging agents encode alternative regulatory subunits of ribonucleotide reductase. *Genes Dev* **4**: 740–751.

Engering A, Hogerwerf L & Slingenbergh J (2013) Pathogen–host–environment interplay and disease emergence. *Emerg Microbes Infect* **2**: e5.

Fang F, Hoskins J & Butler JS (2004) 5-fluorouracil enhances exosome-dependent accumulation of polyadenylated rRNAs. *Mol Cell Biol* **24**: 10766–10776.

Feng Y, Mitchison TJ, Bender A, Young DW & Tallarico J (2009) Multi-parameter phenotypic profiling: using cellular effects to characterize small-molecule

compounds. *Nat Rev Drug Discov* **8**: 567–578.

Finland M & Schönebeck J (1972) Antifungal activity of flucytosine. *J Am Med Assoc* **130**: 789–790.

Fishman MC & Porter JA (2005) Pharmaceuticals: a new grammar for drug discovery. *Nature* **437**: 491–493.

Friedman JH (1989) Regularized discriminant analysis. *J Am Stat Assoc* **84**: 165–175.

Fry RC, Begley TJ & Samson LD (2005) Genome-wide responses to DNA-damaging agents. *Annu Rev Microbiol* **59**: 357–377.

Futamura Y, Kawatani M, Kazami S, Tanaka K, Muroi M, Shimizu T, Tomita K, Watanabe N & Osada H (2012) Morphobase, an encyclopedic cell morphology database, and its use for drug target identification. *Chem Biol* **19**: 1620–1630.

Futamura Y, Kawatani M, Muroi M, Aono H, Nogawa T & Osada H (2013a) Identification of a molecular target of a novel fungal metabolite, pyrrolizilactone, by phenotypic profiling systems. *Chembiochem* **14**: 2456–2463.

Futamura Y, Muroi M & Osada H (2013b) Target identification of small molecules based on chemical biology approaches. *Mol Biosyst* **9**: 897–914.

Gasch AP, Huang M, Metzner S, Botstein D, Elledge SJ & Brown PO (2001) Genomic expression responses to DNA-damaging agents and the regulatory role of the yeast ATR homolog Mec1p. *Mol Biol Cell* **12**: 2987–3003.

Gaughran JP, Lai MH, Kirsch DR & Silverman SJ (1994) Nikkomycin Z is a specific inhibitor of *Saccharomyces cerevisiae* chitin synthase isozyme Chs3 *in vitro* and *in vivo*. *J Bacteriol* **176**: 5857–5860.

Gebre AA, Okada H, Kim C, Kubo K, Ohnuki S & Ohya Y (2015) Profiling of the effects of antifungal agents on yeast cells based on morphometric analysis. *FEMS Yeast Res* **15**: fov040.

Ghannoum M & Rice L (1999) Antifungal agents : mode of action, mechanisms of resistance, and correlation of these mechanisms with bacterial resistance. *Clin Microbiol* **12**: 501–517.

Giaever G, Shoemaker DD, Jones TW, Liang H, Winzeler EA, Astromoff A & Davis RW

(1999) Genomic profiling of drug sensitivities via induced haploinsufficiency. *Nat Genet* **21**: 278–283.

Giaever G, Chu AM, Ni L, *et al.* (2002) Functional profiling of the *Saccharomyces cerevisiae* genome. *Nature* **418**: 387–391.

Gozalbes R, Brun-Pascaud M, Garcia-Domenech R, Galvez J, Girard PM, Doucet JP & Derouin F (2000) Prediction of quinolone activity against *Mycobacterium avium* by molecular topology and virtual computational screening. *Antimicrob Agents Chemother* **44**: 2764–2770.

Gupta K, Bishop J, Peck A, Brown J, Wilson L & Panda D (2004) Antimitotic antifungal compound benomyl inhibits brain microtubule polymerization and dynamics and cancer cell proliferation at mitosis, by binding to a novel site in tubulin. *Biochemistry* **43**: 6645–6655.

Hammond SM (1977) Biological activity of polyene antibiotics. *Prog Med Chem* **14**: 105–179.

Harvey AL (2008) Natural products in drug discovery. *Drug Discov Today* **13**: 894–901.

Hillenmeyer ME, Fung E, Wildenhain J, *et al.* (2008) The chemical genomic portrait of yeast: uncovering a phenotype for all genes. *Science* **320**: 362–365.

Hillenmeyer ME, Ericson E, Davis RW, Nislow C, Koller D & Giaever G (2010) Systematic analysis of genome-wide fitness data in yeast reveals novel gene function and drug action. *Genome Biol* **11**: R30.

Holmes AR, Lin Y-H, Niimi K, Lamping E, Keniya M, Niimi M, Tanabe K, Monk BC & Cannon RD (2008) ABC transporter Cdr1p contributes more than Cdr2p does to fluconazole efflux in fluconazole-resistant Candida albicans clinical isolates. *Antimicrob Agents Chemother* **52**: 3851–3862.

Houle D, Govindaraju DR & Omholt S (2010) Phenomics: the next challenge. *Nat Rev Genet* **11**: 855–866.

Hughes TR, Marton MJ, Jones AR, *et al.* (2000) Functional discovery via a compendium of expression profiles. *Cell* **102**: 109–126.

Isham N & Ghannoum M (2010) Antifungal activity of miconazole against recent Candida strains. *Mycoses* **53**: 434–437.

Iwaki A, Ohnuki S, Suga Y, Izawa S & Ohya Y (2013) Vanillin inhibits translation and induces messenger ribonucleoprotein (mRNP) granule formation in *Saccharomyces cerevisiae*: application and validation of high-content, image-based profiling. *PLoS One* **8**: e61748.

Jacquemont C & Taniguchi T (2007) Proteasome function is required for DNA damage response and fanconi anemia pathway activation. *Cancer Res* **67**: 7395–7405.

James B (2012) Statistical measures for contrast patterns. *In: Contrast Data Mining: Concepts, Algorithms, and Applications*, (Dong G & James B, eds), pp. 13–20. Chapman and Hall/CRC, Boca Raton, FL.

Jansen G, Lee AY, Epp E, Fredette A, Surprenant J, *et al.* (2009) Chemogenomic profiling predicts antifungal synergies. *Mol Syst Biol* **5**: 051909–051909.

Jansen G, Lee AY, Epp E, Fredette A, Surprenant J, *et al.* (2009) Chemogenomic profiling predicts antifungal synergies. *Mol Syst Biol* **5**: 338.

Jia N, Arthington-Skaggs B, Lee W, Pierson C, Lees ND, Eckstein J, Barbuch R & Bard M (2002) Candida albicans sterol C-14 reductase, encoded by the ERG24 gene, as a potential antifungal target site. *Antimicrob Agents Chemother* **46**: 947–957.

Jigami Y (2008) Yeast glycobiology and Its application. *Biosci Biotechnol Biochem* **72**: 637–648.

Jin Y & Weisman LS (2015) The vacuole/lysosome is required for cell-cycle progression. *eLife* **4**.

Johnson ME & Edlind TD (2012) Topological and mutational analysis of *Saccharomyces cerevisiae* Fks1. *Eukaryot Cell* **11**: 952–960.

Johnson ME, Katiyar SK & Edlind TD (2011) New Fks hot spot for acquired echinocandin resistance in *Saccharomyces cerevisiae* and its contribution to intrinsic resistance of Scedosporium species. *Antimicrob Agents Chemother* **55**: 3774–3781.

Jonckheere AR (1954) A distribution-free k-sample test against ordered alternatives. *Biometrika* **41**: 133–145.

Kachroo AH, Laurent JM, Yellman CM, *et al.* (2015) Systematic humanization of yeast genes reveals conserved functions and genetic modularity. *Science* **348**: 921–925.

Katsila T, Spyroulias GA, Patrinos GP & Matsoukas M-T (2016) Computational approaches in target identification and drug discovery. *Comput Struct Biotechnol J* **14**: 177–184.

Kelly SL, Lamb DC, Corran a J, Baldwin BC & Kelly DE (1995) Mode of action and resistance to azole antifungals associated with the formation of 14 alpha-methylergosta-8,24(28)-dien-3 beta,6 alpha-diol. *Biochem Biophys Res Commun* **207**: 910–915.

Kohanski MA, DePristo MA & Collins JJ (2010) Sublethal antibiotic treatment leads to multidrug resistance via radical-induced mutagenesis. *Mol Cell* **37**: 311–320.

Kuo SC & Lampen JO (1974) Tunicamycin - an inhibitor of yeast glycoprotein synthesis. *Biochem Biophys Res Commun* **58**: 287–295.

Kuranda K, Leberre V, Sokol S, Palamarczyk G & François J (2006) Investigating the caffeine effects in the yeast *Saccharomyces cerevisiae* brings new insights into the connection between TOR, PKC and Ras/cAMP signalling pathways. *Mol Microbiol* **61**: 1147–1166.

Lampen JO, Arnow PM, Borowska Z & Laskin AI (1962) Location and role of sterol at nystatin-binding sites. *J Bacteriol* **84**: 1152–1160.

Lang P, Yeow K, Nichols A & Scheer A (2006) Cellular imaging in drug discovery. *Nat Rev Drug Discov* **5**: 343–356.

Lee M, Han S, Chang H, Kwak Y, Weller DM & Kim D (2013) FitSearch : a robust way to interpret a yeast fitness profile in terms of drug's mode-of-action. *BMC Genomics* **14**: 1–11.

Lee W, St.Onge RP, Proctor M, Flaherty P, Jordan MI, Arkin AP, Davis RW, Nislow C & Giaever G (2005) Genome-wide requirements for resistance to functionally distinct DNA-damaging agents. *PLoS Genet* **1**: 0235–0246.

Levin DE (2005) Cell wall integrity signaling in *Saccharomyces cerevisiae. Microbiol Mol Biol Rev* **69**: 262–291.

Liberali P, Snijder B & Pelkmans L (2015) Large-scale genetic perturbation screens have been instrumental in many biological discoveries. *Nat Rev Genet* **16**: 18–32.

Livermore DM (2011) Discovery research: the scientific challenge of finding new

antibiotics. *J Antimicrob Chemother* **66**: 1941–1944.

Luesch H, Wu TYH, Ren P, Gray NS, Schultz PG & Supek F (2005) A genome-wide overexpression screen in yeast for small-molecule target identification. *Chem Biol* **12**: 55–63.

Lum PY, Armour CD, Stepaniants SB, *et al.* (2004) Discovering modes of action for Therapeutic compounds using a genome-wide screen of yeast heterozygotes. *Cell* **116**: 121–137.

Lussier M, White a M, Sheraton J, *et al.* (1997) Large scale identification of genes involved in cell surface biosynthesis and architecture in *Saccharomyces cerevisiae*. *Genetics* **147**: 435–450.

Mahmoudi N, de Julián-Ortiz J-V, Ciceron L, Gálvez J, Mazier D, Danis M, Derouin F & García-Domenech R (2006) Identification of new antimalarial drugs by linear discriminant analysis and topological virtual screening. *J Antimicrob Chemother* **57**: 489–497.

Mahmoudi N, Garcia-Domenech R, Galvez J, Farhati K, Franetich JF, Sauerwein R, Hannoun L, Derouin F, Danis M & Mazier D (2008) New active drugs against liver stages of Plasmodium predicted by molecular topology. *Antimicrob Agents Chemother* **52**: 1215–1220.

Martinez AM & Kak AC (2001) PCA versus LDA. *IEEE Trans Pattern Anal Mach Intell* **23**: 228–233.

Mccusker JH (2006) Saccharomyces cerevisiae: an emerging and model pathogenic fungus. *Molecular Principles of Fungal Pathogenesis*, pp. 245–259. American Society of Microbiology.

Mo C, Valachovic M & Bard M (2004) The ERG28-encoded protein, Erg28p, interacts with both the sterol C-4 demethylation enzyme complex as well as the late biosynthetic protein, the C-24 sterol methyltransferase (Erg6p). *Biochim Biophys Acta* **1686**: 30–36.

Moore C & Hurlbert R. (1985) The inhibition of ribonucleoside diphosphate reductase by hydroxyurea, guanazole and pyrazoloimidazole (IMPY). *Pharmacol Ther* **27**: 167–196.

Morens DM, Folkers GK & Fauci AS (2004) The challenge of emerging and re-emerging infectious diseases. *Nature* **430**: 242–249.

Mukherjee PK, Sheehan D, Puzniak L, Schlamm H & Ghannoum MA (2011) Echinocandins: are they all the same? *J Chemother* **23**: 319–325.

Najm FJ, Madhavan M, Zaremba A, *et al.* (2015) Drug-based modulation of endogenous stem cells promotes functional remyelination *in vivo. Nature* **522**: 216–220.

Nelder J & Wedderburn R (1972) Generalized linear models. *R Stat Soc Ser A* **135**: 370–384.

Newman DJ, Cragg GM & Snader KM (2003) Natural products as sources of new drugs over the period 1981 - 2002. *Nat Prod* **66**: 1022–1037.

Nishi I, Sunada A, Toyokawa M, Asari S & Iwatani Y (2009) In vitro antifungal combination effects of micafungin with fluconazole, voriconazole, amphotericin B, and flucytosine against clinical isolates of Candida species. *J Infect Chemother* **15**: 1–5.

O'Brien HE, Parrent JL, Jackson JA, Moncalvo J & Vilgalys R (2005) Fungal community analysis by large-scale sequencing of environmental samples. *Appl Environ Microbiol* **71**: 5544–5550.

Ohnuki S, Oka S, Nogami S & Ohya Y (2010) High-content, image-based screening for drug targets in yeast. Lehner B, ed. *PLoS One* **5**: e10177.

Ohnuki S, Kobayashi T, Ogawa H, Kozone I, Ueda J-Y, Takagi M, Shin-Ya K, Hirata D, Nogami S & Ohya Y (2012) Analysis of the biological activity of a novel 24-membered macrolide JBIR-19 in *Saccharomyces cerevisiae* by the morphological imaging program CalMorph. *FEMS Yeast Res* **12**: 293–304.

Ohnuki S, Okada H & Ohya Y (2015) Image-based prediction of drug target in yeast. *Methods Mol Biol* **1263**: 319–7.

Ohtani M, Saka A, Sano F, Ohya Y & Morishita S (2004) Development of image processing program for yeast cell morphology. *J Bioinform Comput Biol* **1**: 695–709.

Ohya Y, Sese J, Yukawa M, *et al.* (2005) High-dimensional and large-scale phenotyping of yeast mutants. *Proc Natl Acad Sci U S A* **102**: 19015–19020.

Ohya Y, Kimori Y, Okada H & Ohnuki S (2015) Single-cell phenomics in budding yeast. *Mol Biol Cell* **26**: 3920–3925.

Okada H, Abe M, Asakawa-Minemura M, Hirata A, Qadota H, Morishita K, Ohnuki S, Nogami S & Ohya Y (2010) Multiple functional domains of the yeast l,3-β-glucan synthase subunit Fks1p revealed by quantitative phenotypic analysis of temperature-sensitive mutants. *Genetics* **184**: 1013–1024.

Okada H, Ohnuki S, Roncero C, Konopka JB & Ohya Y (2014) Distinct roles of cell wall biogenesis in yeast morphogenesis as revealed by multivariate analysis of high-dimensional morphometric data. *Mol Biol Cell* **25**: 222–233.

Ovalle R, Lim ST, Holder B, Jue CK, Moore CW & Lipke PN (1998) A spheroplast rate assay for determination of cell wall integrity in yeast. *Yeast* **14**: 1159–1166.

Parker WiB & Cheng YC (1990) Metabolism and mechanism of action of 5-fluorouracil. *Pharmac Ther* **48**: 381–395.

Parsons AB, Brost RL, Ding H, Li Z, Zhang C, Sheikh B, Brown GW, Kane PM, Hughes TR & Boone C (2004) Integration of chemical-genetic and genetic interaction data links bioactive compounds to cellular target pathways. *Nat Biotechnol* **22**: 62–69.

Parsons AB, Lopez A, Givoni IE, *et al.* (2006) Exploring the mode-of-action of bioactive compounds by chemical-genetic profiling in yeast. *Cell* **126**: 611–625.

Pegg AE (1984) Methylation of the O^6 position of guanine in DNA is the most likely initiating event in carcinogenesis by methylating agents. *Cancer Invest* **2**: 223–231.

Perlin DS (2007) Resistance to echinocandin-class antifungal drugs. *Drug Resist Updat* **10**: 121–130.

Perlman ZE, Slack MD, Feng Y, Mitchison TJ, Wu LF & Altschuler SJ (2004) Multidimensional drug profiling by automated microscopy. *Science* **306**: 1194–1198.

Petranyi G, Ryder NS & Stütz A (1984) Allylamine derivatives: new class of synthetic antifungal agents inhibiting fungal squalene epoxidase. *Science* **224**: 1239–1241.

Piotrowski JS, Okada H, Lu F, *et al.* (2015) Plant-derived antifungal agent poacic acid targets β-1,3-glucan. *Proc Natl Acad Sci* **112**: E1490–E1497.

Polak-Wyss A (1995) Mechanism of action of antifungals and combination therapy. *J Eur*

Acad Dermatology Venereol **4**: S11–S16.

Polak-Wyss A, Lengsfeld H & Oesterhelt G (1985) Effect of oxiconazole and Ro 14-4767/002 on sterol pattern in *Candida albicans*. *Med Mycol* **23**: 433–441.

Price JH, Goodacre A, Hahn K, Hodgson L, Hunter EA, Krajewski S, Murphy RF, Rabinovich A, Reed JC & Heynen S (2002) Advances in molecular labeling, high throughput imaging and machine intelligence portend powerful functional cellular biochemistry tools. *J Cell Biochem* **39**: 194–210.

Rahier A, Pierre S, Riveill G & Karst F (2008) Identification of essential amino acid residues in a sterol 8,7-isomerase from *Zea mays* reveals functional homology and diversity with the isomerases of animal and fungal origin. *Biochem J* **414**: 247–259.

Rao S, Porter DC, Chen X, Herliczek T, Lowe M & Keyomarsi K (1999) Lovastatin-mediated G1 arrest is through inhibition of the proteasome, independent of hydroxymethyl glutaryl-CoA reductase. *Proc Natl Acad Sci U S A* **96**: 7797–7802.

Richards KL, Anders KR, Nogales E, Schwartz K, Downing KH & Botstein D (2000) Structure-function relationships in yeast tubulins. *Mol Biol Cell* **11**: 1887–1903.

Richardson PG & Anderson KC (2003) Bortezomib: a novel therapy approved for multiple myeloma. *Clin Adv Hematol Oncol* **1**: 596–600.

Rine J, Hansen W, Hardeman E & Davis RW (1983) Targeted selection of recombinant clones through gene dosage effects. *Proc Natl Acad Sci U S A* **80**: 6750–6754.

Rix U & Superti-Furga G (2009) Target profiling of small molecules by chemical proteomics. *Nat Chem Biol* **5**: 616–624.

Roemer T & Krysan DJ (2014) Antifungal drug development: challenges, unmet clinical needs, and new approaches. *Cold Spring Harb Perspect Med* **4**: a019703–a019703.

Roemer T, Xu D, Singh SB, Parish CA, Harris G, Wang H, Davies JE & Bills GF (2011) Confronting the challenges of natural product-based antifungal discovery. *Chem Biol* **18**: 148–164.

Rogers PD & Barker KS (2003) Genome-wide expression profile analysis reveals coordinately regulated genes associated with stepwise acquisition of azole resistance in *Candida albicans* clinical isolates. *Antimicrob Agents Chemother* **47**: 1220–1227.

Ross-Macdonald P (2003) Growing yeast for fun and profit: use of saccharomyces cerevisiae as a model system in drug discovery. *Model Organisms in drug discovery*, (Caroll MP & Fitzgerald K, eds), pp. 9–32. John Wiley & Sons Ltd.

Roti G & Stegmaier K (2012) Genetic and proteomic approaches to identify cancer drug targets. *Br J Cancer* **106**: 254–261.

Saito TL, Ohtani M, Sawai H, Sano F, Saka A, Watanabe D, Yukawa M, Ohya Y & Morishita S (2004) SCMD: *Saccharomyces cerevisiae* morphological database. *Nucleic Acids Res* **32**: D319–D322.

Sawistowska-Schriider ET, Kerridge D & Perry H (1984) Echinocandin inhibition of 1,3-β-D-glucan synthase from Candida albicans. *FEBS Lett* **173**: 134–138.

Schenone M, Dančík V, Wagner BK & Clemons P (2013) Target identification and mechanism of action in chemical biology and drug discovery. *Nat Chem Biol* **9**: 232–240.

Schreiber SL (2005) Small molecules: the missing link in the central dogma. *Nat Chem Biol* **1**: 64–66.

Shah Alam Bhuiyan M, Eckstein J, Barbuch R & Bard M (2007) Synthetic lethal interactions involving loss of the yeast ERG24- the sterol C-14 reductase gene. *Lipids* **42**: 69–76.

Shen B (2015) A new golden age of natural products drug discovery. *Cell* **163**: 1297–1300.

Shoji S, Walker SE & Fredrick K (2009) Ribosomal translocation: One step closer to the molecular mechanism. *ACS Chem Biol* **4**: 93–107.

Silver LL (2011) Challenges of antibacterial discovery. *Clin Microbiol Rev* **24**: 71–109.

Spellberg B, Powers JH, Brass EP, Miller LG & Edwards JE (2004) Trends in antimicrobial drug development: Implications for the future. *Clin Infect Dis* **38**: 1279–1286.

St Onge R, Schlecht U, Scharfe C & Evangelista M (2012) Forward chemical genetics in yeast for discovery of chemical probes targeting metabolism. *Molecules* **17**: 13098–13115.

Stearns T, Hoyt MA & Botstein D (1990) Yeast mutants sensitive to antimicrotubule drugs define three genes that affect microtubule function. *Genetics* **124**: 251–262.

Storey JD (2002) A direct approach to false discovery rates. *J R Stat B* **64**: 479–498.

Swets DL (1996) Using discriminant eigenfeatures for image retrieval. *IEEE Trans Pattern Anal Mach Intell* **18**: 831–836.

Swinney DC & Anthony J (2011) How were new medicines discovered? *Nat Rev Drug Discov* **10**: 507–519.

Takeshita T, Wu W, Koike A, Fukuda M & Ohta T (2009) Perturbation of DNA repair pathways by proteasome inhibitors corresponds to enhanced chemosensitivity of cells to DNA damage-inducing agents. *Cancer Chemother Pharmacol* **64**: 1039–1046.

Terfloth L & Gasteiger J (2001) Neural networks and genetic algorithms in drug design. *Drug Discov Today* **6**: 102–108.

Timson J (1975) Hydroxyurea. *Mutat Res* **32**: 115–132.

Toledo‐Arana A & Solano C (2010) Deciphering the physiological blueprint of a bacterial cell. *BioEssays* **32**: 461–467.

Vai M, Popolo L & Alberghina L (1987) Effect of tunicamycin on cell cycle progression in budding yeast. *Exp Cell Res* **171**: 448–459.

Vermes A (2000) Flucytosine: a review of its pharmacology, clinical indications, pharmacokinetics, toxicity and drug interactions. *J Antimicrob Chemother* **46**: 171–179.

Vink E, Vossen JH, Ram AFJ, van den Ende H, Brekelmans S, de Nobel H & Klis FM (2002) The protein kinase Kic1 affects 1,6-β-glucan levels in the cell wall of Saccharomyces cerevisiae. *Microbiology* **148**: 4035–4048.

Vizeacoumar FJ, Chong Y, Boone C & Andrews BJ (2009) A picture is worth a thousand words: Genomics to phenomics in the yeast Saccharomyces cerevisiae. *FEBS Lett* **583**: 1656–1661.

Wagner BK & Schreiber SL (2016) Perspective the power of sophisticated phenotypic screening and modern mechanism-of-action methods. *Cell Chem Biol* **23**: 3–9.

Waldorf AR & Polak A (1983) Mechanisms of action of 5-fluorocytosine. *Antimicrob*

Agents Chemother **23**: 79–85.

Wang PJ, Chabes A, Casagrande R, Tian XC, Thelander L & Huffaker TC (1997) Rnr4p, a novel ribonucleotide reductase small-subunit protein. *Mol Cell Biol* **17**: 6114–6121.

Warringer J, Ericson E, Fernandez L, Nerman O & Blomberg A (2003) High-resolution yeast phenomics resolves different physiological features in the saline response. *Proc Natl Acad Sci U S A* **100**: 15724–15729.

Yang M, Ohnuki S & Ohya Y (2014) Unveiling nonessential gene deletions that confer significant morphological phenotypes beyond natural yeast strains. *BMC Genomics* **15**: 1–12.

Zhang YQ, Gamarra S, Garcia-Effron G, Park S, Perlin DS & Rao R (2010) Requirement for ergosterol in V-ATPase function underlies antifungal activity of azole drugs. *PLoS Pathog* **6**: e1000939.

Zhou X & Wong STC (2006) Informatics challenges of high-throughput microscopy. *IEEE Signal Process Mag* **23**: 63–72.

Zygmunt WA & Tavormina PA (1966) Steroid interference with antifungal activity of polyene antibiotics. *Appl Envir Microbiol* **14**: 865–869.